

Stellar Processes Near the Massive Black Hole in the Galactic Center

Tal Alexander*

Faculty of Physics

The Weizmann Institute of Science

PO Box 26, Rehovot 76100, Israel

Abstract

A massive black hole resides in the center of most, perhaps all galaxies. The one in the center of our home galaxy, the Milky Way, provides a uniquely accessible laboratory for studying in detail the connections and interactions between a massive black hole and the stellar system in which it grows; for investigating the effects of extreme density, velocity and tidal fields on stars; and for using stars to probe the central dark mass and to probe post-Newtonian gravity in the weak- and strong-field limits. Recent results, open questions and future prospects are reviewed in the wider context of the theoretical framework and physical processes that underlie them.

keywords: black hole, Milky Way, galactic nucleus, stellar dynamics, stellar physics

PACS: 97.10.-q, 98.10.+z, 98.35.J, 98.62.Js

Contents

1	Introduction	3
1.1	Astrophysical context	3
1.2	Science questions	5
1.3	Scope and connections to related topics	6
2	Observational overview: Stars in the Galactic center	7
2.1	The central 100 parsecs	7
2.2	The central parsec	10

*Incumbent of the William Z. & Eda Bess Novick career development chair

Email address: <mailto:tal.alexander@weizmann.ac.il> (Tal Alexander)

URL: <http://www.weizmann.ac.il/~tal/> (Tal Alexander)

3	Stellar dynamics at extreme densities	13
3.1	Physical processes and scales	13
3.1.1	Dynamical processes	13
3.1.2	Characteristic scales	14
3.1.3	Keplerian power-law stellar cusps	17
3.2	The stellar cusp in the Galactic center	19
3.3	Mass segregation	22
3.4	Stellar Collisions	24
3.4.1	Collisional destruction of giants	25
3.4.2	Tidal spin-up	27
3.4.3	Stellar mergers and exotic objects	28
4	Probing the dark mass with stellar dynamics	30
4.1	Weighing and pinpointing the dark mass	31
4.1.1	Statistical estimators	33
4.1.2	Orbital estimators	35
4.1.3	Distance to the Galactic Center	39
4.2	Constraints on non-BH dark mass alternatives	40
4.2.1	Cluster of dark stellar-mass objects	40
4.2.2	Exotic elementary particles	42
4.2.3	Extended dark mass around the MBH	43
4.3	Limits on MBH binarity	44
4.4	High-velocity runaway stars	45
5	Probing post-Newtonian gravity near the MBH	46
5.1	Relativistic orbital effects	46
5.1.1	Gravitational redshift	47
5.1.2	Periapse shift	48
5.1.3	Frame dragging	49
5.2	Gravitational lensing	50
5.2.1	Point mass gravitational lens	50
5.2.2	Gravitational lensing by the Galactic MBH	52
5.2.3	Beyond the point lens approximation	55
6	Strong star–MBH interactions	56
6.1	Tidal disruption	57
6.1.1	Tidal disruption rate	58
6.1.2	Tidal disruption and its aftermath	61
6.1.3	Signatures of tidal disruption	64
6.1.4	Tidal detonation	65
6.2	Dissipative interactions with the MBH	67
6.2.1	Orbital inspiral into the MBH	67
6.2.2	Gravitational wave emission	69
6.2.3	Tidal heating, squeezars, and tidal capture	71
6.2.4	Tidal scattering	72
6.2.5	Star–disk interactions	75
7	The riddle of the young stars	75
7.1	The difficulties of forming or importing stars near a MBH	77

7.2	Proposed solutions	78
7.2.1	Unusual <i>in-situ</i> star formation	78
7.2.2	Rejuvenation	80
7.2.3	Dynamical migration	80
7.2.4	Exchange capture	81
7.3	Feeding the MBH with stellar winds	82
8	Outlook	83
8.1	Progress report	83
8.2	Future directions	83
	Acknowledgements	86
	References	86

1 Introduction

The massive black hole (MBH) in the center of the Milky Way is the nearest example of a universal phenomenon: central galactic MBHs. It was first detected as an unusual non-thermal radio source, Sagittarius A* (Sgr A*) (Balick & Brown 1974). Over the following decades, observations across the electromagnetic spectrum, together with theoretical arguments, established with ever-growing confidence that Sgr A* is at the dynamical center of the Galaxy and that it is associated with a very massive and compact dark mass concentration. This has ultimately led to the nearly inescapable conclusion that the dark mass is a black hole. At present, observations of Sgr A* and its immediate environment offer the strongest empirical evidence for the existence of MBHs.

This review deals with one of the many aspects of the MBH phenomenon: stellar processes near the MBH in the Galactic center (GC). To motivate this choice of subject matter and to establish the astrophysical context and the scientific questions of interest, it is necessary first to address the questions: why study MBHs? why focus on stars near a MBH? and why in the GC?

1.1 Astrophysical context

Observations indicate that most nearby galaxies contain a massive compact dark object in their center, whose mass lies in the range $10^6 M_\odot \lesssim m \lesssim \text{few} \times 10^9 M_\odot$ (Kormendy & Richstone 1995; Magorrian et al. 1998; Gebhardt et al. 2003; see recent review by Ferrarese & Ford 2005). It is widely believed that these dark objects are MBHs, and that they exist in the centers of most, if not all galaxies. Their number density and mass scale are broadly consistent with the hypothesis that they are now-dead quasars, which were visible for a relatively short time in their past as extremely luminous Active Galactic Nuclei (AGN), powered by the gravitational energy released by the accretion of gas and stars¹ (Soltan 1982; Yu & Tremaine 2002). Some present-day galaxies have AGN, although none as bright as quasars. However, most present-day galactic nuclei are inactive, which implies that accretion has either almost ceased or switched to a non-luminous mode. Their inactivity is not due to the lack of gas supply; most galaxies have more than enough to continue powering an AGN. The “dimness problem” is one of the key issues of accretion theory, which deals with the physics of flows into compact objects (e.g. Narayan 2002).

The MBH mass m is known to correlate very well with σ_{sph} , the stellar velocity dispersion of the spheroidal component of the host galaxy (the spheroid is the bulge in disk galaxies, or the entire galaxy

¹It is possible that very low-mass MBHs like the one in the GC have acquired most of their mass by mergers with other black holes.

in ellipticals. Ferrarese & Merritt 2000; Gebhardt et al. 2000; Tremaine et al. 2002),

$$m \simeq 1.3 \times 10^8 \left(\frac{\sigma_{\text{sph}}}{200 \text{ km s}^{-1}} \right)^{\beta_{m/s}} M_{\odot}, \quad \beta_{m/\sigma} \sim 4-5. \quad (1.1)$$

Since the m/σ_{sph} correlation holds on large scales where the MBH is dynamically unimportant, it suggests a causal connection between the formation of the MBH and its host galaxy. There are also claims of correlations between σ_{sph} and the circular velocity of spiral galaxies on very large scales, which implies a connection between the MBH mass and the dark matter halo of the galaxy (Ferrarese 2002; Baes et al. 2003). Whether it is the galaxy that somehow influences the growth of the MBH, or the MBH that somehow regulates the formation of the galaxy, is still unclear. The nature of the role that MBHs play in the formation and evolution of galaxies is one of the major unsolved problems of galaxy formation.

The Galactic MBH is quite normal. Like most MBHs, it is inactive, and it follows the m/σ_{sph} relation (Valluri et al. 2005). With $m \sim (3-4) \times 10^6 M_{\odot}$, it is one of the least massive MBHs discovered, in keeping with the relatively small bulge of the Milky Way. What makes it special is its proximity. At ~ 8 kpc from the Sun, the Galactic black hole is ~ 100 times closer than the MBH in Andromeda, the nearest large galaxy, and ~ 2000 times closer than galaxies in Virgo, the nearest cluster of galaxies. For this reason it is possible to observe today the stars and gas in the immediate vicinity of the Galactic MBH at a level of detail that will not be possible for any other galaxy in the foreseeable future.

In spite of its relative proximity, observations of the GC are challenging due to strong, spatially variable extinction by interstellar dust, which is opaque to optical-UV wavelengths. Emission processes related to the very low-level accretion activity in the GC can be observed in the radio and mm wavelengths on the long wavelength range of the spectrum, or in X-rays on the short wavelength range. However stars, whose spectra are approximately black-body and extend over a limited wavelength range, emit most of their luminosity in the optical-UV range, some in the IR and negligibly in longer or shorter wavelengths. Observations of stars in the GC must be conducted in the infrared, through the atmospheric transmission “windows” (when observing from Earth), primarily in the K -band² ($2.2 \mu\text{m}$). While the visual extinction along the line of sight to the GC is $A_V \sim 30$ mag, which corresponds to a transmission ratio of only $1 : 10^{12}$ photons, the K -band extinction is only $A_K \sim 3$ mag (Rieke et al. 1989), or a transmission ratio of $1 : 15$ photons. However, IR astronomy poses a much more difficult technological challenge than optical astronomy because of the strong ambient background³. Rapid advances in IR detectors in the last decade have finally made it possible to take full advantage of the proximity of the Galactic MBH. Individual stars can now be tracked as they orbit the MBH in the very crowded stellar field around it. Their mass, age and evolutionary stage can be determined from their spectral features, and their radial (line-of-sight) velocities can be measured from their Doppler-shifted spectra.

Because of the huge mass ratio between a star and the MBH, stars orbiting near it are effectively test particles. This is to be contrasted with the gas in that region, which can be subject to non-gravitational forces due to thermal, magnetic or radiation pressure. These can complicate the interpretation of dynamical data and limit its usefulness. The term “near” is taken here to mean close enough to the MBH so that the gravitational potential is completely dominated by it, but far enough so that the stars can survive

²The K -band is centered on $2.2 \mu\text{m}$ and is $0.6 \mu\text{m}$ wide. The absolute (intrinsic) K -band magnitude, M_K , is related to the monochromatic luminosity at $2.2 \mu\text{m}$, L_K , by $M_K = -2.5 \log_{10} L_K + 84.245$, for L_K in $\text{erg s}^{-1} \mu\text{m}^{-1}$. The apparent (observed) magnitude is related to the absolute one by $K = M_K + \text{DM} + A_K$, where the distance modulus is $\text{DM} = 5 \log_{10}(R_0/10 \text{ pc}) = 14.5$ mag for a distance to the GC of $R_0 = 8$ kpc (Eisenhauer et al. 2003) and where $A_K \sim 3$ mag is the K -band dust extinction coefficient in the direction of the GC (Rieke et al. 1989). For the Sun, $M_{K\odot} = 3.41$ and $L_{K\odot} = 2.154 \times 10^{32} \text{ erg s}^{-1} \mu\text{m}^{-1}$.

³History and economics also played a role. Optical astronomy had a long head-start over IR astronomy, which had to wait for the advent of modern electronics and cryogenics. In addition, the market for IR devices is much smaller than that for optical ones. As a result, the development of efficient IR detectors lagged decades behind optical detectors.

(that is, beyond the MBH event horizon, or beyond the radius where stars are torn apart by the tidal field). In this range, stars directly probe the gravitational field of the MBH as long as their trajectory does not take them so close to the MBH that dissipative processes, such as tidal heating, affect their motion. The event horizon of the MBH in the GC is much smaller than the tidal radius for most stars, and so effects due to General Relativity (GR) lead to deviations of only a few percents from Newtonian motion. To first order, the stellar orbits can be treated as Keplerian, which substantially simplifies the analysis. However, with accurate enough astrometric and spectroscopic observations it may be possible to detect post-Newtonian effects in the orbits and to probe GR.

The stars near the MBH are of interest in themselves, in particular when they can no longer be treated as point particles due to strong interactions with other stars or with the MBH. The observed stellar density near the MBH is extremely high, in accordance with theoretical predictions of the stellar distribution near a MBH. The presence of so many stars so close to the MBH leads to a variety of interactions between the MBH and the stars, which may be relevant for feeding the MBH and can potentially produce an observable signal of the MBH existence. The high density, large orbital velocities and strong tidal field, well above those in any other Galactic environment, effectively make the central ~ 0.1 pc of Galaxy a “stellar collider”. In this extreme environment, otherwise rare dynamical processes that can affect the inner structure of stars occur relatively frequently. The formation and evolution of stars in the extreme environment so close to the MBH challenge theories of stellar dynamics and star formation.

The Galactic MBH and the stellar environment around it are probably representative of many similar systems in the universe. It is therefore likely that insights gained from the study of this uniquely accessible system can be applied to MBHs in general. In particular, insights about the role that stars near MBHs play in the feeding, growth and evolution of the MBH and the galactic nucleus.

1.2 Science questions

The study of the stars near the MBH in the GC offers an opportunity to address many specific questions in the general themes mentioned above. These broadly fall in four categories.

The nature of the dark mass The identification of a BH is mainly done by eliminating all other possibilities, and so an inquiry into the nature of the dark mass must begin by measuring its primary parameters: mass, size, position and velocity (§4). The measured compactness of the mass distribution can discriminate between a BH and other alternatives (§4.2). The central dark mass may be composed of several components that have to be disentangled, for example a binary MBH (§4.3), or a single MBH surrounded by a dense cluster of stellar mass compact remnants and a dark matter cusp of elementary particles (§4.2.2, §4.2.3). The position and velocity of the dark mass, which lies at the dynamical center of the Galaxy, are also primary parameters for reconstructing the Galactic structure and rotation and for calibrating distance indicators (§4.1.3).

Post-Newtonian physics Stellar orbits very near the MBH should display post-Newtonian deviations such as periape angle shifts, Lense-Thirring precession or gravitational redshift, and thus test various aspects of GR (§5.1). Compact remnants and low-mass main sequence (MS) stars inspiraling into the MBH could emit detectable gravitational wave (GW) radiation (§6.2.2). The deflection of light by the gravitational potential of the MBH may be detected by gravitational lensing effects (§5.2).

Formation and growth of MBHs Observations of stars can provide clues on the way the MBH forms and grows. Gas can be supplied by stellar winds from nearby giants or young massive stars, or by stars passing very near the MBH (§2.2, §6.2.4). The efficiency of tidal disruption and capture

can be probed by searching for stars that are in the process of being captured (§6.2.3) or have narrowly avoided such fate (§6.2.4). Stars can interact with a cold remnant accretion disk and reveal its existence (§6.2.5). The MBH may also grow by merging with other BHs, whether stellar mass BHs (SBHs) (§3.3) or intermediate mass black holes (IBHs) (§4.3, §7.2.3).

Stars under extreme conditions the unique and extreme conditions near the MBH (§3) may be the reason behind the unusual stellar populations observed there. Observations may reveal evidence for processes such as extreme mass segregation (§3.3), collisional destruction (§3.4.1), tidal spin-up (§3.4.2) or 3-body exchanges (§7.2.4) and provide new insights about unusual modes of star formation near a MBH (§7.2.1).

1.3 Scope and connections to related topics

The GC is a complex interacting system. Its different components, processes and regions are interrelated. Many of the topics discussed below can be expanded to apply to MBHs in general. Keeping this review focused on stellar processes near the Galactic MBH inevitably involves setting somewhat arbitrary limits to its scope.

This review deals with stellar processes in the inner 1–2 parsecs of the GC, where the MBH dominates the dynamics, and in particular in the innermost region where stars can still exist. Stellar processes near a MBH may result in observable effects and thus provide methods for detecting MBHs. However, some of the effects discussed below are rather subtle and their usefulness in investigating stellar dynamics near the MBH is limited to the GC, as it is unlikely that they could be observed with comparable precision near MBHs in other galaxies.

In spite of the fact that stars are born of gas and dust and to gas and dust (and compact remnants) return, gas processes, such as accretion and outflows, will be discussed only to the extent that they are directly related to stellar processes near the MBH. Observations of the Milky Way and a few nearby galaxies show that distinct stellar populations exist near their MBH (Lauer et al. 1998). It is likely that the environment near a MBH affects the mechanisms of star formation. However, star formation is poorly understood even in typical galactic environments, let alone near a MBH, and will be discussed here only briefly.

The discussion will focus on low mass MBHs ($m \lesssim 10^8 M_\odot$), like the Galactic MBH, where the tidal disruption radius (for solar type stars) lies outside the event horizon. This allows the possibility of tidal disruption and limits the role of GR in the dynamics of stars near the MBH. This situation is not generalizable to massive MBHs ($m \gtrsim 10^8 M_\odot$), which are qualitatively different in these respects. At the other end of the mass spectrum lie IBHs ($10^2 \lesssim m \lesssim 10^4 M_\odot$), whose existence is still a matter of speculation (e.g. Kaaret et al 2001; Hopman, Portegies-Zwart & Alexander 2004; Portegies Zwart et al. 2004; see review by Miller & Colbert 2004). IBHs will also not be discussed here, except where related directly to the GC. Likewise, although major (comparable mass) MBH mergers and binary MBHs may play an important role in the evolution of MBHs in general (e.g. Merritt & Milosavljević 2004), it seems unlikely that this is relevant for the low mass Galactic MBH and the steep stellar cusp around it, and so this topic will be mentioned only briefly here.

Additional information and discussion of some of the topics outside the scope of this review can be found in other reviews about the GC: Genzel & Townes (1987; early general review on inner 10 pc); Genzel, Hohlenbach & Townes (1994; comprehensive review with focus on stellar and gas processes); Morris & Serabyn (1996; focus on large spatial scales, gas and star formation); Melia & Falcke (2001; focus on accretion and the radio source Sgr A*); Yusef-Zadeh, Melia & Wardle (2000; focus on interactions between stars, gas, dust, clouds and supernovae remnants) and Alexander (2003; focus on stellar phenomena). More observational and theoretical background can be found in Falcke & Hehl (2003).

The acronyms and notations used in this review follow where possible the usual conventions in the literature. For convenience, the ones frequently used here are listed in table (1.1).

2 Observational overview: Stars in the Galactic center

The observational picture of the GC, and in particular that of the central few parsecs, is a rapidly evolving one. A too detailed focus on the most recent observations runs the risk of premature obsolescence, as ongoing observational campaigns continuously yield new data and insights. This overview will therefore be limited to painting a broad-brush picture, and defer detailed discussion to the relevant topical sections below.

It is useful to begin by a brief summary of some stellar properties that are of particular relevance in this context. The initial stellar mass sets the stellar lifespan, and together the two determine which dynamical processes are relevant (for example, a slow dynamical process that operates on massive objects may be irrelevant because the massive stars are too short-lived, while the long-lived stars are not massive enough). The initial mass also sets the evolution of the stellar IR luminosity, which determines if, and at which evolutionary stage the star can be observed. Figure (2.1) shows the stellar lifespan, the MS K -band luminosity and the MS spectral type designation as function of initial stellar mass, compared to the estimated dynamical two-body relaxation time in the GC and compared to current and future K -band detection limits (for evolved stars, see Fig. 3.5 in Genzel, Hollenbach & Townes 1994).

2.1 The central 100 parsecs

The stars well outside the dynamical sphere of influence of the Galactic MBH on the $\lesssim 100$ pc scale are relevant for understanding the stellar environment in the inner parsec because they define the “boundary conditions” for the inner GC; because, given enough time or under certain dynamical conditions (§3.3) stars can migrate from large distances to the center, and because the stellar population far from the MBH can serve as a control sample for separating the effects of the MBH from intrinsic stellar phenomena.

The GC lies at the center of the Galactic bulge (typical length-scale ~ 2 kpc), which is composed of an old (~ 10 Gyr), passively evolving stellar population. However, the stellar population in the central ~ 100 pc, whose density rises toward the center as r^{-2} , appears to have been forming continuously over the lifetime of the Galaxy. The star formation is probably fed by the large reservoir of molecular gas (the central molecular zone) that is concentrated in the inner ~ 200 pc (Serabyn & Morris 1996). The stellar population in the GC is thus a mixture of the inner extension of the old bulge population and intermediate-age and young stars from more recent star formation epochs (Philipp et al. 1999; Mezger et al. 1999; Figer et al. 2004).

About half of the young stars in the region are found today in three particularly massive, young ($\lesssim 5$ Myr) clusters: The Quintuplet (~ 30 pc from the center in projection, $M \sim 10^4 M_\odot$, $\bar{\rho} \sim \text{few} \times 10^3 M_\odot \text{pc}^{-3}$), The Arches (~ 30 pc from the center in projection, $M \gtrsim 10^4 M_\odot$, $R \sim 0.2$ pc, $\bar{\rho} \sim 3 \times 10^5 M_\odot \text{pc}^{-3}$), and the central cluster around the MBH (Figer 2003). The three clusters contain in total hundreds of MS O-stars, tens of Wolf-Rayet (WR) stars and a few luminous blue variable stars (§2.2), which are $\sim 10\%$ of all the massive stars (initial mass $> 20 M_\odot$) in the entire Galaxy. They produce $\sim 10\%$ of the Galactic ionizing luminosity, and are responsible for the formation of $0.01 M_\odot \text{yr}^{-1}$ in stars (a rate per volume of $\sim 10^{-7} M_\odot \text{yr}^{-1} \text{pc}^{-3}$, 250 times higher than the Galactic mean). This is however only $\sim 1\%$ of the total Galactic star formation rate. The disparity reflects the marked bias in the initial mass function of these clusters toward the formation of massive hot and luminous stars (Figer et al. 1999; Figer 2005). The overall similarity between the young stellar populations of the Arches and the Quintuplet and that of the central cluster (§2.2) is noteworthy in view of the fact that the two off-center clusters show no evidence of harboring a central BH.

Table 1.1: Acronyms and notation frequently used in this review (by topic, alphabetically)

Term	Defined	Meaning	Term	Defined	Meaning
Acronyms			Stellar dynamics		
AGN		Active Galactic Nucleus	J	p. 18	Specific angular momentum
BH		Black hole	n_*	p. 16	Stellar number density
DF		Distribution function	r_{coll}	p. 15	Collisional radius
GC		Galactic center	t_c	p. 16	Collision time
GR		General Relativity	t_e	p. 16	Evaporation time
GW		Gravitational waves	t_J	p. 59	Angular mom. relaxation time
IBH		Intermediate mass black hole	t_r	p. 16	Relaxation time
IMF		Initial mass function	t_s	p. 16	Mass segregation time
IR		Infrared	α	p. 19	Logarithmic slope of n_*
MBH		Massive black hole	ε	p. 17	Specific orbital energy
MS		Main sequence	ρ	p. 20	Mass density
NS		Neutron star	σ	p. 15	1D stellar velocity dispersion
SBH		Stellar black hole	ψ	p. 17	Relative gravitational potential
WD		White dwarf	Stellar astrometry and orbits		
WR		Wolf-Rayet star	a	p. 18	Keplerian semi-major axis
Stellar properties			e	p. 18	Keplerian eccentricity
E_*	p. 27	Stellar binding energy	i	p. 36	Inclination angle
K	p. 4	K -band magnitude	p	p. 33	Projected distance from MBH
L_*	p. 25	Total stellar luminosity	P	p. 18	Keplerian orbital period
M_*	p. 14	Stellar mass	r_p	p. 27	Orbital periape
N_*	p. 17	Number of stars	r_a	p. 35	Orbital apoapse
R_*	p. 14	Stellar radius	z	p. 33	Line of sight distance from MBH
t_*	p. 9	Stellar lifespan	β	p. 46	Velocity in terms of speed of light c
T_*	p. 25	Effective temperature	Υ	p. 46	Relativistic parameter
V_e	p. 15	Stellar escape velocity	Star–MBH interactions		
V_*	p. 61	Stellar circular velocity	b^{-1}	p. 57	Tidal penetration parameter
τ_*	p. 27	Stellar dynamical timescale	r_t	p. 15	Tidal disruption radius
MBH properties			Γ_s	p. 75	Tidal scattering rate
m	p. 14	MBH mass	Γ_t	p. 59	Tidal disruption rate
r_h	p. 15	MBH radius of influence	τ_p	p. 27	Periape passage timescale
r_S	p. 15	Schwarzschild radius	Gravitational lensing		
s	p. 49	Spin parameter	A	p. 51	Lensing magnification
GC properties			D_{LS}	p. 50	Lens–source distance
A_K	p. 4	K -band dust extinction	D_{OL}	p. 50	Observer–lens distance
DM	p. 4	Distance modulus	D_{OS}	p. 50	Observer–source distance
R_0	p. 4	Sun–GC distance	x	p. 51	Image angular position in terms of θ_E
t_H	p. 15	Hubble time (\sim age of GC)	y	p. 51	Source angular position in terms of θ_E
Θ_0	p. 39	Local Galactic rotation speed	Γ_L	p. 52	Gravitational lensing rate
			θ_E	p. 50	Einstein angle

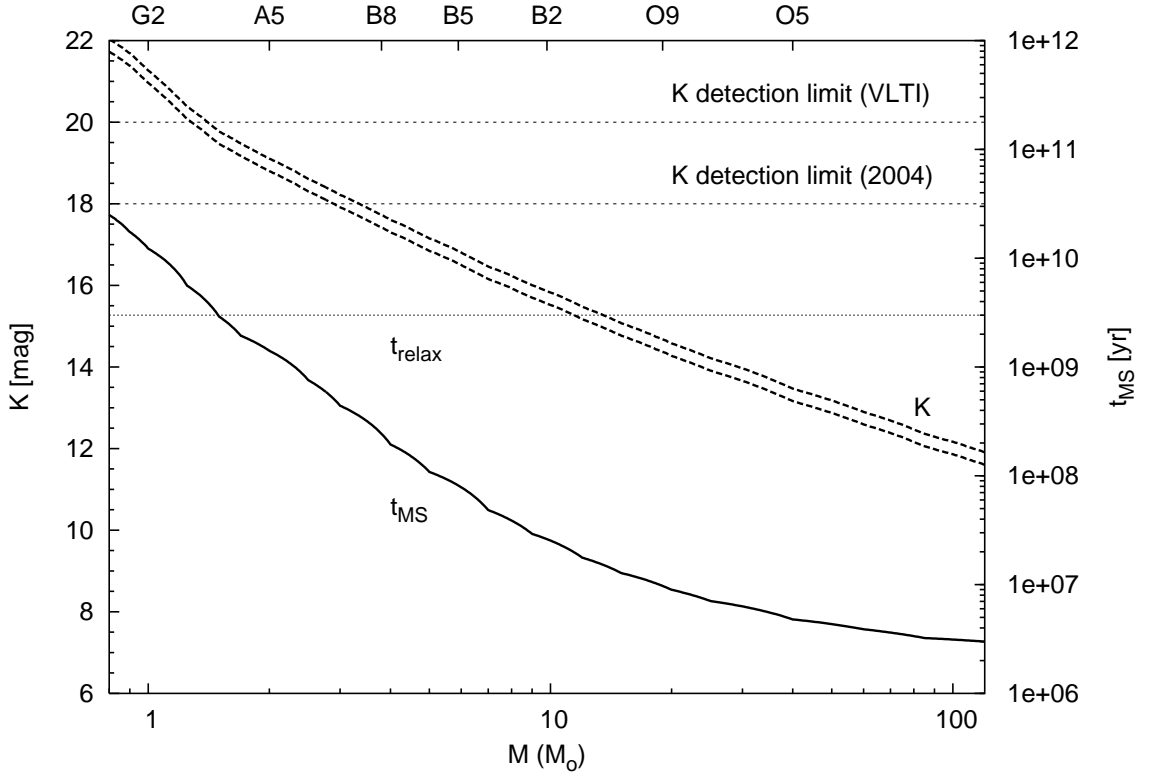


Figure 2.1: Main sequence lifetime and K -band magnitude for zero-age solar metallicity stars (based on the stellar tracks of Schaller et al. 1992). An approximate association of mass with spectral type is indicated in the upper horizontal axis (Cox 2000). The apparent K -band magnitudes are given for a plausible range of distance and extinction coefficient values: the top curve for the fiducial distance to the GC of $R_0 = 8$ kpc (Reid 1993; Eisenhauer et al. 2003) and K -band extinction of $A_K = 3$ mag (Rieke et al. 1989), and the bottom curve for the more recent determination of $R_0 = 7.62$ kpc and $A_K = 2.8$ mag. A rough estimate of the two-body relaxation time in the GC, $t_r \sim 3 \times 10^9$ yr (Alexander 1999), the current detection limit in the K -band with the VLT ($K = 18$ mag with completeness of 63%, Genzel et al. 2003b) and the anticipated limit for the VLTI interferometer with adaptive optics (Paresce et al. 2003) are also shown.

X-Ray observations of the inner 20 pc also reveal ~ 2000 X-ray sources, which follow the distribution of the stars in the IR. The hard spectral index of over half of these sources suggests that they are magnetically accreting white dwarfs (WDs) and X-ray pulsars in high mass X-ray binaries (where a neutron star (NS) accretes the wind of a massive companion).

It is useful to construct a stellar population model to represent the continuously star forming population of the central GC. When the star formation rate is constant, the present-day mass function (number of stars per stellar mass) at time t is simply related to the initial mass function (IMF) dN_*/dM_* by

$$\left. \frac{dN_*}{dM_*} \right|_t \propto \left. \frac{dN_*}{dM_*} \right|_0 \min[t, t_*(M_*)], \quad (2.1)$$

where t_* is the stellar lifespan. The stellar contents of such a model are listed in table (2.1). This model

Table 2.1: A mean stellar population model for the inner GC^a

Component	Mass fraction ^b	Number fraction ^c	Notes
Gas consumed	1.8	—	Including reprocessed gas
Gas reprocessed	0.8	—	Assumed ejected from GC
Live stars ($M_* > 0.1 M_\odot$)	0.74	0.85	Mean mass $0.43 M_\odot$
Live stars ($M_* > 0.8 M_\odot$)	0.22	0.13	Mean mass $0.84 M_\odot$
Compact remnants ^d	0.27	0.15	Mean mass $0.94 M_\odot$
WDs ^e ($0.6 M_\odot$)	0.03	0.03	Progenitor mass $0.8\text{--}1.5 M_\odot$
WDs ^e ($0.7 M_\odot$)	0.08	0.06	Progenitor mass $1.5\text{--}2.5 M_\odot$
WDs ^e ($1.1 M_\odot$)	0.12	0.05	Progenitor mass $2.5\text{--}8.0 M_\odot$
NSs ^e ($1.4 M_\odot$)	0.03	0.01	Progenitor mass $8.0\text{--}30 M_\odot$
SBHs ^f ($10 M_\odot$)	0.01	0.0005	Progenitor mass $> 30 M_\odot$

^a Continuous star formation over 10 Gyr at a constant rate with a Miller-Scalo IMF (Miller & Scalo 1979) and solar metallicity (Alexander & Sternberg 1999). Calculated by a stellar population synthesis code (Sternberg, Hoffman & Pauldrach 2003) using the Geneva stellar evolution tracks (Schaller et al. 1992).

^b Relative to total remaining mass in stars and remnants.

^c Relative to total remaining number of stars and remnants.

^d Average supernovae rate of $1.2 \times 10^{-5} \text{ yr}^{-1}$ per $10^7 M_\odot$ of gas consumed.

^e Meylan & Mayor (1991).

^f Timmes, Woosley & Weaver (1996).

assumes a 10 Gyr old, continuously star forming population with a Miller-Scalo⁴ IMF (1979) and solar metallicity. The K -band luminosity function (number of stars per magnitude) of this model is well approximated by a power-law down to faint magnitudes ($K \lesssim 20$ mag), $d \log N_*/dK = s$, with $s \simeq 0.35$ (Alexander & Sternberg 1999). This value broadly agrees with the observed K -band luminosity function in the inner 0.25 pc (Davidge et al. 1997) and that of the Galactic bulge as observed through Baade’s window, ~ 0.5 kpc from the GC (Tiede, Frogel & Terndrup 1995; Zoccali et al. 2003).

2.2 The central parsec

The central parsec lies inside the dynamical sphere of influence of the MBH (§3.1.2). The properties of the stellar population there are observed to change with decreasing distance from the MBH, once at ~ 0.4 pc and then again at ~ 0.04 pc (Fig. 2.2).

Both the stellar spatial distribution and the stellar population outside ~ 0.4 pc are a continuation of the large scale $n_* \propto r^{-2}$ mixed distribution of old and young stars in the inner 100 pc (Genzel et al. 2003b). The old population is dynamically relaxed and follows the Galactic rotation pattern (McGinn et al. 1989; Haller et al. 1996; Genzel et al. 1996).

Inside ~ 0.4 pc the stellar spatial distribution flattens to $n_* \propto r^{-1.4}$ (Genzel et al. 2003b). On approximately the same length-scale (whether or not this is a coincidence is unclear), there appears a dominant population of massive young stars (Forrest et al. 1987; Allen, Hyland & Hillier 1990; Krabbe et al. 1995; Paumard 2004). This population consists of dynamically unrelaxed blue supergiants with distinctive helium emission lines in their infrared spectra (Tamblyn 1996; Genzel et al. 1996; Genzel

⁴A useful analytic approximation of the normalized Miller-Scalo IMF (1979) is $\ln(dN_*/dM_*|_0) = -\ln(2M_*/M_\odot)\ln(400M_*/M_\odot)/4 - 7.11$ for $0.1 < M_*/M_\odot < 125$.

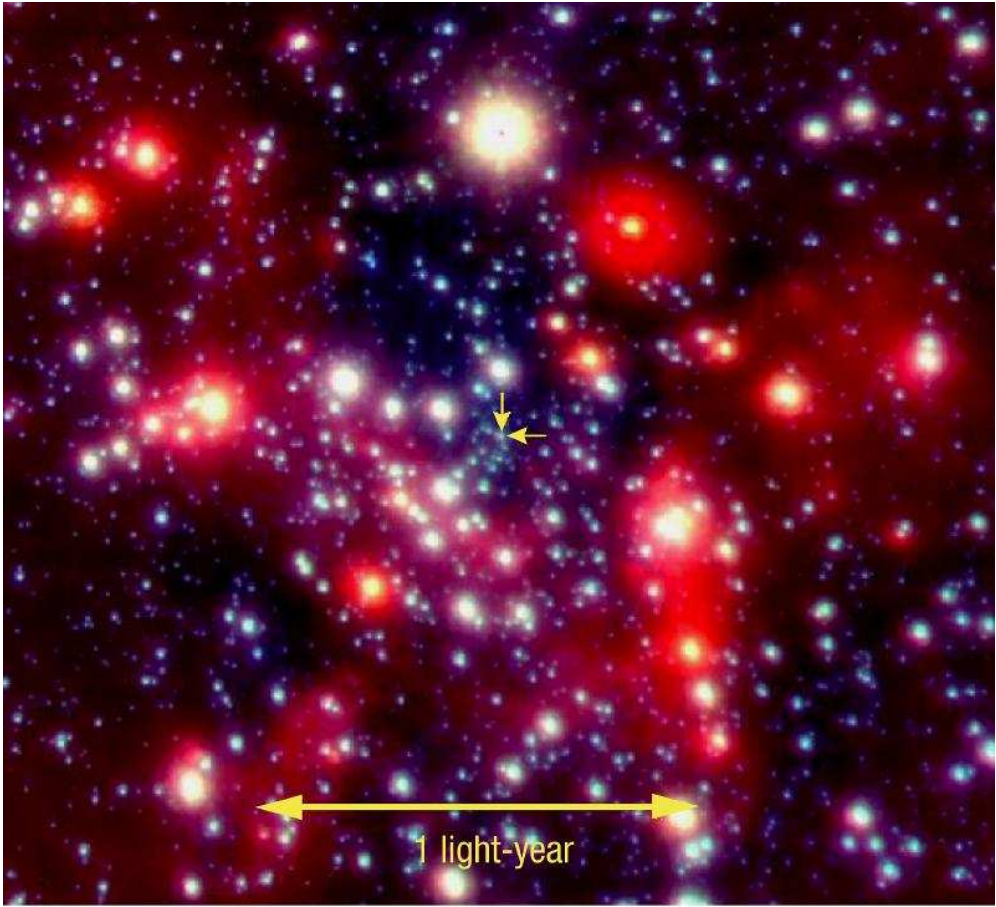


Figure 2.2: A false color composite image of the central parsec of the GC taken by the Very Large Telescope in the H ($1.65\,\mu\text{m}$), K_s ($2.16\,\mu\text{m}$) and L' ($3.76\,\mu\text{m}$) infrared bands (Genzel et al. 2003b). The position of the MBH is indicated by the two small arrows. A mixture of stellar types is clearly apparent: Old, intermediate mass cool red giants and young massive hot blue stars. (Reprinted with permission from the *Astrophysical Journal*)

et al. 2000). The lack of hydrogen lines and evidence of outflow in the spectral line shapes (“P Cygni profiles”) identify them as WR stars or Luminous Blue Variables (LBVs) (Najarro et al 1997). WRs are stars with masses of order $\text{few} \times 10 M_\odot$, lifespans of $\text{few} \times 10^6$ yr undergoing rapid mass loss by a stellar wind, which removes the hydrogen-rich envelope and uncovers the helium-rich core. LBVs are WR progenitors that are still in the process of losing their envelopes. There are tentative detections of X-ray emission from the shocked winds of a couple of these stars (Baganoff et al. 2003).

The emission line stars co-rotate tangentially in an opposite direction to the Galactic rotation, in two partially overlapping disk-like structures (Levin & Beloborodov 2003; Genzel et al. 2003b; Fig. 2.3). The two disks are strongly inclined relative to each other. In projection on the plane of the sky, the inner disk appears to rotate clock-wise, and the outer disk counter-clockwise. The inner extent of the disk population is ~ 0.04 pc. Two prominent concentrations of stars appear among the disk stars. The IRS16 complex is located on the line-of-nodes (the intersection between the disk plane and the plane of the sky) of the clockwise disk, and so this apparent stellar over-density can plausibly be explained as a projection effect (Genzel et al. 2005, in prep.). The IRS13 complex is part of the counter-clockwise disk, which is nearly face-on. IRS13 appears to be a genuine over-concentration of stars with common

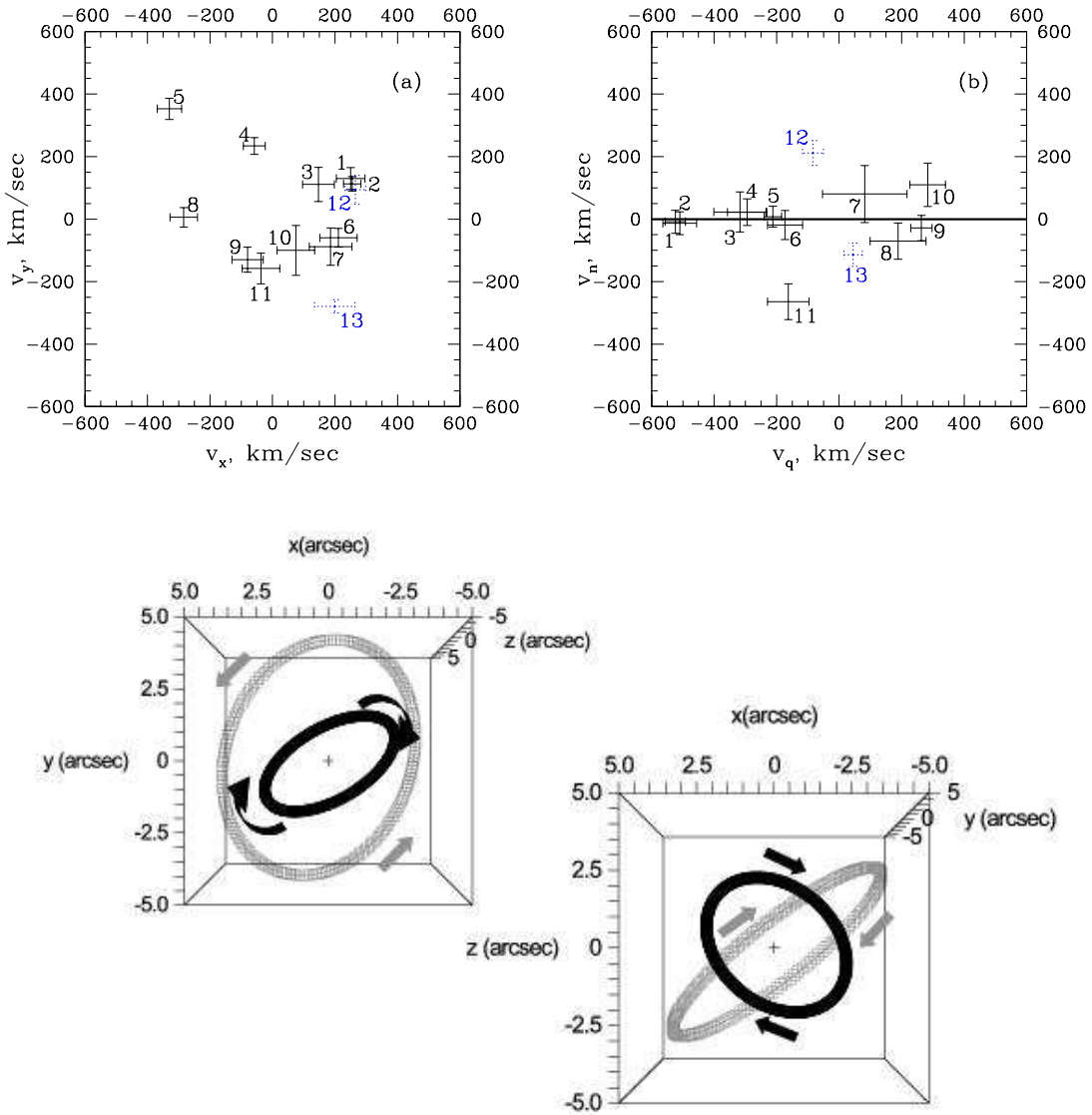


Figure 2.3: Evidence for disk-like stellar structures around the Galactic MBH. Top left: Distribution in projected velocity space of 13 bright emission line stars in the inner $\sim 5''$ from a compilation by Genzel et al. (2000). Top right: The same, after transforming to the disk coordinates. 10 of the 13 stars lie in a thin disk with opening angle $\lesssim 10^\circ$. (Levin & Beloborodov 2003. Reprinted with permission from the *Astrophysical Journal*). Bottom: Reconstructed orientations of the the inner clockwise ring and the outer counter-clockwise disk (Genzel et al. 2003b. Reprinted with permission from the *Astrophysical Journal*), shown from two vantage points. The coordinates x and y are in the plane of the sky, and z is along the line of sight, with the observer at $z = -\infty$.

velocities (Maillard et al. 2004; Schödel et al. 2005).

Inside ~ 0.04 pc the population changes again. There are no bright giants, red or blue, and only faint blue stars are observed there. This population is known as the “S-stars” or “S-cluster”, after their

identifying labels⁵. Deep near-IR photometric (Krabbe et al. 1995; Genzel et al. 2003b) and spectroscopic (Genzel et al. 1997; Eckart, Ott & Genzel 1999; Figer et al. 2000; Gezari et al. 2002; Ghez et al. 2003b) observations of that region were all consistent with the identification of these stars as massive MS stars. It is now spectroscopically confirmed (Ghez et al. 2003b; Eisenhauer et al. 2005) that the S-stars are B0–B9 MS stars (corresponding to masses in the range $\sim 3M_{\odot}$ – $\sim 15M_{\odot}$). The rotational velocities (stellar spin) are similar to those of Solar neighborhood stars of the same spectral type. Thus, there is no indication of anything unusual about the S-stars, apart for their location very near the MBH. Astrometric observations (Ghez et al. 2005; Schödel et al. 2003; Eisenhauer et al. 2005) indicate that, unlike the emission line stars farther out, the S-stars orbits appear random (isotropic) and uncorrelated with the orientation of either disk. There are some marginal statistical indications of a bias toward radial orbits (Genzel et al. 2000; Schödel et al. 2003, but see Ghez et al. 2005).

The brightest star in the S-cluster, S2/S0-2 ($K=13.9$ mag), is a transitional O8–B0 star with a mass of $\sim 15M_{\odot}$, effective temperature of $\sim 30,000$ K, intrinsic bolometric luminosity of $L \sim 10^3 L_{\odot}$ and a main sequence lifespan of $\sim 10^7$ yr. All the other stars in the cluster are less massive, longer-lived, cooler and fainter. A B9 MS star has a mass of $\sim 3M_{\odot}$, a radius of $\sim 2.1R_{\odot}$ and a main sequence lifespan of $\sim 4 \times 10^8$ yr. A typical star would correspond to a B2 main sequence star, with a mass of $\sim 10M_{\odot}$, a radius of $\sim 4.5R_{\odot}$ and main sequence lifespan of $\sim 2 \times 10^7$ yr (Cox 2000; Schaller et al. 1992). It is not clear what is the relation, if any, between the population of the He stars on the 0.04–0.4 pc scale and the S-cluster stars inside 0.04 pc. The nature and origin of the young stars near the MBH are the subject of ongoing investigations (§7).

3 Stellar dynamics at extreme densities

The extreme conditions in the central ~ 0.1 pc around the MBH are unique in the Galaxy. The strong tidal field (total disruption of a solar type star at a distance ten times the event horizon), high velocities (up to $\sim 0.2c$ at disruption) and high stellar density (up to $\sim 10^8 M_{\odot} \text{pc}^{-3}$, 10^9 higher than in the vicinity of the Sun) effectively make the environment near the MBH a “stellar collider” (a total stellar collision rate of $\mathcal{O}(10^{-5}) \text{yr}^{-1}$ in the central 0.02 pc). Under such extreme conditions, strong stellar interactions may probe and modify the stars’ internal structure, and otherwise rare dynamical processes may become frequent enough to have observable consequences. Before discussing the evidence for the existence of a high density cusp in the GC (§3.2) and its consequences for stellar collisions (§3.4), it is useful to review briefly the physical processes and scales that govern the evolution of a stellar system around a MBH.

3.1 Physical processes and scales

3.1.1 Dynamical processes

The dynamical processes in a gravitating stellar system can be summarized by classifying stellar interactions by their distance scale (e.g. Binney & Tremaine 1987; Heggie & Hut 2003). In this context the term interaction refers both to remote gravitational interactions where the stars exchange momentum and energy, as well as actual physical contact between stars.

⁵Two labeling conventions are used for the IR sources near the MBH, the MPE labels (of the form S#) and the UCLA labels (of the form S#-#, see Ghez et al. 1998). The dual labels of some stars of special interest very near the MBH are listed here for convenience.

MPE:	S1	S2	S4	S8	S9	S11	S12	S13	S14
UCLA:	S0-1	S0-2	S0-3	S0-4	S0-5	S0-9	S0-19	S0-20	S0-16

On the largest scale, the stellar orbit is determined by the superposed interactions with the MBH and all the other stars, which are well approximated by a smooth gravitational potential. On a shorter scale, the stellar motions are randomized by two-body scattering when two stars approach each other so that their mutual interaction dominates that of the smoothed potential. Over time, scattering leads to the relaxation of the system and the redistribution of energy and angular momentum. Massive perturbers, such as stellar clusters, IBHs or molecular clouds can accelerate the relaxation (Zhao, Haehnelt & Rees 2002). In addition, very near the MBH, where the orbits are nearly Keplerian, angular momentum relaxation (but not energy relaxation) can be accelerated by the process of “resonant relaxation” (Rauch & Tremaine 1996). In the course of relaxation, the stars, whose mass range spans 2–3 orders of magnitude, are driven toward energy equipartition. However, equipartition cannot be achieved in a self gravitating system, and in particular in the steep potential well of a MBH. A two-body interaction will tend to slow down the heavier star and speed up the lighter one, but since the typical orbital radius depend only on the velocity (specific energy), the heavy star will sink to the center, while the lighter star will drift outward. Over time, this process leads to mass segregation—the more massive stars are concentrated near the MBH and the lighter stars are pushed out of the inner region.

The system continuously loses stars by two-body scattering, either abruptly, by a single strong encounter that ejects a star, or gradually, by diffusion to higher energies (evaporation). The lost star takes away positive energy from the system. The system then becomes more bound and compact, the collision rate increases, yet more stars are lost, and a runaway process is launched. This so called “gravothermal catastrophe” or “core collapse” reflects the fact that a self-gravitating system has a negative heat capacity—it become hotter when energy is taken out. Core collapse, if unchecked, will lead to the formation of an extremely dense stellar core surrounded by a diffuse extended halo.

Once the density becomes high enough, very short-range inelastic collisions are no longer extremely rare, and the fact that the stars are not point masses, but extended objects with internal degrees of freedom, becomes significant. In such collisions energy is extracted from the orbit and invested in the work required to raise stellar tides, or strip stellar mass. The outcome of inelastic collisions depends critically on whether a MBH is present or not. If the collision is slow, as it is in the core of a globular cluster where there is no MBH, then the typical initial orbit is just barely unbound (parabolic). In this case, the tidal interaction may extract enough orbital energy for “tidal capture”, and the formation of a binary. However, when the stars orbit a central MBH, the collisions are fast (The Keplerian velocity near the MBH exceeds the escape velocity from the star) and the initial orbits are very unbound (hyperbolic). Even very close fly-bys cannot take enough energy from the orbit to bind the two stars, and so they continue on their way separately after having extracted energy and angular momentum from the orbit. The stars can radiate away the excess heat on a time scale shorter than the mean time between collisions, but it is harder to get rid of the excess angular momentum. It is therefore likely that high rotation is the longest-lasting dynamical after effect of a close hyperbolic encounter, and that stars in a high density cusp are spun-up stochastically by repeated collisions (§3.4.2). Finally, at zero range, almost head-on stellar collisions can lead to the stripping of stellar envelopes (§3.2), the destruction of stars, or to mergers that result in the creation of “exotic stars”. These are stars that cannot be formed in the course of normal stellar evolution, such as a Thorne-Żytkow object, which is an accreting neutron star (NS) embedded in a giant envelope (Thorne & Żytkow 1975).

3.1.2 Characteristic scales

Several important length-scales and timescales govern the dynamics of the stellar system around the MBH. These are listed here, with estimates of their values in the GC. A star of mass $M_\star = 1 M_\odot$ and radius $R_\star = 1 R_\odot$ and a MBH mass of $m = 3.5 \times 10^6 M_\odot$ (Schödel et al. 2003) are assumed. Physical lengths are expressed also as angular sizes for a distance to the Galactic Center of $R_0 = 8 \text{ kpc}$, which

corresponds to $1'' = 0.039$ pc (Eisenhauer et al. 2003).

Event horizon The size of the event horizon of a non-rotating black hole, the Schwarzschild radius, is

$$r_S = \frac{2Gm}{c^2} = 10^{12} \text{ cm} \sim 3 \times 10^{-7} \text{ pc} \sim 9 \mu\text{arcsec}. \quad (3.1)$$

Tidal radius The tidal radius, r_t , is the maximal distance from the MBH where the tidal forces of the MBH can overwhelm the stellar self-gravity and tear the star apart. Its exact value depends somewhat on the stellar structure and the energy of the orbit, but up to a factor of order unity it is

$$r_t \sim R_* \left(\frac{m}{M_*} \right)^{1/3} = 10^{13} \text{ cm} \sim 3 \times 10^{-6} \text{ pc} \sim 90 \mu\text{arcsec}. \quad (3.2)$$

Collision radius The collision radius, r_{coll} , is the minimal distance from the MBH where large angle deflections by close gravitational encounters are possible. Closer to the MBH the relative velocity between the interacting stars, v , exceeds the escape velocity from the stellar surface, V_e , and the distance of closest approach required for a large angle deflection becomes smaller than the stellar radius (i.e. when $V_e^2 \sim GM_*/R_* < Gm/r \sim v^2$). Stars undergoing such a physical collision are destroyed since the orbital energy exceeds the stellar binding energy. At distances smaller than

$$r_{\text{coll}} \sim \left(\frac{m}{M_*} \right) R_* \sim 0.08 \text{ pc} \sim 2 \text{ arcsec}, \quad (3.3)$$

two-body relaxation gradually becomes inefficient.

MBH radius of influence The radius of influence, r_h , is the region where the MBH dominates the dynamics. It is customary to define $r_h = Gm/\sigma^2$, where σ is the 1D stellar velocity dispersion away from the MBH. However, in most cases this is not a well defined quantity because σ depends on radius (σ is constant only in an isothermal density distribution, which is not the case in the GC). Kinematically, the MBH potential dominates that of the stars out to a distance where the enclosed stellar mass is $M_*(< r) \sim \mathcal{O}(m)$. For the isothermal distribution $M_*(< r_h) = 2m$. The measured enclosed mass in the GC indicates that $M_*(\lesssim 2 \text{ pc}) \simeq m$ and $M_*(\lesssim 4 \text{ pc}) \simeq 2m$ (Schödel et al. 2003), and so the MBH radius of influence in the GC can be estimated at

$$r_h \sim 10^{19} \text{ cm} \sim 3 \text{ pc} \sim 90 \text{ arcsec}. \quad (3.4)$$

Age of GC It is assumed that the age of the GC, being the center of the old spheroid component of the Galaxy, the bulge, is of the same order as the age of the universe (roughly, the Hubble time),

$$t_H \sim 10 \text{ Gyr}. \quad (3.5)$$

Dynamical timescale The dynamical, or orbital time t_d , is the time it takes a star to cross the system

$$t_d \sim \frac{r}{v} \sim 2\pi \sqrt{\frac{r^3}{GM(<r)}} \sim 2 \times 10^5 \text{ yr (at 3 pc)} \sim 300 \text{ yr (at 0.03 pc)}, \quad (3.6)$$

where r is the typical size of the system and $M(<r)$ is the total enclosed mass (MBH and stars).

Two-body relaxation timescale The two-body relaxation time, t_r , is related to σ , the mean stellar mass $\langle M_\star \rangle$ and the stellar number density n_\star by (e.g. Binney & Tremaine 1987)

$$t_r \sim \frac{0.34\sigma^3}{G^2 \langle M_\star \rangle^2 n_\star \ln \Lambda} \sim \mathcal{O}(10^9 \text{ yr}), \quad (3.7)$$

where a Maxwellian velocity distribution is assumed and $\log \Lambda \sim \mathcal{O}(10)$ is the Coulomb logarithm. Λ is the ratio between the largest and smallest impact parameters possible in the system for elastic collisions⁶. Since near the MBH $\sigma^3 \propto r^{-3/2}$, the relaxation time is not a strong function of r in a stellar cusp where roughly $n_\star \propto r^{-3/2}$, as is the case in the GC (§3.2). The old stars near the MBH are expected to be dynamically relaxed since $t_r < t_H$. The relaxation time can also be approximately expressed in terms of N_\star , the number of stars enclosed within radius r ,

$$t_r(r) \sim \left(\frac{m}{\langle M_\star \rangle} \right)^2 \frac{P(r)}{2\pi \log(0.4N_\star)N_\star}, \quad (3.8)$$

where P is the circular orbital period.

Segregation timescale The mass segregation timescale for stars of mass M_\star is of the same order as the relaxation timescale, and scales with M_\star as (§3.3)

$$t_s \sim t_r \frac{\langle M_\star \rangle}{M_\star} \quad (M_\star > \langle M_\star \rangle). \quad (3.9)$$

Evaporation time The evaporation time scale is

$$t_e \sim 300t_r. \quad (3.10)$$

Evaporation is unimportant in the GC since $t_e \gg t_H$ (and also because the GC is not an isolated system, but is embedded in the bulge, so evaporated stars can be replaced).

Collision timescale The rate, per star, of grazing collisions between two stars of mass and radius M_\star^a , R_\star^a and M_\star^b , R_\star^b , each, is

$$t_c^{-1} = 4\sqrt{\pi}n_\star\sigma \left(R_\star^a + R_\star^b \right)^2 \left[1 + \frac{G(M_\star^a + M_\star^b)}{2\sigma^2 (R_\star^a + R_\star^b)} \right] \sim 10^{-9} \text{ yr}^{-1} \text{ (at } 0.02 \text{ pc)}, \quad (3.11)$$

where it is assumed that the stars follow a mass independent Maxwellian velocity distribution with 1D velocity dispersion σ (this is a good approximation near the MBH, see §3.1.3). The two terms contributing to the total rate are the geometric cross-section and the gravitational focusing term due to the mutual attraction of the colliding stars, which dominates when the typical stellar velocities are much smaller than the escape velocity from the stars. For $M_\star^a = M_\star^b$, this corresponds to $\sigma^2 < GM_\star/2R_\star = V_e^2/4$. The collision rate diverges for $\sigma/V_e \rightarrow 0$ or $\sigma/V_e \rightarrow \infty$ and is lowest when $\sigma/V_e = 1/2$. For the high velocities near the MBH, gravitational focusing is only important for collisions with compact remnants where $R_\star \ll R_\odot$.

⁶The relaxation time can be derived approximately from the rate for large deflection angle collisions, $t_r^{-1} \sim n_\star \sigma \Sigma$, where the cross-section is given by $\Sigma \sim \pi (G \langle M_\star \rangle / \sigma^2)^2$. The actual rate is larger by a factor $\log \Lambda$ due to the additional contribution of the many weaker collisions at large impact parameters.

3.1.3 Keplerian power-law stellar cusps

Theoretical studies of the co-evolution of a MBH and the stellar system around it indicate that a wide range of dynamical scenarios all lead to the formation of a stellar density cusp, a region of diverging density around the MBH (e.g. Bahcall & Wolf 1976; 1977; Young 1980; Lee & Goodman 1989; Quinlan, Hernquist & Sigurdsson 1995). The dynamical evolution of the stars in the radius of influence depends on the ratio between the relaxation time and the age of the system. If $t_r > t_H$, two-body relaxation can be neglected, the MBH grows adiabatically and the resulting stellar distribution depends on the initial conditions. For example, an initially isothermal distribution will give rise to a $n_* \propto r^{-3/2}$ cusp (Young 1980). Other initial conditions will result in a variety of stellar distributions, some falling as steeply as $n_* \propto r^{-5/2}$ (Lee & Goodman 1989; Quinlan, Hernquist & Sigurdsson 1995). However, when $t_r < t_H$, two-body relaxation erases the initial conditions, and the final configuration will depend only on the boundary conditions and the stellar mass function.

The formation history of the Galactic MBH is not known. Estimates of the stellar density and velocity indicate that $t_r < t_H$ near the MBH (§3.1.2), and so the old stars there are expected to have relaxed dynamically by two-body interactions. This is consistent with their observed isotropic velocity field and spatial distribution (Genzel et al 1996; Ghez et al 1998; Genzel et al 2000; §2). The DF of a spherically symmetric system with an isotropic velocity field is a function of ε only. Bahcall & Wolf (1977) show that the distribution function (DF) f (stars per $\text{drd}\mathbf{v}$ interval) of such a system that is relaxed and consists of stellar masses in the range $M_1 < M_* < M_2$ and a moderately varying mass function dN_*/dM_* , can be approximated near the MBH by a power-law with a mass-dependent index

$$f(\varepsilon; M_*) \propto \varepsilon^{p_M}, \quad p_M \equiv \frac{M_*}{4M_2}, \quad (3.12)$$

where $\varepsilon = -v^2/2 + \psi(r)$ is the specific energy of the star, $\psi = -\phi > 0$ is the relative gravitational potential, ϕ is the gravitational potential, and $f=0$ for $\varepsilon < 0$. The power-law index varies in the range $0 < p_M \leq 1/4$ across the mass spectrum. The corresponding stellar number density (stars per dr) is (see Eq. 3.17)

$$n_*(r; M_*) \propto r^{-3/2-p_M}. \quad (3.13)$$

Thus the most massive component of a relaxed multi-mass system is expected to have an $r^{-7/4}$ density profile. and the lightest one an $r^{-3/2}$ density profile. In the simple case of a single mass population ($M_1 = M_2$), $p_M = 1/4$ and $n_* \propto r^{-7/4}$ (Bahcall & Wolf 1976; see also Binney & Tremaine 1987, p. 547 for a simple derivation by dimensional analysis). Note that these results apply also to the Galactic dark matter halo elementary particles in the GC (Gnedin & Primack 2004), which are expected to interact gravitationally with the cusp stars and settle into a $r^{-3/2}$ cusp near the MBH (§4.2.3).

Dynamical simulations (e.g. Murphy Cohn & Durisen 1991; Baumgardt, Makino & Ebisuzaki 2004) confirm that when the population consists of a single stellar mass, or when the most massive stars come to dominate the central stellar mass density due to mass segregation, their DF has indeed a power-law index $p_M \sim 0.25$. The simulations also indicate that the central distribution of the less massive stars is flatter, with $p_M \lesssim 0$. Note that Eq. (3.12) was derived under various assumptions about the boundary conditions far from the MBH and about the stellar mass function, and its general applicability has yet to be investigated in full by numeric simulations. Nevertheless, it will be assumed here to hold generally, since it is broadly consistent with the numerical results and is analytically convenient. Note that the applicability of the Bahcall-Wolf solution to the GC is based on the assumption that the GC has evolved in isolation for at least a relaxation time before the present epoch. In particular, it is assumed that it has not experienced a strong perturbation such as associated, for example, with a merger of two comparable mass galaxies and their MBHs (a “major merger”). This assumption is consistent with the low mass of the MBH, and with the steep stellar cusp observed around it (§3.2), since major mergers are thought to

result in flattened stellar cores due to ejection of stars by the two merging MBHs (Milosavljević et al 2002).

The Bahcall-Wolf solution applies to point particles. This assumption no longer holds very near the MBH, where the collision rate is high because of the very high stellar density and velocity. Stars on tight orbits around the MBH cannot survive for long, and so eventually most of the population there will consist of stars that are on very wide, marginally bound (parabolic) orbits, which spend only a small fraction of their time in the collisionally dominated region. These marginally bound stars have a flatter spatial distribution, of the form (e.g. Binney & Tremaine 1987, p. 551)

$$n_{\star} \propto r^{-1/2}. \quad (3.14)$$

Near the MBH, at $r \ll r_h$ the potential is Keplerian to a good approximation, $\psi(r) = Gm/r$, and the orbits can be characterized by their semi-major axis a (or their period P) and their eccentricity e ($0 \leq e \leq 1$ for bound orbits),

$$a = \frac{Gm}{2\varepsilon}, \quad e^2 = 1 - \frac{J^2}{Gma}, \quad P = 2\pi \sqrt{\frac{a^3}{Gm}}, \quad (m \gg M_{\star}), \quad (3.15)$$

where J is the magnitude of the specific angular momentum, such that the orbital energy is given by

$$\varepsilon = -\frac{1}{2}v^2 + \frac{Gm}{r} = -\frac{1}{2}v_r^2 - \frac{J^2}{2r^2} + \frac{Gm}{r}, \quad (3.16)$$

where v_r is the radial velocity. The stellar densities per $d\mathbf{r}$, $d\varepsilon$ and da that correspond to a DF of the form $f(\varepsilon) = A\varepsilon^p$ (Eq. 3.12) are, respectively, (e.g. Schödel et al 2003, Eqs. A1–A8)

$$\begin{aligned} n_{\star}(r) &= (2\pi)^{3/2} \frac{\Gamma(1+p)}{\Gamma(5/2+p)} (Gm)^{3/2+p} A r^{-3/2-p}, \\ n_{\star}(\varepsilon) &= \sqrt{2}\pi^3 (Gm)^3 A \varepsilon^{p-5/2}, \\ n_{\star}(a) &= 2^{2-p}\pi^3 (Gm)^{3/2+p} A a^{1/2-p}. \end{aligned} \quad (3.17)$$

In the general spatially spherically symmetric case (anisotropic velocity field), the DF $f(\varepsilon, J)$ depends both on ε and J . The distribution of specific energy and angular momentum, $n(\varepsilon, J)$ (stars per $d\varepsilon dJ$) is

$$n_{\star}(\varepsilon, J) = 8\pi^2 J f(\varepsilon, J) P_r(\varepsilon, J), \quad (3.18)$$

where P_r is the radial period. For Keplerian orbits $P_r = P$ and the distribution of specific energy and eccentricity (stars per $d\varepsilon de$) is (cf Cohn & Kulsrud 1978)

$$n_{\star}(\varepsilon, e) = \left[2\sqrt{2}\pi^3 (GM)^3 f(\varepsilon, J) \varepsilon^{-5/2} \right] e, \quad (3.19)$$

It then follows that for Keplerian orbits with *isotropic* velocities the normalized distribution of eccentricities $n(e)$ (stars per de interval) is simply (cf Binney & Tremaine 1987)

$$n_{\star}(e) = 2e. \quad (3.20)$$

Thus, isotropically distributed stars on Keplerian orbits tend to have high eccentricities, with a fraction $1 - e^2$ having eccentricities $> e$ (for example, 10% have $e > 0.95$).

The velocity distribution is tied to the spatial density distribution through the Jeans Equation (the continuity equation of the stellar orbits in phase space in terms of the stellar density and velocity dispersion)

$$\frac{v_c^2}{\sigma^2} = -\frac{d \ln n_\star}{d \ln r} - \frac{d \ln \sigma^2}{d \ln r}, \quad (3.21)$$

where $v_c = \sqrt{GM(<r)/r}$ is the circular velocity and a steady state, isotropic, non-rotating system is assumed. The assumption of steady-state is justified because the dynamical timescale is much shorter than the relaxation timescale. The assumptions of approximate isotropy and non-rotation are observationally justified for the old stellar population and for the stars in the central 1'' (§2.2). Since very near the MBH the stellar mass is negligible, $M(<r) \simeq m$, the velocity dispersion is Keplerian, $\sigma^2 \propto r^{-1}$, and the density is a power-law, $n_\star \propto r^{-\alpha}$ (here $\alpha = 3/2 + p$), it follows from the Jeans equation that

$$\sigma_M^2 = \left(\frac{1}{5/2 + p_M} \right) \frac{Gm}{r}. \quad (3.22)$$

This result justifies the approximation that the velocity dispersion in a relaxed stellar system around a MBH is mass-independent, since σ_M^2 changes by less than 10% over the entire mass range, in marked contrast to the $\sigma_M^2 \propto M_\star^{-1}$ dependence of equipartition.

Theoretical arguments indicate that the velocity field of a relaxed system very near a MBH should be approximately Maxwellian and isotropic locally (Quinlan, Hernquist & Sigurdsson 1995). This is indeed observed to be the case in the GC. The measured radial velocity distribution is well fitted by a Gaussian distribution (Genzel et al. 1996) and the measured velocities in the plane of the sky and along the line-of-sight are consistent with an isotropic velocity dispersion (Ghez et al 1998; Genzel et al 2000). The Jeans equation (Eq. 3.21) indicates that the steeper the cusp (larger p_M), the larger v_c/σ , and so the fraction f_u of unbound stars (those with $v > v_e = \sqrt{2}v_c$) is smaller⁷,

$$f_u(p_M) = \sqrt{\frac{2}{\pi}} \int_{\sqrt{5+2p_M}}^{\infty} u^2 e^{-u^2/2} du. \quad (3.23)$$

The fraction of unbound stars varies greatly across the range of interest because the integration over the exponential tail of the Maxwellian distribution depends sensitively on the lower limit. For example, in a flat core ($n_\star \sim \text{const.}$), $f_u(-3/2) \simeq 0.6$, whereas in a steep cusp (e.g. $n_\star \propto r^{-2.5}$), $f_u(1) \simeq 0.07$. Because unbound stars have wide orbits and spend most of their time far away from the MBH, the stellar population in a shallow cusp is well mixed and representative of the average population over a large volume. In contrast, the stellar population in a steep cusp is localized and can therefore develop and maintain properties that differ from those of the general population.

3.2 The stellar cusp in the Galactic center

The basic premise of the attempt to quantify the global properties of the stellar distribution in the inner GC is that there is an underlying quasi-steady state distribution that includes most of the mass and most of the stars, and which is traced by the old faint stars. In contrast, the young stars and bright giants, which dominate the light, are less reliable tracers because they could be far from steady-state, or subject

⁷The stars are bound to the GC as a whole (MBH and stars), but when they approach the MBH they move with $v > v_e$ in the two-body MBH-star system.

to statistical fluctuations due to their small numbers, or susceptible to environmental effects such as stellar collisions or photoionization (Sellgren et al. 1990).

The proximity of the GC allows, in principle, a direct test of the theoretical predictions about the distribution of stars around a MBH. However, even in the GC the derivation of the 3D mass and number density distributions from the observations is hindered by several substantial obstacles.

1. The star counts are inevitably incomplete. Only stars brighter than the detection threshold can be observed. To observe fainter stars, the instrumental photometric sensitivity must be improved, and with it the angular resolution in order to resolve individual stars in the crowded field near the MBH and avoid the source confusion problem. The dynamic range of the detectors must also be increased, otherwise the bright stars in the frame will saturate the detectors and out-shine their faint neighbors. These instrumental requirements can rarely all be satisfied simultaneously. The degree of incompleteness can be estimated and compensated for in the statistical sense, by simulating the detection procedure with mock data.
2. Obscuration (“extinction”) by a non-uniform distribution of interstellar dust can bias the derived stellar distribution. To compensate for such effects, it is necessary to map the dust across the field, for example by comparing the observed stellar colors with their assumed intrinsic ones. The analysis of the extinction gradient across the central parsec suggests that any bias due to dust extinction is unlikely to be large (Alexander 1999; but see strong gradients in extinction maps by Scoville et al. 2003).
3. It is crucial to separate the old and young stars in order make a meaningful comparison to stellar dynamical models, since the two populations are dynamically distinct (§2.2). The phase space distribution of the young stars reflects the initial conditions at birth and their still unknown formation mechanism (§7), whereas the distribution of the old stars has had time to adjust to the presence of the MBH and is probably dynamically relaxed. The stellar type can be determined, at least for the brighter stars, by their spectra or infrared colors.
4. The observed 2D star counts have to be translated to 3D densities. This can be done by first making assumptions about the symmetries of the DF (e.g. spherical symmetry and isotropic velocity; Genzel et al 1996), deprojecting the observed surface density and line of sight velocity dispersion (Eq. 4.2) and relating the deprojected quantities to the enclosed mass via the Jeans equation (Eq. 3.21). Alternatively, the star counts can be fitted to a projected 3D model distribution with a small number of free parameters (e.g. a broken power-law cusp), for example by maximal likelihood criteria (Alexander 1999; Genzel et al 2003b; see also Merritt & Tremblay 1994 for a more sophisticated approach, yet to be applied to GC data). This method does not take into account the velocity information, which in any case is not available for all the stars.
5. Only the luminous stars are directly observed. However, most of the mass is expected to be in the very faint low mass stars, compact remnants or other forms of dark mass, if such exist (§4.2). In order to obtain the mass density $\rho(r)$, it is necessary either to measure the diffuse mass dynamically, which is very difficult to do in the center, where the potential is dominated by the MBH (§4.2.3), or else assume a stellar number-to-mass ratio, N_*/M , in order to translate the stellar number density $n_*(r)$ to mass density. Such a procedure is very uncertain, since N_*/M probably depends strongly on the distance from the MBH due to mass segregation.

The light distribution in the GC approximately follows a $\sim r^{-2}$ power-law from as far away as ~ 100 pc, where it cannot be directly related to the central super-massive BH, to ~ 1 pc from SgrA* (Serabyn & Morris 1996; §2). Early attempts to determine the stellar distribution inside the central

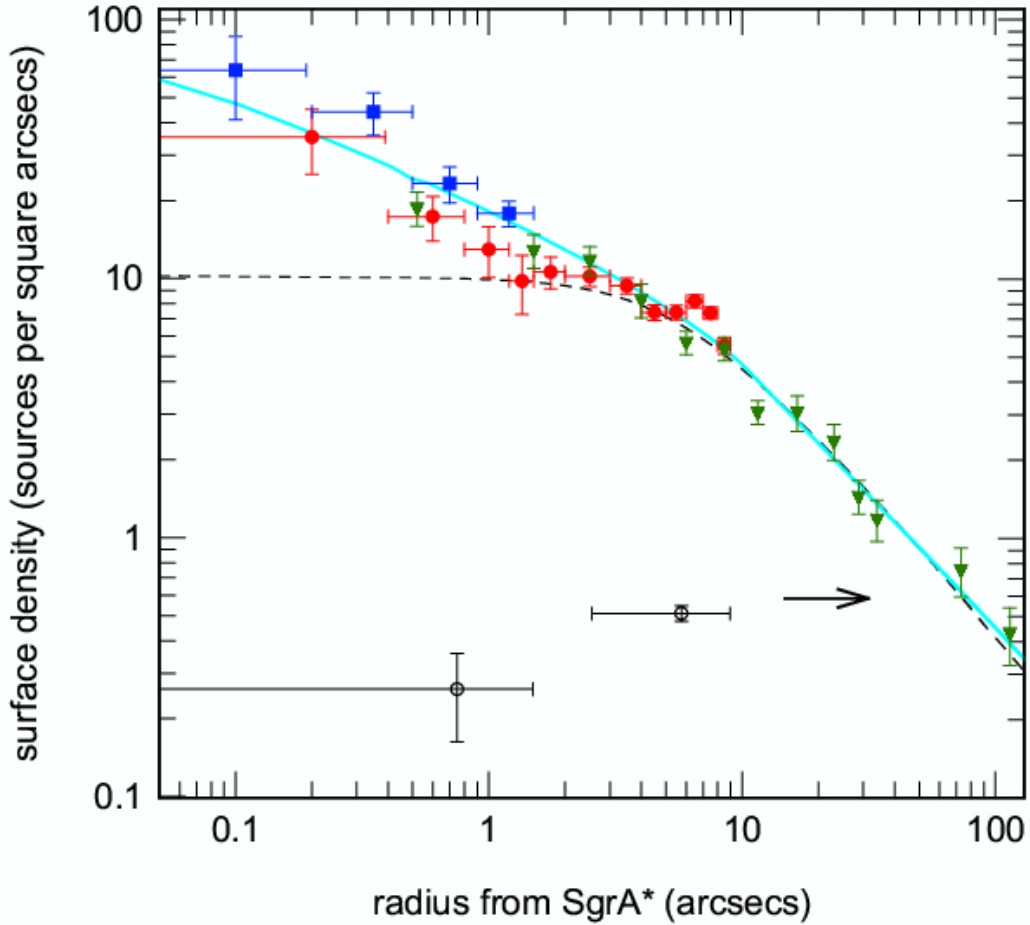


Figure 3.1: Measurements of the surface density distribution of the stellar counts around the Galactic MBH (Genzel et al 2003b). The observed surface density corresponds to a space number density of $n_{\star} \propto r^{-\alpha}$ with $\alpha = 1.0 \pm 0.1$ inside 0.4 pc, and $\alpha = 2.0 \pm 0.1$ outside. (Reprinted with permission from the *Astrophysical Journal*).

parsec concentrated on identifying the core radius r_c , where the surface density falls to half its central value, by measuring the surface density of the brightest stars (the only ones observable at the time) or of the total surface brightness. These studies yielded conflicting results, from $r_c \sim 0.05$ pc (Allen 1983; Scoville 2004) to ~ 1 pc (Rieke & Rieke 1988). It appears that the differences between the various estimates depend on whether the light distribution or the number counts are used and whether or not the bright stars are included in the fits. A consensus has yet to emerge on this question.

Generally, star counts follow the mass more faithfully than the total light distribution, which is completely dominated by the light of giants, even though they are only a small fraction of the population both by number and mass. Analyses of the stellar distribution based on star counts (Alexander 1999; Genzel et al 2003b) indicate that a stellar cusp rises monotonously all the way into the central $\sim 0.1''$ (0.004 pc) (Fig. 3.1). The number density was determined by fitting the star-counts to a 3-parameter broken power-law (break radius and the inner and outer exponents) using maximal likelihood and taking into account completeness corrections. The number density was then converted to a mass density by assuming a constant N_{\star}/M ratio and normalizing to the enclosed stellar mass $M_{\star}(<r) = M(<r) - m$ far from the MBH. The total enclosed mass $M(<r)$ was measured dynamically on the $\lesssim 10$ pc scale, and

the MBH mass m was measured dynamically close to the center (§4.1). The resulting mass model is (Genzel et al 2003b; assuming $R_0 = 8$ kpc)

$$\rho(r) = \rho_0 \left(\frac{r}{r_0} \right)^{-\alpha}, \quad \rho_0 = 1.2 \times 10^6 M_\odot \text{pc}^{-3}, \quad r_0 = 0.4 \text{pc}, \quad \alpha = \begin{cases} 1.4 \pm 0.1 & r < r_0 \\ 2.0 \pm 0.1 & r \geq r_0 \end{cases}. \quad (3.24)$$

This translates to an enclosed stellar mass in the inner cusp ($r < r_0$) of

$$M_\star(< r) = 6 \times 10^5 (r/r_0)^{1.6} M_\odot, \quad (3.25)$$

and extremely high densities near the MBH, $\rho(0.04 \text{pc}) = 3 \times 10^7 M_\odot \text{pc}^{-3}$ and $\rho(0.004 \text{pc}) = 8 \times 10^8 M_\odot \text{pc}^{-3}$. Note however that the total mass enclosed in the high density regions is very small, only $\sim 8000 M_\odot$ inside 0.04pc and $\sim 200 M_\odot$ inside 0.004pc . These estimates of extreme densities are consistent with the observed gradual depletion of bright giants with decreasing distance to the center, which is naturally explained by a combination of projection effects and collisional destruction in a steep density cusp (§3.4).

The observed power-law is consistent with the Bahcall-Wolf solution for the less massive stars in a relaxed population. This may hint that the mass density inside r_0 is dominated by dark objects more massive than the $M_\star < 10 M_\odot$ stars which constitute the majority of the observed population. If this is indeed the case, as is further explored in §3.3, then N_\star/M must rise toward the center, contrary to what was assumed, and so the mass model (Eq. 3.24) should be interpreted as representing the run of the density in the luminous stars only. The total mass density distribution may have a steeper slope than the observed number density, and the mass density close to the center may be yet higher than the estimates above⁸.

3.3 Mass segregation

It is quite likely that the stars observed near the MBH constitute only a small fraction of the total extended mass there. Mass segregation is expected to drive a flow of NSs and SBHs to the center since these compact remnants are more massive than the mean stellar mass in the unsegregated parent population (table 2.1) and since, unlike the short-lived massive MS stars, the remnants are effectively eternal and have time to segregate significantly (Morris 1993; Miralda-Escudé 2000). SBHs, which are the most massive stellar remnants, are expected to be the most centrally concentrated.

The farther from the center a compact object is born, the longer it takes it to sink in. The process can be described in terms of dynamical friction, the drag experienced by a massive object M_\bullet as it moves through a background of lighter masses (the drag is due to the work done by the massive object in focusing the lighter masses across and behind it). When the velocity DF is Maxwellian, and in the limit $M_\bullet \gg \langle M_\star \rangle$, the deceleration due to dynamical friction, \dot{v}_{df} , depends only on the total mass density of the background stellar population and not on the individual masses (Chandrasekhar 1943; Binney & Tremaine 1987, Eqs. 7–17, 7–23),

$$\dot{v}_{\text{df}} = - \frac{4\pi \log \Lambda G^2 M_\bullet \rho(r)}{v^2} \left[\text{erf}(X) - \frac{2X}{\sqrt{\pi}} \exp(-X^2) \right], \quad (3.26)$$

where $X \equiv v/\sqrt{2}\sigma$ (Note that the dynamical friction timescale for $v \sim \sigma$, $t_{\text{df}} \equiv |v/\dot{v}_{\text{df}}| \sim t_r \langle M_\star \rangle / M_\bullet$, is the mass segregation timescale, Eq. 3.9). To estimate the size of the “collection basin” from which compact objects can reach the center over the lifetime of the Galaxy $t_H \sim 10$ Gyr, consider the orbital evolution of

⁸For a given, dynamically determined enclosed mass M_0 within r_0 , a power-law density $\rho(r) = [4\pi M_0 / (3-\alpha)r_0^3] (r/r_0)^{-\alpha}$ increases with increasing α inside $r_\alpha = r_0 \exp[1/(\alpha-3)]$ and decreases outside r_α .

a compact remnant of mass M_\bullet that is initially on a circular orbit with velocity v_c at some radius r from the center. The dynamical friction drag exerts a torque $\dot{L} = \dot{v}_{\text{df}} r$ that causes the orbit to decay and the mass to spiral inward. It is convenient to approximate here the central density distribution as an isothermal cusp, $\rho(r) = v_c^2 / 4\pi G r^2$, whose circular velocity $v_c = \sqrt{2}\sigma$ is independent of the radius, so that $\dot{L} = v_c \dot{r} = \dot{v}_{\text{df}} r$. This assumption does not introduce a large error since the stellar density distribution outside the central regions is approximately isothermal (§3.2), and most of the time spent by the inspiraling object is at large radii. The solution of the torque equation relates the time available for reaching the center, t_{df} , to the maximal initial distance $\max r_{\text{df}}$,

$$\max r_{\text{df}} = \left(\frac{\log \Lambda}{1.17} \frac{GM_\bullet t_{\text{df}}}{v_c} \right)^{1/2} \sim 5 \text{ pc}, \quad (3.27)$$

for $t_{\text{df}} = t_H$, an SBH of mass $M_\bullet = 10 M_\odot$, and for $\log \Lambda \sim 10$ and $v_c \sim 150 \text{ km s}^{-1}$ on the $\lesssim 10 \text{ pc}$ scale (Kent 1992). This is in very good agreement with estimates based on more realistic density profiles for the GC (Morris 1993; Miralda-Escudé 2000).

It is difficult to estimate reliably the number of SBHs, N_\bullet , that have sunk to the center in the course of the Galaxy’s lifetime, or the characteristic spatial extent r_\bullet of the central SBH cluster. Such an estimate depends on various uncertain quantities and properties: the IMF, the star formation history of the GC, the relation between the initial stellar mass and the final SBH mass (the SBH mass function) and the dynamical conditions in the GC. In addition, the magnitude of the SBH natal “kick” velocity could affect the segregation efficiency, since faster SBHs sink more slowly (Eq. 3.27). Estimates lie in the range $N_\bullet = 2.4 \times 10^4$ within $r_\bullet = 0.7 \text{ pc}$ (for $M_\bullet = 7 M_\odot$ SBHs; Miralda-Escudé & Gould 2000) to between $N_\bullet = 3.2 \times 10^4$ and $N_\bullet = 7.4 \times 10^5$ within $r_\bullet = 0.8 \text{ pc}$ (for $M_\bullet = 10 M_\odot$ SBHs; Morris 1993). However, values of $N_\bullet \gtrsim 10^5$ are inconsistent with the current dynamical measurements of the enclosed stellar mass on these scales (§3.2). Inside r_\bullet the SBHs are expected to be distributed in a $r^{-7/4}$ cusp (§3.1.3).

Irrespective of the uncertainty in N_\bullet , this is an extreme degree of concentration. The inner parsec of the Galaxy may contain up to $\sim 10^{-2}$ of all Galactic SBHs, in $\sim 10^{-10}$ of the Galactic volume. Such a degree of mass segregation will significantly affect the run of the N_\star/M ratio with radius, which may fall by an order of magnitude from $r \sim 10 \text{ pc}$ to $r \sim 0.01 \text{ pc}$ (M. Freitag, private. comm.).

It is possible to obtain a rough upper limit on the central concentration of SBHs from purely dynamical considerations. The more concentrated the SBH cluster, the higher the rate at which two-body scattering will deflect SBHs into event horizon-crossing orbits. The “drain limit” is set by considering how many SBHs can be packed inside a radius r_\bullet , in steady state, so that the number scattered into the MBH over the age of the Galaxy equals the number enclosed (Alexander & Livio 2004; §6.1.1)

$$\frac{1}{N_\bullet} \frac{dN_\bullet}{dt} \sim \frac{1}{\log(2\sqrt{r_\bullet/r_S}) t_r} < \frac{1}{t_H}. \quad (3.28)$$

Equation (3.28) translates to the upper bound (solved numerically),

$$\max N_\bullet(< r_\bullet) \sim \frac{2 \log(2\sqrt{r_\bullet/r_S})}{3 \log(0.4 \max N_\bullet)} \left(\frac{m}{M_\bullet} \right)^2 \frac{P(r_\bullet)}{t_H}. \quad (3.29)$$

This limit is particularly useful close to the MBH, where the enclosed stellar mass estimates become unreliable due to the uncertainties in the determination of the MBH mass and of N_\star/M . The drain limit for $10 M_\odot$ SBHs is $\sim 10^4$ inside $r_\bullet = 0.1 \text{ pc}$.

The central cluster of massive compact remnants is not easy to detect. Three possible approaches are discussed in the literature: (1) direct detection of the compact objects; (2) detection of mass segregation by the central depletion of light “test particles”; (3) indirect detection of the compact objects by their effects on the environment. The evidence for mass segregation around the Galactic MBH is at present only circumstantial.

Direct dynamical detection of the smoothed potential of the extended mass by deviations from Keplerian motion requires very high astrometric precision over multiple orbital periods. The current upper limit is still ~ 30 higher than predicted by the drain limit (Mouawad et al 2005; §4.2.3). Orbital perturbations by occasional close interactions with individual compact remnants may be detectable with future very large telescopes ($\gg 10$ m) (Weinberg, Milosavljević & Ghez 2005). The gravitational lensing properties of the MBH with respect to background stars will be modified by the SBHs orbiting it, in particular when the light rays of a lensed image pass near one of the SBHs (Gould & Loeb 1992; Miralda-Escudé & Gould 2000; §5.2). However, the detection of background stars lensed by an MBH–SBH “binary” requires a photometric sensitivity ~ 100 times larger ($K \sim 23$ mag) than is presently available and even then the events are predicted to be rare ($\sim 0.06 \text{ yr}^{-1}$) (Chanamé, Gould & Miralda-Escudé 2001). Accretion of the dilute interstellar gas by fast moving compact remnants in the inner ~ 0.1 pc will probably not lead to significant X-ray emission (Haller et al 1996; Pessah & Melia 2003). On the larger, 1 pc scale there is an observed over-abundance of transient X-ray sources (4 sources observed compared to 0.2 expected on average). This is interpreted as evidence for a high central concentration of NS and SBHs, of which some are accreting from a binary companion acquired in the course of a 3-body exchange encounter with a stellar binary (Muno et al 2005).

Chanamé & Gould (2002) propose using the angular distribution of millisecond pulsars around the MBH for detecting mass segregation. Millisecond pulsars, being NSs, are lighter than the average stellar mass in the SBH-dominated center. Since they are older than the relaxation time (their ages are estimated from the spin-down timescale, $P/2\dot{P} \sim \text{few} \times 10^9 \text{ yr}$), they should be depleted in the center due to mass segregation. However, the radio pulses are hard to detect because they are strongly scattered by the interstellar plasma in the GC. Lazio et al (2003) report finding only 10 candidate pulsars in the central ~ 200 pc of the GC. Deeper surveys at higher frequencies will be required to avoid the scattering and to significantly improve these statistics. Another class of potential light test particles are the long-lived, low mass MS progenitors ($M_\star \lesssim 2 M_\odot$) of the He burning “horizontal branch / red clump” giants (Alexander et al., in preparation). While the low mass progenitors are themselves too faint to be observed by current instruments, their giant progeny are luminous enough ($K \sim 16$) and are readily detected. Observations show that these giants gradually disappear from the population with decreasing projected distance from the MBH (Genzel et al 2003b). One possible interpretation is that this is due to mass segregation operating on the progenitors. However detailed calculations are still lacking, and other explanations, such as collisional destruction (§3.4), have yet to be ruled out.

Finally, the compact remnants could be revealed by their effect on the relatively few burning stars in the center. Collisional destruction by SBHs, perhaps accompanied by the creation of exotic collision products (e.g. Thorne–Żytkow objects) is a possibility that has not yet been explored in detail. Strong, non-destructive interactions between SBHs and MS stars of similar mass may be responsible for the capture of the young B-stars observed there (Alexander & Livio 2004; §7.2.4).

3.4 Stellar Collisions

With central densities above $10^8 M_\odot \text{ pc}^{-3}$, the inner cusp is the densest environment in the Galaxy, exceeding even the core density of massive globular clusters by up to a factor of 100. In this extreme density the mean time between physical stellar collisions, t_{coll} (Eq. 3.11) is shorter than the age of system $\sim t_H$, which is also roughly the lifespan of a $\sim 1 M_\odot$ star. Since the probability to avoid a collision is $\exp(-t_H/t_{\text{coll}}) \ll 1$, the dynamics and stellar population in the high density inner cusp are completely dominated by collisions. The GC is essentially a naturally occurring “stellar collider”.

3.4.1 Collisional destruction of giants

Images of the inner arcseconds of the GC clearly reveal a central cavity in the distribution of luminous late-type red giants (Fig. 2.2). The depletion is gradual (Fig. 3.2). Inside $\sim 5''$ (0.2 pc projected distance) there are no $K < 10$ mag late-type giants, and inside $\sim 1.5''$ (0.06 pc projected distance) there are even no $K < 12$ mag late-type giants. Apart for the luminous, short-lived He stars (§2.2), the maximal stellar luminosity gradually decreases in the inner $2''$.

A possible explanation for this trend, selective obscuration of the center by a centrally concentrated distribution of dust, is not supported by an analysis of the measured extinction across the inner parsec (Alexander 1999). Alternatively, stellar collisions could be responsible for the depletion of the luminous late-type giants (Lacy, Townes & Hollenbach 1982; Phinney 1989; Genzel et al. 1996) or the disappearance of CO absorption—a distinctive spectral signature of red giants—in the integrated light (Sellgren 1990; Figer et al 2000). Luminous red giants have very large extended envelopes, and therefore a large cross-section for collisions with other stars. A strong collision may strip the giant’s envelope leaving behind an almost bare burning core. This will drastically lower its IR luminosity because the IR spectral range lies in the Raleigh-Jeans part of the stellar blackbody spectrum (for effective temperature $T_\star \gtrsim 4000$ K), and so the IR luminosity scales as $L_{\text{IR}} \propto R_\star^2 T_\star$ whereas the total stellar luminosity scales as $L_\star \propto R_\star^2 T_\star^4$. Consider a collision that disperses the envelope of a $\sim 100 R_\odot$ red supergiant and leaves a $\sim 1 R_\odot$ burning core. Studies of rapid mass transfer in close binaries (e.g. Podsiadlowski, Rappaport & Pfahl 2002) indicate that a stripped core retains its nuclear luminosity. The factor 10^4 decrease in surface area must then be compensated by a factor 10 increase in the effective temperature, which translate to a factor 10^3 (7.5 mag) decrease in the IR luminosity.

Despite its low surface gravity, a red giant is quite robust against collisions. The dynamical timescale in the envelope is of the order of a year and the thermal timescale is of the order of several decades, so a collision in which a star “punches a hole” in the giant’s envelope will probably not have a lasting effect. However, hydrodynamical studies of collisions between dwarf stars and giants indicate that the envelope can be completely disrupted when the impact parameter is significantly smaller than the stellar radius. This happens either by the ejection the giant’s core from the extended envelope, which then rapidly disperses, or by the formation of a common envelope binary, which stirs the envelope and leads to its evaporation on a time scale much shorter than the giant phase (Livne & Tuchman 1988; Davies & Benz 1991; Rasio & Shapiro 1990, 1991; Bailey & Davies 1999). 3-body collisions between a binary and a giant are even more efficient in disrupting the envelope (Davies et al. 1998). However, it is hard to estimate the overall contribution of 3-body collisions because the binary fraction near the MBH is uncertain. Note that collisional destruction is less likely to occur in early-type blue supergiants, which do not have a well-separated compact core / extended envelope structure.

Figure (3.2) compares the observed distribution of stars in the plane of projected distance p and magnitude K with theoretical contours of the expected mean number of surviving giants in a collisionally dominated cusp. The stellar spectral type is indicated, where such information is available. The early-type stars, which are too young to be dynamically relaxed, clearly stand out in the p - K plane. They are too short-lived to be affected by stellar collisions. In contrast, the old late-type giants are relaxed and susceptible to collisions. The theoretical calculations estimate the collisions rate (Eq. 3.11) and survival probability by assuming solar mass projectiles, use cross-sections for collisional destruction calibrated by hydrodynamical simulations, and take into account the stellar DF (Eqs. 3.24, 3.22) and mass function (Eq. 2.1) of the GC and the evolution of the stellar radius and K -band luminosity along the stellar tracks (Alexander 1999). The possible effects of mass segregation in enhancing the collision rate and efficiency are not taken into account.

The results show that two distinct effects can cause the observed depletion. One is purely geometrical. The number of stars enclosed in an annulus of projected radius p and width dp scales as $p^{2-\alpha} dp$ in a $n_\star \propto r^{-\alpha}$ cusp. For cusps shallower than r^{-2} the number of stars decreases with p , and so does the

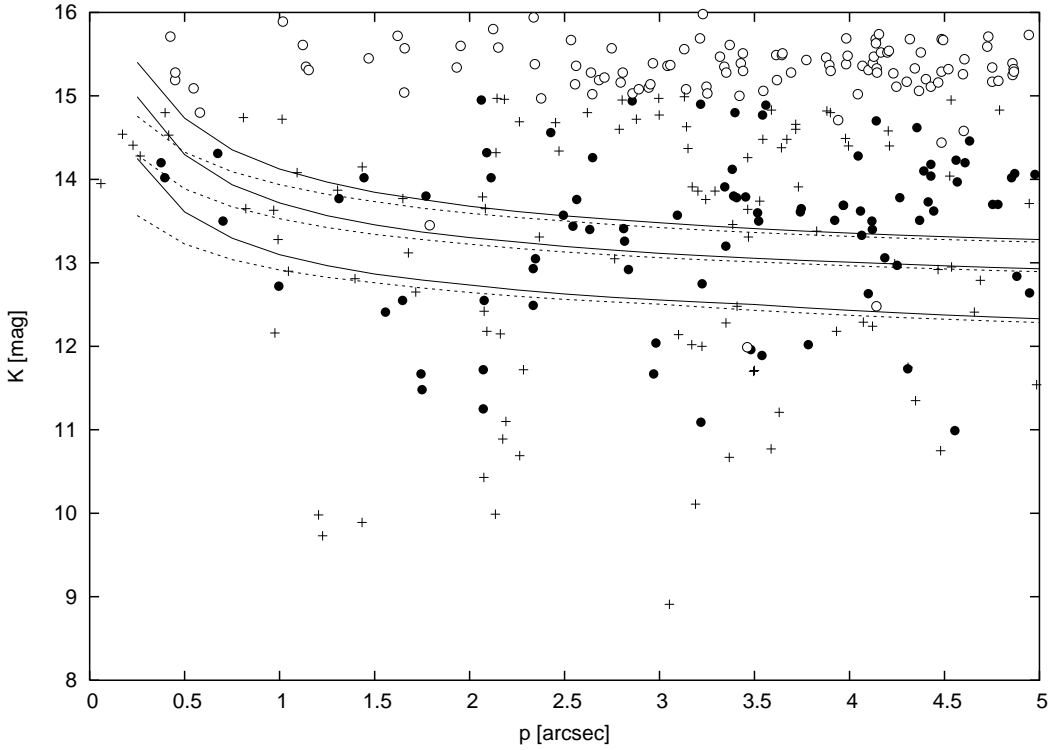


Figure 3.2: Evidence for the collisional destruction of the envelopes of bright red giants in a high density stellar cusp around the Galactic MBH (updated version of figure 9 in Alexander 1999). The apparent stellar K -band magnitude of stars in the inner $5''$ is plotted against the projected angular distance from the black hole, p (VLT CONICA/NAOS data from Trippe, Ott et al. 2005, in prep.). The stars are sorted into spectral types (filled circles: late-type, crosses: early-type, open circles: unknown) according to their spectral features (when available) or according to their CO-band color $m(\text{CO}) \equiv m(2.29\mu\text{m}) - m(2.26\mu\text{m})$ (from the Gemini science demonstration dataset), which is sensitive to the characteristic CO absorption feature in late-type giants (Genzel et al. 2003b). Most of the low luminosity stars without spectral identifications are probably also old late-type stars. The three dashed contour lines represent model predictions for the decrease in surface density of bright stars due to projection. The three solid lines include also the effects of collisional destruction in a high density $n_* = 1.2 \times 10^6 (p/10'')^{-1.4}$ stellar cusp (§3.2). The model predicts, on average, 1.5 (top contour), 1.0 (central contour), and 0.5 (bottom contour) dynamically relaxed (old) stars per 0.25 arcsecond bin that are brighter than the contour level.

probability of observing the rarer, luminous giants. The second effect is dynamical. Once the stellar density rises above $\sim 5 \times 10^7 M_\odot \text{pc}^{-3}$, collisions become effective. The additional collisional depletion, above that due to projection, improves the fit of the model to the data in the inner $\sim 1.5''$. Thus, the observed gradual depletion of bright late-type giants toward the center cannot, in itself, be taken as proof of a high density cusp. However, taken together with the observed rise in the surface density (§3.2), both properties indicate that a steep, high density cusp provides a self-consistent interpretation of the data.

3.4.2 Tidal spin-up

The Keplerian velocity in the inner parsec around the MBH is a substantial fraction of the escape velocity from a typical star, and even exceeds it at $r < r_{\text{coll}}$ (§3.1.2). Stars moving rapidly in the dense stellar cusp near the MBH will suffer over their lifetimes numerous high-velocity, close tidal encounters with other stars. Although such encounters transfer some energy and angular momentum from the hyperbolic orbit ($\varepsilon < 0$ relative to the other star) to the colliding stars, they rarely remove enough energy for tidal capture. This is in marked contrast to the situation in the high density cores of globular clusters, where the colliding stars are on nearly zero-energy orbits and close collisions can lead to the formation of tight binaries. The effects of hyperbolic encounters on the stars are mostly transient. The dynamical and thermal relaxation timescales are short compared to the stellar lifespan, and thus apart from some mass-loss in very close collisions, the star is largely unaffected. It is however more difficult for the star to shed the excess angular momentum since magnetic braking (the torque applied to a star when the stellar wind resists being swept by the rotating stellar magnetic field) typically operates on timescales of the order of the stellar lifespan (Gray 1992). Fast rotation is therefore the longest lasting dynamical after-effect of a close encounter. Over time, the contributions from many, randomly oriented tidal encounters will lead to a “random walk” buildup of the stellar spin (Alexander & Kumar 2001).

The possibility that stars in MBH cusps are rapid rotators may have interesting implications for their evolution and the interpretation of their observed properties (see review by Maeder & Meynet 2000). For example, rotationally induced mixing may reveal itself in the spectral line ratios, and rotation may be directly observed in the spectral line profiles (but high rotation will be suppressed by expansion in the giant phase). Detection of such signatures in the spectra of the observed giants can provide additional evidence for the existence of an underlying dense cusp of low-mass MS stars, which at present cannot be directly observed.

Consider a star of mass M_* and radius R_* that undergoes a single tidal encounter with a perturbing mass m (here a star or a compact object). When the tidal deformations in the star are small, the energy taken from the orbit and invested in raising the tides can be described by a linear multipole expansion in the periape distance (distance of closest approach) $r_p = a(1 - e)$ (Press & Teukolsky 1977),

$$\frac{\Delta E_t}{E_*} = \left(\frac{m}{M_*} \right)^2 \sum_{l=2}^{\infty} \frac{T_l(\eta, e)}{(r_p/R_*)^{2l+2}} \sim \frac{T_2}{(r_p/r_t)^6}, \quad (3.30)$$

where $E_* \equiv GM_*^2/R_*$ is the stellar binding energy (up to a factor of order unity depending on the stellar structure), T_l are the dimensionless tidal coupling coefficients, which depend on the eccentricity e ($e > 1$ for an unbound orbit, Eq. 3.15) and on the dimensionless periape crossing timescale $\eta \equiv \tau_p/\tau_*$ where $\tau_p = \sqrt{r_p^3/G(M_* + m)}$ is the periape crossing timescale and $\tau_* = \sqrt{R_*^3/GM_*}$ is the stellar dynamical timescale. The tidal coefficients T_l can be calculated numerically for any given stellar model and orbit (e.g. Alexander & Kumar 2001). For many applications it suffices to use the lowest order multipole, T_2 . The angular velocity at periape is

$$\Omega_p^2 = \frac{v_\infty^2}{r_p^2} + \frac{2G(M_* + m)}{r_p^3}, \quad (3.31)$$

where v_∞ is the relative velocity at infinity. Generally, T_2 peaks when Ω_p matches the frequency of the fundamental mode of the star, $\Omega_p \sim \mathcal{O}(\tau_*^{-1})$. The higher the velocity of the encounter (the larger e , Eq. 3.15), the larger the value of r_p (larger η) for resonance with the fundamental mode. The distance dependence of ΔE_t (to lowest order) can be understood by noting that the energy in the tidal oscillations is proportional to the square of the amplitude of the tidal elongation, $\Delta R_*/R_* \sim (R_*/r_p)^3 (m/M_*)$.

The orbital energy, ΔE_t , and angular momentum, ΔJ_t , that are transferred to the star in an impulsive tidal encounter (such as a hyperbolic one) are related by (e.g. Kumar & Quataert 1998)

$$\Delta E_t = \Delta J_t \Omega_p. \quad (3.32)$$

For rigid body rotation⁹, the change in the angular velocity of the star due to the tidal interaction is $\Delta \Omega_t = \Delta J_t / I$, where I is the star's moment of inertia (assumed here constant), so that

$$\frac{\Delta \Omega_t}{\Omega_b} = \frac{\sqrt{GM_\star^3 R_\star}}{I \Omega_p} \left(\frac{m}{M_\star} \right)^2 \sum_{l=2}^{\infty} \frac{T_l(\eta, e)}{(r_p/R_\star)^{2l+2}}, \quad (3.33)$$

where $\Omega_b \equiv \sqrt{GM_\star/R_\star^3}$ is the centrifugal breakup angular velocity, where the star sheds mass from its equator.

Equations (3.30) and (3.33) apply only for soft encounters ($r_p \gtrsim 2R_\star$), where the linear expansion holds. Hydrodynamic simulation can then be used to extend Eq. (3.33) to strong encounters. Simulations show that as r_p decreases, $\Delta \Omega_t$ first grows faster than predicted by linear theory, but then as r_p approaches R_\star , the formal divergence of $\Delta \Omega_t$ is truncated when mass is ejected from the tidally disturbed star and carries away the excess angular momentum (Alexander & Kumar 2001). Figure (3.3) shows the predicted mean rotation of solar mass stars in the GC cusp after 10 Gyr of stochastic tidal spin-up, assuming inefficient magnetic breaking. The stellar spin reaches an r.m.s value of $\Omega/\Omega_b \sim 0.3$ at the center (rotational velocity of $0.3V_\star \sim 130 \text{ km s}^{-1}$), about 60 times higher than is observed in solar type stars in normal environments. The spin-up effect falls only slowly with distance from the MBH ($\Omega/\Omega_b \sim 0.1$ at 0.3 pc) because the higher tidal coupling in slower collisions compensates for the lower collision rate there. Thus atypically high spin could be a characteristic of long-lived, low mass stars over a substantial fraction of the MBH's sphere of influence. The spin-up, being a random walk process, grows with time as $t^{1/2}$ and become significant only for long-lived stars. It is not relevant for short-lived massive MS stars or for the relatively short post-MS giant phase. For example, a $5M_\odot$ star with $V_\star \sim 600 \text{ km s}^{-1}$ and a MS lifespan of $t_\star \sim 10^8 \text{ yr}$ will be spun up close to the MBH to only $0.3V_\star \sqrt{t_\star/t_H} \sim 20 \text{ km s}^{-1}$ (scaling from the calculated spin-up for a $1M_\odot$ star and assuming a similar spin-up efficiency). This is much less than the typical rotational velocity observed in such stars in normal environments, whose origin is related to their formation and not to tidal spin-up.

3.4.3 Stellar mergers and exotic objects

A possible outcome of a collision between two stars is a merger, where a new object, possibly more massive than either of its building blocks, is created. The high rate of stellar collisions near the MBH raises the question whether it is possible to create massive stars from lower mass stars by successive mergers, or exotic stars by the capture of a compact object inside a normal star (Morris 1993). This is of interest in view of the puzzling presence of young massive stars near the MBH, where normal modes of star formation are thought to be impossible (§7). The hypothesis that the very massive emission line stars in the central 0.4 pc are merger products is made less compelling by the fact that such stars are also found in the young massive stellar clusters in the central $\sim 50 \text{ pc}$, where the central densities are much smaller (§2.1). In addition, the collision rate is much too low at the relatively large distance of

⁹The timescale for angular momentum re-distribution due to convective transport in a red giant is $\sim 1 \text{ yr}$ (Zahn 1989) and so rigid rotation is achieved on a timescale similar to that of the collision itself. The timescale for angular momentum re-distribution in radiative MS stars is not well known, although it is likely to be shorter than the stellar lifespan.

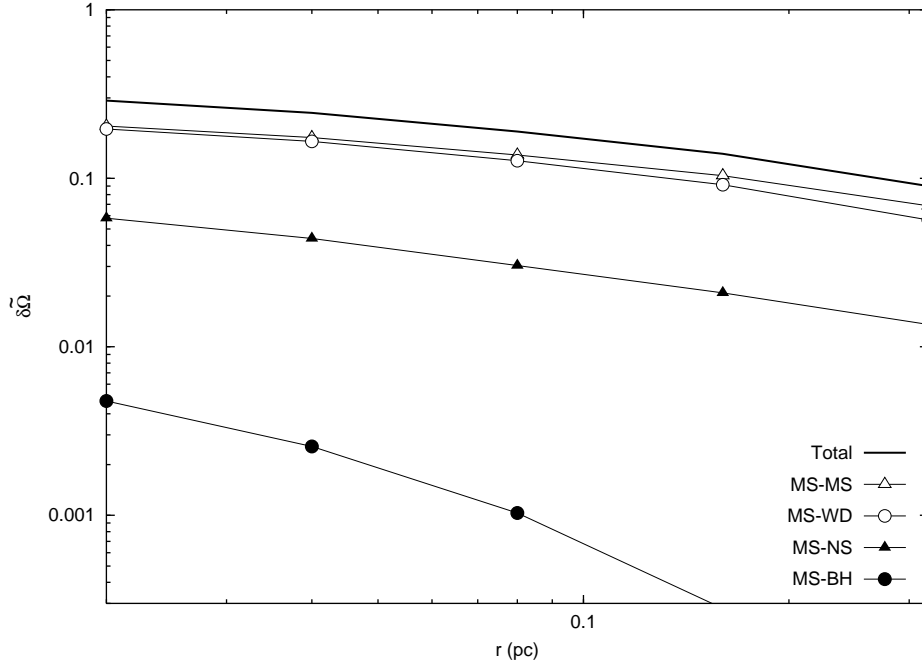


Figure 3.3: The average spin-up of a solar type star by star-star tidal interactions over 10 Gyr as function of distance from the Galactic MBH (Alexander & Kumar 2001). An $\alpha=1.5$ density cusp is assumed. The rotation grows over time in a random walk fashion by repeated close passages. The angular rotation frequency $\delta\bar{\Omega} \equiv \delta\Omega/\Omega_b = 1$ corresponds to rotation at the centrifugal break-up velocity. In addition to the total spin-up, the separate contributions from collisions with main sequence stars (MS), white dwarfs (WD), neutron stars (NS) and stellar black holes (BH) are shown. (Reprinted with permission from the *Astrophysical Journal*).

the emission line stars (Eq. 3.11). However, it is still relevant to consider the merger scenario for the S-stars, which are both much lighter and closer to the MBH.

A successful chain of mergers requires that the mean time between mergers be shorter than the lifespan of the merger product (usually assumed to be similar to the MS lifespan of a normal star of the same mass, and therefore becoming shorter as the merger chain progresses). The time constraint does not appear to be an insurmountable obstacle, if glancing collisions can lead to a merger (Genzel et al. 2003b). However, it is very unlikely that the merging efficiency can be so high for such high velocity collisions.

The first requirement for an efficient merger is that the impactor star (the smaller of the two with mass M_i) can be stopped in the target star (the larger of the two with mass M_t). This translates to the requirement that the target mass contained in the cylinder “punched out” by the impactor equals or exceeds the impactor mass, that is approximately $M_i \lesssim R_i^2 R_t (M_t/R_t^3)$, where R_i and R_t are the radii of the impactor and target. Thus, the stopping condition can be formulated as the requirement that the column density of the impactor be less or equal to that of the target,

$$\frac{M_i}{R_i^2} \lesssim \frac{M_t}{R_t^2}. \quad (3.34)$$

Effective stopping does not in itself imply an efficient merger, since when $v_\infty > V_e$, the specific kinetic energy of the impactor is enough to unbind a unit mass of the target star. The total amount of mass that can be ejected from the target depends then also on the mass ratio between the impactor and

the target. The relative velocity at impact is $\geq V_e$ even when $v_\infty = 0$, which is of the order of the sound speed in the star. Therefore such collisions will be supersonic, and the kinetic energy can be efficiently converted to heat by the shocks and drive the mass loss. The outcome of a penetrating encounter depends therefore not only on the mass ratio and the relative velocity, but also on the assumed stellar M_\star -to- R_\star relation, and on the impact parameter (since the column density is a strongly varying function of position in the star).

The actual situation revealed by numerical simulations is more complex than implied by the simplified discussion above. For example, an impactor can be destroyed by heating even when it is not stopped by the target, and mergers can occur in slow enough collisions even without initial physical contact between the two stars if they are tidally captured and form a decaying binary. The simulations generally show that the merger efficiency decreases rapidly when $v_\infty \gtrsim V_e$, but the exact details depend strongly on the assumed stellar structure model. Lai et al. (1993) find that mergers can occur even when the relative velocity is as high as $v_\infty \sim 1.5V_e$, provided that the collision is very close to head-on. However, Freitag & Benz (2005), using more realistic stellar models, find that mergers are much less efficient. Freitag, Gürkan & Rasio (2004) find no mergers in Monte-Carlo simulations of stellar collisions in a galactic nucleus with a MBH. Thus, massive star buildup by mergers very near the MBH does not appear likely.

A related process is the capture of a compact object (NS or SBH) inside a star, and the possible formation of an exotic, accretion powered "star" (Thorne-Żytkow object). The typical relative velocity at impact between the compact object and the star is $v \sim \mathcal{O}(Gm/r)$, which is much smaller than the escape velocity from the compact object, $V_e \sim \mathcal{O}(c)$. The collisional cross-section of the compact object is then dominated by the gravitational focusing term (see Eq. 3.1.2), which is much larger than its physical size. Therefore, the effective size of the impactor is the Bondi accretion radius, $R_i \sim \mathcal{O}(GM_i/v^2)$ (Bondi 1952), and the column density ratio between the compact impactor and the target star is $\sim (R_i/r)^2 m^2 / (M_i M_t)$. This ratio can be of order unity if the collision is atypically slow or occurs at a large enough distance (e.g. $r \sim 0.1$ pc for $m = 3.5 \times 10^6 M_\odot$ and a collision between a $M_i = 1.4 M_\odot$ NS and a $M_t = 10 M_\odot$, $R_t = 4.5 R_\star$ star). A star powered by accretion on a NS may appear as a red giant or supergiant with peculiar photospheric abundances (Eich et al. 1989; Biehle 1991, 1994), whereas one accreting on a SBH may look like a WR blue giant (Morris 1993). The evolution of such configurations is uncertain.

4 Probing the dark mass with stellar dynamics

Stars near the MBH are effectively test particles since their mass is negligible compared to that of the MBH, $M_\star/m \sim 10^{-7} - 10^{-5}$. As long as their trajectories do not take them too close to the MBH, where dissipative processes can affect their motion (§6), stars directly probe the gravitational potential near the MBH. This is in contrast to gas dynamics, where the possible influence of non-gravitational forces due to thermal pressure, radiation pressure or magnetic fields can substantially complicate the interpretation of dynamical data and limit its usefulness. The analysis of stellar orbits near the MBH, well within the radius of influence, is further simplified by the fact that the orbits are Keplerian to a good approximation (Eq. 3.15).

The type of information about the dark mass that can be extracted from the data, the level of analysis possible, and the methods used, all depend on the nature of the observations (stellar position, proper motion, radial velocity, magnitude, colors, spectral classification), on their quality, on the properties of stars observed (proximity to the MBH, velocity, luminosity, age), and on the total duration of the monitoring. Two approaches can be used to weigh and locate the dark mass (§4.1). One is statistical, which typically requires less data for each star (and so was the first to be applied), but needs a meaningfully large sample and is limited by various necessary assumptions about the parent population. The second involves the derivation of partial or full orbital solutions for individual stars. In principle, a single well

sampled stellar orbit is all that is needed to obtain the mass and location of the dark mass (assuming the dark mass is fully enclosed in the orbit; §4.2). However, this is only feasible near the MBH, where the periods are short enough for accelerations to be measured. Farther away from the MBH ($r \gtrsim 0.1$ pc, $P \gtrsim 1000$ yr) there is no substitute for statistical mass estimators to measure the total enclosed mass (stars and MBH).

Following initial attempts to probe the potential of the central dark mass by gas kinematics (Wollman et al. 1976; Lacy et al. 1980), the use of stellar kinematics progressed to include radial velocities (McGinn et al. 1989; Sellgren et al. 1990; Krabbe et al. 1995; Haller et al. 1996; Genzel et al. 1997), stellar proper motions (Eckart & Genzel 1996; Ghez et al. 1998), and stellar accelerations (Ghez et al. 2000; Eckart et al. 2002). Each of these subsets of the full orbital data were used to place some constraints on the dark mass (§4.1.2). Finally, it is now possible, using high-precision infrared astrometry and spectroscopy, to follow the trajectories and radial velocity curves of individual stars as they orbit the MBH (e.g. Schödel et al. 2002; Ghez et al. 2003b; Eisenhauer et al. 2003,2005). The combined input from stellar orbits and from high precision radio measurements of the position and proper motion of Sgr A* have all but ruled out non-BH alternatives for the dark matter in the center of the GC (4.2). This has also made it possible to directly measure the distance to the GC (§4.1.3) and strongly constrain the presence of a secondary BH in the GC (§4.3). A very different class of stars that may provide information on the central dark mass are high-velocity stars, well on their way out of the Galaxy (§4.4). The discovery of such stars can prove that the dark mass must be extremely compact to eject them so energetically, and is therefore likely a MBH.

4.1 Weighing and pinpointing the dark mass

The primary parameters of the dark mass are its mass, size, location and velocity. An empirical determination of their values has many implications. The mass and size fix the mean density, which determines whether the dark mass is indeed a MBH (§4.2). The formal density associated with a BH (mass over volume of a Euclidean sphere whose radius is the event horizon) is

$$\rho_{\text{BH}} \sim \frac{3}{4\pi} \frac{m}{r_s^3} = \frac{3(c^2/2G)^3}{4\pi m^2} = \left(\frac{m}{4 \times 10^6 M_\odot} \right)^{-2} \times \begin{cases} 1.1 \times 10^3 \text{ g cm}^{-3} \\ 1.7 \times 10^{25} M_\odot \text{ pc}^{-3} \end{cases} \quad (4.1)$$

The higher the lower bound on ρ/ρ_{BH} , the more plausible is the assumption that it is a MBH, and the less likely are alternative non-singular configurations. The question of the position the dark mass can be decomposed into three separate issues. (1) Where is the dynamical center (the center of attraction) in the GC? (2) Where is the dynamical center relative to the center of mass of the GC? (3) Where is the dynamical center relative to the radio source Sgr A*? The three positions need not be the same.

The dark mass will execute Brownian-like motion relative to the stellar cluster around it due to small gravitational “kicks” arising from Poisson fluctuations in the stellar number density (e.g. Chandrasekhar 1944). The amplitude of the Brownian excursions away from the cluster’s center of mass will depend on how massive the dark mass is (the more massive it is, the less it will move) and on the properties of the stellar system around it (§4.2.3). It should be emphasized that due to the long range nature of gravitational interactions, Brownian motion in a self-gravitating system is fundamentally different from that in a gas. The statistical mechanics of the gravitational Brownian motion of a massive object, which itself dominates the potential, are still a subject of active investigations. Neither is it obvious that Sgr A* must lie at the dynamical center. This is of course expected if the source is an accreting MBH, since the emission should arise inside $\sim 10r_s \sim 10^{13}$ cm. However, the extremely low luminosity of Sgr A*, now also detected in the X-ray (Baganoff et al. 2001) and IR (Genzel et al. 2003a), does not require a MBH. It could easily be powered by accretion on a stellar mass compact object. In that extreme case, Sgr A* would merely be a test particle in orbit around the dark mass. To explore this possibility, it is

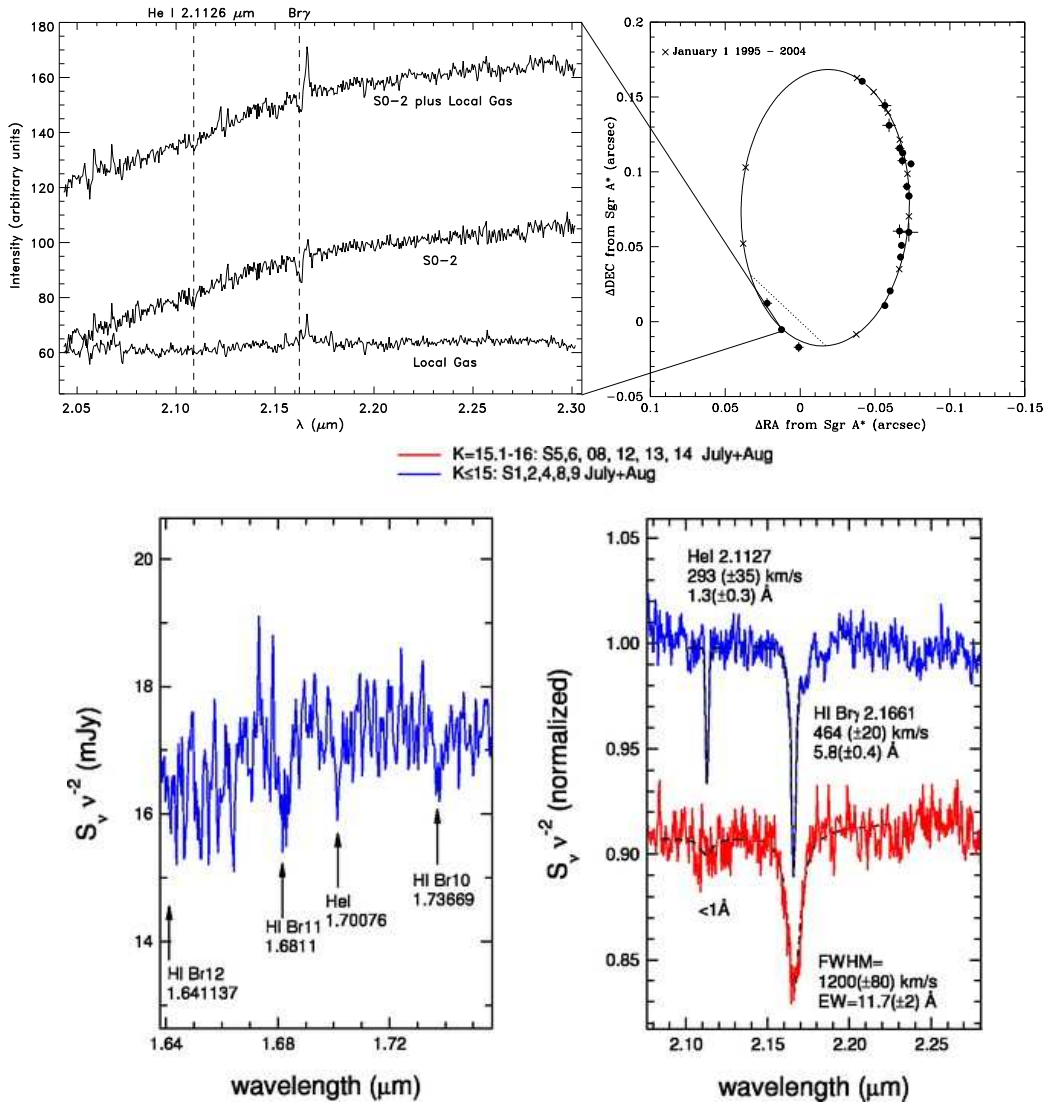


Figure 4.1: Infrared spectra of the early-type (hot) S-cluster stars. Top: Infrared spectrum and orbit reconstruction of S2/S0-2 (Ghez et al. 2003b). Reprinted with permission from the *Astrophysical Journal*. Bottom: Composite spectra of 5 bright stars ($K < 15$ mag, top spectra left and right) in the H and K -bands and 6 faint stars ($15 < K < 16$ mag, bottom spectrum left) in the K -band (Eisenhauer et al. 2005). Reprinted with permission from the *Astrophysical Journal*.

necessary first to pinpoint the location of the radio source Sgr A* in the IR frame, where the stars are observed and where the dynamical center is identified¹⁰. This was achieved by the discovery of 7 red giants and supergiants in the inner 15'' whose extended mass-loss envelopes ($R \sim 5R_*$) emit radio maser radiation (coherent light emission analogous to laser light) from a molecular transition of SiO (Menten et al. 1997; Reid et al. 2003b). Since these giants are also bright IR sources, they can be observed in both radio and IR and used to align the two reference frames and correct for various distortions. This enabled the determination of the position of Sgr A* relative to the IR stellar observations to within 10

¹⁰The IR reference frame is defined by the average angular position $\langle \mathbf{p} \rangle = \sum_{i=1}^{N_*} \mathbf{p}_i / N_*$ of a statistically large sample of stars around Sgr A*. While each star is moving, $\langle \mathbf{p} \rangle$ is assumed to be nearly stationary and the relative motion between $\langle \mathbf{p} \rangle$ and the central dark mass is assumed to be negligibly small (Eisenhauer et al. 2003).

mas (1σ) and established that Sgr A* indeed coincides with the dynamical center as determined by the orbits (§4.1.2). The radio/IR alignment also played a crucial role in the detection of the low level IR accretion emission from Sgr A* (Genzel et al. 2003a; Ghez et al. 2004).

Finally, a precise measurement of the position of the MBH along the line of sight, the distance to the GC, is important for reconstructing the structure and dynamics of the Galaxy (§4.1.3).

4.1.1 Statistical estimators

Astrometric observations of stars can provide the 2D projected angular positions $\mathbf{p}(t_i)$ at discrete times $\{t_i\}$, which by differencing yield the angular velocity (proper motion) $\dot{\mathbf{p}}(t)$ and angular acceleration (proper acceleration) $\ddot{\mathbf{p}}(t)$. Spectroscopic observations can measure the Doppler shift of spectral features and provide the line of sight velocity $\dot{z}(t_i)$, and the line of sight acceleration $\ddot{z}(t)$. The position z along the line of sight can not be measured directly. In practice, not all this information is available for all the stars. Spectroscopy requires more photons than photometry, and so faint stars may have proper motion information, but not radial velocities. In addition, a reliable measurement of the Doppler shift requires distinct spectral features, which are not always available in the IR range of the spectrum. Proper motion can be measured only when the astrometric errors are smaller than the proper displacement, and so slow stars far from the center may have radial velocity information, but not proper motion. The astrometry of stars near the dense center can be unreliable because of source confusion and because they can be “lost” among the other stars due to their high velocity and large displacement between consecutive observation times.

The available stellar data can be described statistically in terms of the mean surface number density $\Sigma(\mathbf{p})$ and the projected velocity dispersion of the i 'th velocity component $\sigma_p^2(\mathbf{p}) = \langle [v_i(\mathbf{p}) - \bar{v}_i(\mathbf{p})]^2 \rangle$ (assuming a value of R_0 for converting proper motion to physical velocity). The means are taken over binned projected areas. It is usually assumed, as is indicated by the observed Σ , that the density distribution is spherically symmetric. In that case the bins are annuli of projected radius p and width Δp .

The Jeans equation is the most direct way of using the mean quantities to estimate the enclosed mass (e.g. Binney & Tremaine 1987 §4.2.1d). It is assumed here for simplicity that the velocity dispersion is isotropic (see analysis of the non-isotropic case by Genzel et al. 2000). The projected quantities can be inverted by the Abel integrals,

$$n(r) = -\frac{1}{\pi R_0^2} \int_r^\infty \frac{d\Sigma}{dp} \frac{dp}{\sqrt{(R_0 p)^2 - r^2}}; \quad n(r)\sigma^2(r) = -\frac{1}{\pi R_0^2} \int_r^\infty \frac{d(\Sigma\sigma_p^2)}{dp} \frac{dp}{\sqrt{(R_0 p)^2 - r^2}}. \quad (4.2)$$

The derived functions¹¹ $n(r)$ and $\sigma^2(r)$ are then used to estimate the total enclosed mass $M(r)$ from the Jeans equation (Eq. 3.21). If there is a compact mass in the center, the enclosed mass curve will converge to m with decreasing radius, otherwise it should decrease to zero (Fig. 4.2).

¹¹In practice, the discrete p -bins that are used for estimating σ_p^2 and Σ are often too coarse for a stable solution of Eq. (4.2). Instead, some simple parametrized models are assumed for $n(r)$ and $\sigma^2(r)$, and the best fit parameters are obtained by the inverse equations $\Sigma(p) = 2R_0^2 \int_p^\infty nr(r^2 - R_0^2 p^2)^{-1/2} dr$ and $\Sigma(p)\sigma_p^2(p) = 2R_0^2 \int_p^\infty n\sigma^2 r(r^2 - R_0^2 p^2)^{-1/2} dr$.

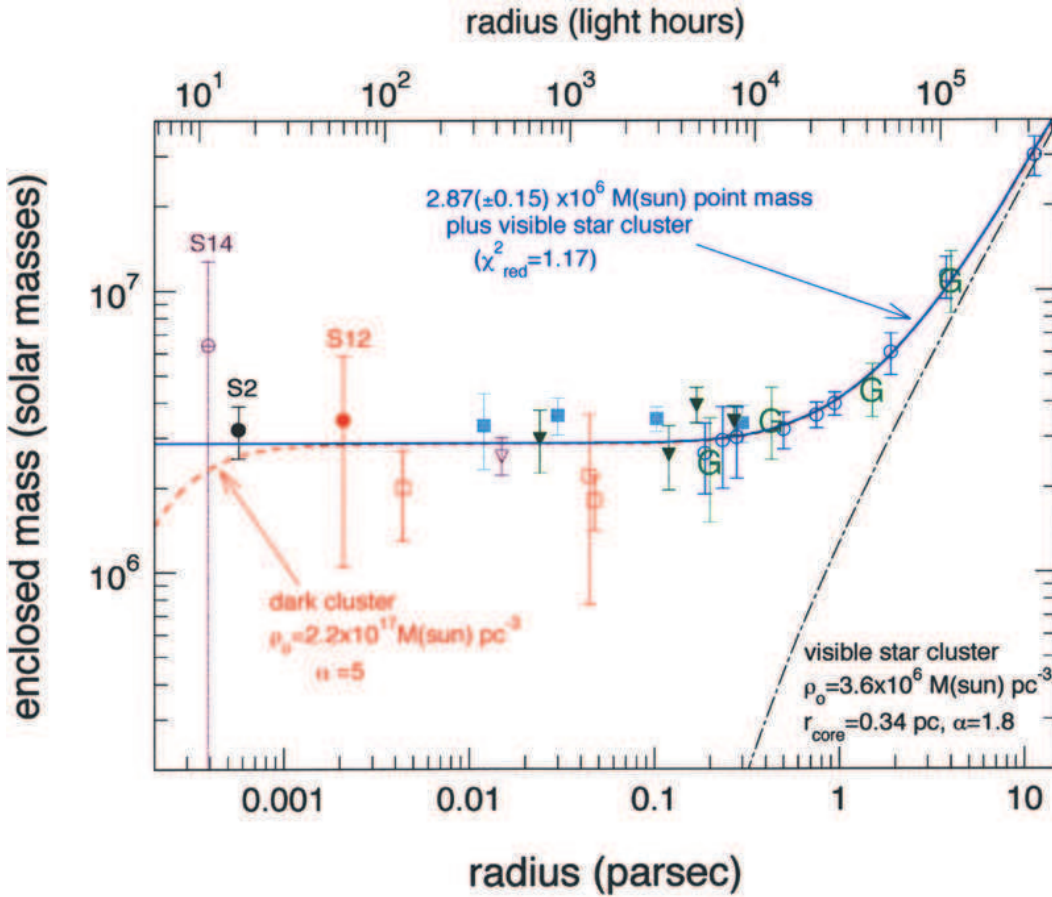


Figure 4.2: Enclosed mass distribution in the GC (Schödel et al. 2003) for $R_0 = 8$ kpc (Reid 1993). Filled circles: Orbital solutions. Filled triangles: Leonard-Merritt projected mass estimator (data from Schödel et al. 2003 and Ott et al. 2003). Open triangle: Bahcall-Tremaine mass estimator (Ghez et al. 1998). Filled rectangles: Jeans eq. solution for a parameterized anisotropic model (Genzel et al. 2000). Open circles: Jeans eq. solution for a parameterized isotropic model using radial velocities of late-type stars (Genzel et al. 1996). Open rectangles: Non-parametric mass estimator for an isotropic model (Chakrabarty & Saha 2001). “G”: Mass estimates from gas Doppler shifts (Genzel & Townes 1987). Solid line: Best fit to all data for a model of a central point mass with a stellar cluster. Dash-dot line: Mass in the stellar cluster alone—this model clearly does not fit the data. Dashed line: Visible cluster with a Plummer model of a hypothetical very compact dark cluster—this model marginally fits the data. (Reprinted with permission from the *Astrophysical Journal*)

When the data is too sparse to allow meaningful estimates of Σ and σ^2 , more elementary statistical estimators can be used that do not require binning or inversion from projected to 3D quantities. These can be obtained by taking moments of the Jeans equation, $\langle r^k M(< r) \rangle$ for integer k , and averaging over the stellar density (the virial theorem is also derived this way, see Leonard & Merritt 1989). Bahcall & Tremaine (1981) show that the virial theorem mass estimator

$$M_{\text{VT}} = \frac{3\pi}{2G} \langle z^2 \rangle / \langle 1/R_0 p \rangle, \quad (4.3)$$

where $\langle \dots \rangle$ denotes the sample average, is very biased and has other undesirable statistical proper-

ties. They propose instead a better behaved “projected mass estimator” for spherically symmetric and isotropic systems of test particles orbiting a dominant point mass, which uses line of sight motions,

$$M_{\text{BT}} = \frac{16}{\pi G} R_0 \langle \dot{z}^2 p \rangle. \quad (4.4)$$

Leonard & Merritt (1989) propose a related mass estimator for a spherically symmetric non-rotating system, which uses proper motions and is anisotropy-independent,

$$M_{\text{LM}} = \frac{16}{\pi G} R_0^3 \left\langle \left(\frac{2}{3} \dot{p}_{\parallel}^2 + \frac{1}{3} \dot{p}_{\perp}^2 \right) p \right\rangle, \quad (4.5)$$

where \dot{p}_{\parallel} and \dot{p}_{\perp} are the proper motions parallel and transverse to \mathbf{p} . This estimator is unbiased only when the sample covers the entire radial extent of the cluster and for cluster density profiles that have a finite mass. However, the stellar data in the GC do not satisfy either of these requirements (the observed power-law density, Eq. 3.24, can not be extrapolated to infinity as the total mass does not converge). The bias in M_{LM} then depends both on the anisotropy and the steepness of the cusp. This can be partially compensated for by correction factors (Genzel et al. 2000).

Chakrabarty & Saha (2001) propose a non-parametric mass estimation algorithm for a spherical and isotropic system that can use both line of sight velocities and proper motions. The method uses maximum likelihood to find the energy-binned DF and radius-binned potential that best reproduce the observed data.

A different approach for estimating the mass, the “Orbital Roulette” method, was proposed by Beloborodov & Levin (2004). The method assumes (as does the virial theorem) that at any given time the stars are at randomly distributed phases in their orbits. For any trial mass distribution, the orbits can be calculated and the phases tested for randomness. If the trial mass is too low, the stars will tend to have high velocities relative to the local escape velocity of the trial potential, and therefore will appear to be atypically close to periaapse. Conversely, if the trial mass is too high, the stars will appear to be atypically close to apoapse ($r_a = a(1+e)$, the maximal distance along the orbit). The best-fit mass distribution and its confidence interval can be identified by the location and shape of the phase-randomness maximum. This method cannot be applied directly to the stellar data in the GC, since it requires all 6 phase space coordinates of the stars, whereas only 5 are available at best. However, in the special case of stars in the inner thin disk, z can be derived from the constraint on the angular momentum \mathbf{J} . Initial results indicate that the Roulette method mass estimate is consistent with the higher values obtained by orbital mass estimates (§4.1.2) (A. Beloborodov and Y. Levin, private comm.).

Table (4.1) compares the statistical mass estimates for the central dark mass that were obtained by different authors using various methods and different data sets. The results all lie in the range $m \sim (2-3) \times 10^6 M_{\odot}$.

4.1.2 Orbital estimators

The first step toward orbital reconstruction is to detect accelerations (curvature) in the stellar motion. Measurements of acceleration can provide quite strong constraints on the properties of the dark mass even without full orbital information. The mean enclosed density of the dark mass can be directly obtained from projected quantities through Newton’s law of gravity (for an assumed angular position of the MBH),

$$\bar{\rho}_{2D} = \frac{3}{4\pi} \frac{m}{r^3} = \frac{3}{4\pi G} \frac{\ddot{r}}{r} = \frac{3}{4\pi G} \frac{\ddot{p}}{p}, \quad (4.6)$$

where r and \ddot{r} are the true 3D position and acceleration. The last equality holds because r and \ddot{r} are parallel, and so are decreased in projection by the same factor. For example, the position and

Table 4.1: Statistical mass estimates^a of the central dark mass (in $10^6 M_\odot$)

JE ^b	VT ^b	BT ^b	LM ^b	NP ^b	Distance	Refs ^c
2.5–3.2 z	1.7±0.6 z	1.9±0.6 z	—	—	< 0.2 pc	[1]
2.5±0.4 b	2.6±0.8 p	2.6±0.8 p	—	—	< 0.08 pc	[2]
—	2.5±0.2 p	2.6±0.2 p	—	—	< 0.2 pc	[3]
3.3 b	2.5–2.6 p	3.1±0.3 p	2.9±0.4 p	—	< 0.2pc	[4]
—	—	—	—	2.0±0.7 p	< 0.004 pc	[5]
—	—	—	—	2.2 ^{+1.6} _{-1.0} z	< 0.005 pc	[5]
—	—	—	—	1.8 ^{+0.4} _{-0.3} b	< 0.05 pc	[5]

^a Proper motion data is designated by (p), radial velocities by (z), both by (b).

^b JE: Jeans Equation, VT: Virial theorem, BT: Bahcall-Tremaine

^b LM: Leonard-Merritt, NP: Non-parametric

^c [1] Genzel et al. (1996), [2] Eckart & Genzel (1997), [3] Ghez et al. (1998)

^c [4] Genzel et al. (2000), [5] Chakrabarty & Saha (2001)

acceleration of the star S2 in 1997/1998 ($p = 150 \text{ mas}$, $\ddot{p} = 5.4 \text{ mas yr}^{-2}$, Ghez et al. 2000; Eckart et al. 2002) translate to a lower bound on the density of $\bar{\rho}_{2D} = 2 \times 10^{12} M_\odot \text{ pc}^{-3}$ or $\rho/\rho_{\text{BH}} = 3 \times 10^{-14}$ for $m = 4 \times 10^6 M_\odot$. Furthermore, since the projected acceleration vectors point to the projected position of the center of acceleration, they can locate the MBH in the IR frame (Ghez et al. 2000; Eckart et al. 2002) (Fig. 4.3).

When the inclination of the orbit is not known, the acceleration provides a lower limit on the MBH mass (for an assumed value of R_0),

$$m > R_0^3 \ddot{p} p^2 / G = m \cos^3 i, \quad (4.7)$$

where i is the inclination angle (see footnote 12). The measured accelerations of a few stars in the inner $\sim 0.5''$ give a lower bound of $m \gtrsim 10^6 M_\odot$ (Ghez et al 2000; Eckart et al. 2002; Schödel et al. 2003).

There is a close similarity between the S-stars orbiting the MBH and a planetary system (for example, $M_\star/m \sim M_{\text{Earth}}/M_\odot$ and $P_{\text{Jupiter}} \lesssim P_\star \lesssim P_{\text{Pluto}}$). The potential of the MBH completely dominates the dynamics, and perturbations by other stars can be neglected over the typical time span of the monitoring campaigns, $\sim \mathcal{O}(10 \text{ yr})$. Classical astronomical techniques for deriving the parameters of binary star systems from astrometric and spectroscopic observations can be directly applied, with only a few modifications (Salim & Gould 1999).

When considered separately, each of the stars forms a binary system with the MBH. A binary orbit is described by 14 parameters: 6 phase space parameters for the star and the MBH each, and the two masses¹². The mass of the star and the reflex motion of the MBH can be neglected because of the very large mass ratio. However, any constant velocity the MBH may have must be taken into account. This

¹²It is customary to describe a binary orbit in the reduced mass frame by 6 parameters (apart for the reduced mass): 2 parameters that determine the shape of the Keplerian ellipse, the semi-major axis a and the eccentricity e (Eq. 3.15), 1 parameter that determines the phase of the orbit, the time of periape passage t_0 , 2 angles that determine the orientation of the orbital plane in space, the inclination angle i (the angle between the line of sight and the normal to the orbital plane) and the longitude of the ascending node Ω (the position angle of the intersection between the plane of the sky and the orbital plane, the line of nodes), and 1 angle that determines the orientation of the ellipse in the orbital plane, the argument of pericenter ω (the angle between the line of nodes and the semi-major axis).

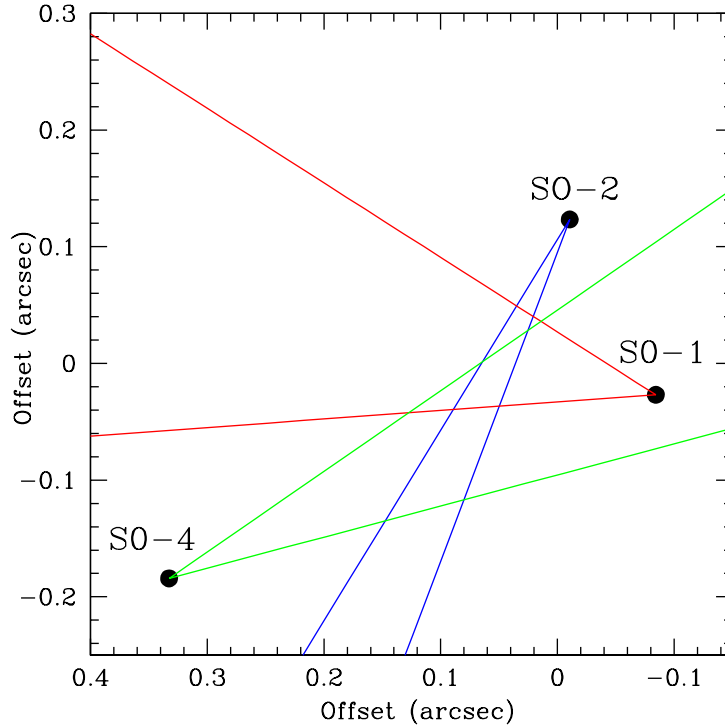


Figure 4.3: Pinpointing the position of the MBH in the IR frame by projected acceleration vectors (Ghez et al. 2000). The 1σ error wedges on the acceleration of 3 stars overlap in a region $\sim 0.05''$ from the nominal position of Sgr A* (at 0,0) as was initially derived from the alignment of the radio and IR grids by maser giants (Menten et al. 1997) (Reprinted with permission from *Nature*).

is in contrast with the case of visual stellar binaries (binaries where both stars are resolved), where the proper motion of the binary's center of mass is irrelevant since the *relative* position between the two stars is directly observed. Until recently the MBH was not detected in the IR, where the stars are observed, and so the stellar orbits were measured against the IR grid, and *not* relative to the position of the MBH itself. Now that Sgr A* is also observed in the IR¹³ (Genzel et al. 2003a; Ghez et al. 2004), the problem of solving the orbit will become easier. The results discussed here are still for the case of an invisible MBH.

In principle, one well sampled stellar orbit with precise astrometric measurements is enough to solve all the parameters of the system apart for two degeneracies: (1) Only the combination m/R_0^3 is fixed by the solution, but not m and R_0 separately (cf Eq. 3.15). (2) There remains a twofold degeneracy in the sign of the radial velocity. These degeneracies can be resolved with radial velocity information, in which case the MBH mass and the distance to the Galactic center can be determined (§4.1.3). The visual binary method for deriving distances utilizes the fact that the star's radial velocity \dot{z} is measured via the Doppler shift of the stellar spectral features in terms of an absolute velocity, whereas the proper motion $\dot{\mathbf{p}}$ is measured in terms of an angular velocity. The two are tied together by the orbital solution, $\dot{\mathbf{r}}_{\text{sol}}(t) = (R_0 \dot{\mathbf{p}}, \dot{z})$, thereby yielding the distance to the binary.

At present, the available orbital data for any single star is not sufficiently accurate to fully constrain

¹³Sgr A* is today easily detected in its flaring state, less so in its quiescent state, where it is only visible in part of the exposures. It is quite likely that with some improvements in the photometric sensitivity, Sgr A* will always be observable.

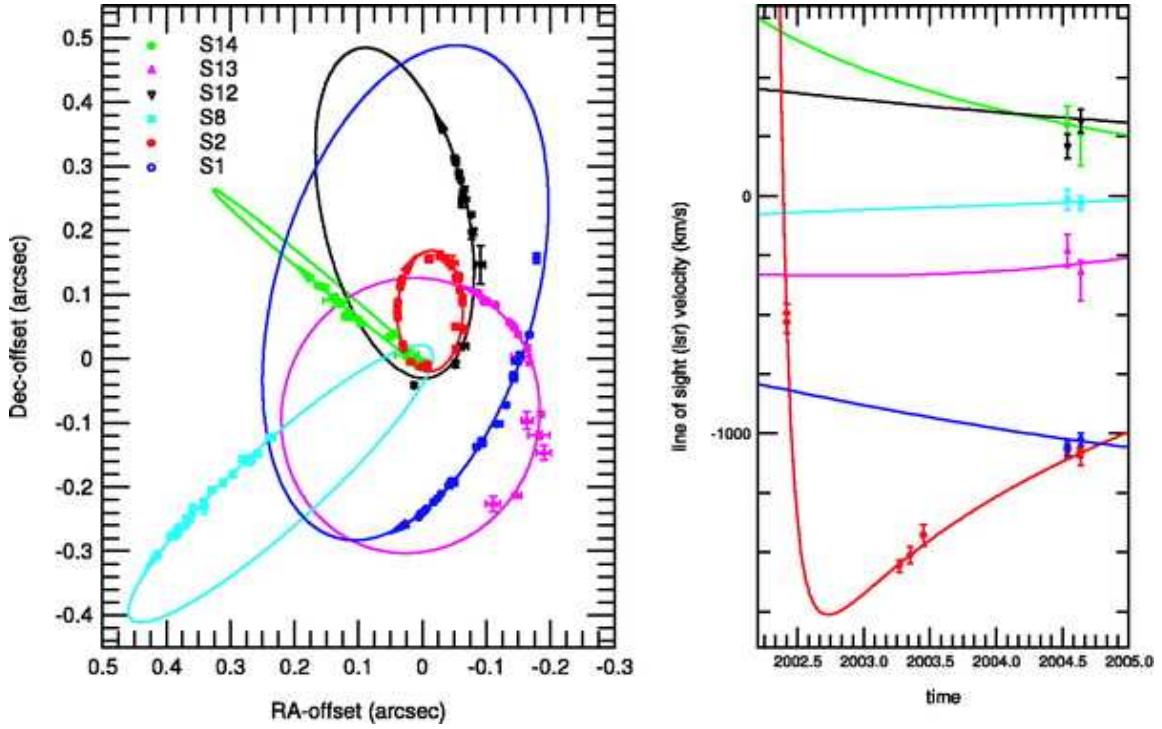


Figure 4.4: The projected orbits (left) and the radial velocity curve (right) of the 6 S-stars used by Eisenhauer et al. (2005) to solve for the mass, position and distance of the MBH. The points with error bars are the observed astrometric and spectroscopic data and the solid curves are the best fit multi-orbit solutions. (Reprinted with permission from the *Astrophysical Journal*).

the solution. Tighter constraints can be obtained by solving simultaneously several orbits (Salim & Gould 1999). Since all the stars are orbiting a common point, the MBH, the ratio of data points to free parameters is much improved and this can significantly reduce the errors on the derived parameters (Fig. 4.4). The best fit orbital parameters and their errors are then obtained by a non-linear least squares fit to the data.

Full 3D orbital solutions provide yet tighter constraints on the density of the central dark mass than Eq. (4.6). If the mass is fully contained in the orbit, as suggested by the fact that the orbit is consistent with Keplerian motion (§4.2), the mean density is

$$\bar{\rho}_{3D} = \frac{3}{4\pi} \frac{m}{r_p^3}. \quad (4.8)$$

The smallest periape discovered to date, $r_p = 0.22 \text{ mpc}$ for the star S0-16, raises the lower bound on the mean density to $\bar{\rho}_{3D} = 8 \times 10^{16} M_\odot \text{ pc}^{-3}$, or $\rho/\rho_{\text{BH}} = 10^{-9}$ for $m = 4 \times 10^6 M_\odot$ (Ghez et al. 2005). However, the tightest constraints on the compactness of the dark mass, $\rho > 7 \times 10^{21} M_\odot \text{ pc}^{-3}$, or $\rho/\rho_{\text{BH}} = 10^{-4}$ come not from stellar orbits, but from radio observations (Reid & Brunthaler 2004). These yield a lower limit on the mass associated with Sgr A* ($\gtrsim 4 \times 10^5 M_\odot$) based on the small peculiar velocity ($< 1 \text{ km s}^{-1}$ perpendicular to the Galactic plane), and an upper limit on the extent of the dark mass ($\lesssim 10^{13} \text{ cm}$) based on the assumption that it is contained within the millimeter radio emitting region (Doeleman et al. 2001; Bower et al. 2004).

Table (4.2) compares the orbital estimates for the mass, position and velocity of the dark mass that were obtained by different authors. The mass estimates all lie in the range $m \sim (3-4) \times 10^6 M_\odot$, which

Table 4.2: Orbital mass, position and velocity estimates for the central dark mass

m^a ($10^6 M_\odot$)	N_\star^b	R_0 (kpc)	Δp^c (mas)	\dot{p} (mas yr $^{-1}$)	Fixed parameters for MBH d	Refs e
3.7 ± 1.5 p	1	—	—	—	$\dot{\mathbf{p}} = \dot{z} = 0, \mathbf{p}, R_0$	[1]
3.6 ± 0.4 p	6	—	1.5	—	$\dot{\mathbf{p}} = \dot{z} = 0, R_0$	[2]
4.1 ± 0.6 b	1	—	2.4	—	$\dot{\mathbf{p}} = \dot{z} = 0, R_0$	[3]
3.59 ± 0.59 b	1	7.94 ± 0.42	1.7	—	$\dot{\mathbf{p}} = \dot{z} = 0$	[4]
3.7 ± 0.2 p	7	—	1.3	1.5 ± 0.5	$\dot{z} = 0, R_0$	[5]
3.61 ± 0.32 b	6	7.62 ± 0.32	1.7	—	$\dot{\mathbf{p}} = \dot{z} = 0$	[6]

a Proper motion data is designated by (p), both proper motion and radial velocities by (b).
 b Number of stars in orbital fit.
 c The uncertainty in the position of the center of acceleration in the IR grid, $\Delta p = (\Delta p_x^2 + \Delta p_y^2)^{1/2}$.
 d When fixed, R_0 is assumed to be 8 kpc.
 e [1] Schödel et al. (2002), [2] Ghez et al. (2003a), [3] Ghez et al. (2003b)
 e [4] Eisenhauer et al. (2003), [5] Ghez et al. (2005), [6] Eisenhauer et al. (2005)

is systematically higher than those derived from the statistical estimators $m \sim (2-3) \times 10^6 M_\odot$, (§4.1.1, table 4.1). The discrepancy with the orbital mass estimates is most marked for the low value from the non-parametric method (Chakrabarty & Saha 2001). This is puzzling, since non-parametric estimators are expected to be robust, but so are orbital mass estimators, which unlike the statistical estimators do not require assumptions about the properties of the stellar cluster. Orbital mass estimates are expected, if anything, to be slightly lower than the statistical mass estimates because they probe the potential closest to the MBH ($r \lesssim 0.02$ pc), where the mass fraction of any extended mass (e.g. stars, compact objects) should be negligible. The systematic differences cannot be attributed to uncertainties in R_0 , since all methods assume $R_0 = 8$ kpc. This discrepancy has not been studied in detail yet, and the reasons for it remain unclear.

4.1.3 Distance to the Galactic Center

The Sun-GC distance, R_0 , is a key parameter in the reconstruction of Galactic structure and dynamics as observed from our vantage point at the Solar system. For example, the current uncertainties in the values R_0 and the local Galactic rotation speed Θ_0 preclude the derivation of useful limits on the spheroidal axes ratios of the dark matter halo around the Galaxy, which could provide information on the nature of the dark matter (Olling & Merrifield 2001; see discussion in Weinberg, Milosavljević & Ghez 2005). The distance to the GC is also an important (though not the only) lower rung in the extragalactic distance scale, useful for calibrating standard candles such as RR Lyrae stars, Cepheids and red clump giants. Until recently, the adopted distance to the GC, $R_0 = 8.0 \pm 0.5$ kpc (Reid 1993) was based on the average of various primary (geometric), secondary (standard candles) and tertiary (theoretical models) distance indicators (see brief summary in Eisenhauer et al. 2003). Geometric distance indicators are in principle the most reliable, *if* the assumptions about physical properties of the system used are well founded.

An early attempt to use stellar observations in the GC to determine the distance to the GC was based on a general relation that holds in a spherical system and relates the line of sight velocity to the projected velocity through R_0 (e.g. Leonard & Merritt 1989),

$$\langle \dot{z}^2 p \rangle = R_0^2 \left\langle \left(\frac{2}{3} \dot{p}_\parallel^2 + \frac{1}{3} \dot{p}_\perp^2 \right) p \right\rangle. \quad (4.9)$$

The combined radial and proper motion data yield $R_0 = 8.2 \pm 0.9$ kpc (Genzel et al. 2000).

The visual binary method (Salim & Gould 1999; Jaroszynski 1999) uses precision measurements of proper motions and radial velocities of stars orbiting the MBH to provide a direct geometric determination of the Sun-MBH distance (§4.1.2). The only assumption is that the orbit is Keplerian. By virtue of its simplicity, this method is essentially free of systematic uncertainties due to uncertainties in the astrophysical modeling.

The first application of the visual binary method was based on the orbit of the star S2 (Eisenhauer et al. 2003). Since the data was not restrictive enough to constrain the 13 free parameters (§4.1.2), it was assumed that the 3 velocity components of the MBH can be taken as zero, in keeping with the low peculiar velocity measured in the radio ($\sim 25 \text{ km s}^{-1}$, Backer & Sramek 1999; Reid et al. 1999, 2003a) and the small error in the estimated velocity of the Solar system toward the GC. This analysis yielded $R_0 = 7.94 \pm 0.42$ kpc, $\Theta_0 = 220.7 \pm 12.7 \text{ km s}^{-1}$ and $m = (3.6 \pm 0.6) \times 10^6 M_\odot$. A subsequent analysis with more data (still assuming zero velocity for the MBH) yielded compatible values, $R_0 = 7.62 \pm 0.32$ kpc and $m = (3.6 \pm 0.3) \times 10^6 M_\odot$ (Eisenhauer et al. 2005).

4.2 Constraints on non-BH dark mass alternatives

A black hole, by its nature, is an object whose existence is hard to prove. Other than demonstrating the absence of a hard surface and a diverging gravitational redshift (the signature of an event horizon as seen by a stationary distant observer), one has to make do with placing ever tighter constraints on the volume enclosing the dark mass. Such limits can then be used to exclude non-BH dark mass models (that is, mass distributions that extend beyond their event horizon), such as a cluster of stellar-mass dark objects (§4.2.1) or “balls” of exotic particles (§4.2.2). Even if the existence of a MBH can be established, it is still possible, indeed quite likely, that it is surrounded by an extended distribution of dark mass, for example a dense cluster of massive compact stellar remnants that have sunk to the bottom of the potential well by the dynamical process of mass segregation (§4.2.3, §7.2). The stellar orbits tracked around the central dark mass probe the gravitational potential there at distances as small as ~ 10 light hours ($\sim 10^{15}$ cm). The information provided by these orbits offers the strongest case yet for the existence of a MBH in a galactic nucleus. Gravitational lensing may also be used to probe the distribution of the dark mass (§5.2.2, §5.2.3). Figure (4.5) summarizes the constraints on the size and density of the dark mass that are discussed below.

4.2.1 Cluster of dark stellar-mass objects

The most conservative dark mass alternative to a MBH is a very dense cluster of dark, or low-luminosity stellar mass objects. Possible candidates include very low mass stars ($M_\star \gtrsim 0.09 M_\odot$), brown dwarfs ($0.01 M_\odot \lesssim M_\star \lesssim 0.09 M_\odot$, failed stars that are not massive enough to ignite hydrogen), planets ($M_\star \lesssim 0.01 M_\odot$, where gravity is negligible compared to the electrostatic forces) or compact stellar remnants: white dwarfs (WDs) ($M_\star \lesssim 1.4 M_\odot$), NSs ($1.4 M_\odot \lesssim M_\star \lesssim 3 M_\odot$) and stellar mass black holes ($M_\star \gtrsim 3 M_\odot$). It is not at all obvious that stellar evolution and stellar dynamics can form a cluster of dark objects that is massive and concentrated enough to play the role of the central dark mass in the GC. However, irrespective of the formation history of such a hypothetical cluster, it is possible to invoke stability arguments to obtain robust upper limits on the cluster lifespan against the dynamical processes of evaporation and run-away collisions (Maoz 1998; §3.1.2). The lower this upper limit is compared to the age of the GC, the less likely is the dark cluster hypothesis.

Maoz (1998) obtained such limits for a sample of galaxies, including the Milky Way, where a dark mass m was detected inside a radius r_m . To obtain the most conservative limit, it was assumed that (1) the hypothetical cluster has the least centrally concentrated observed density profile (a Plummer model,

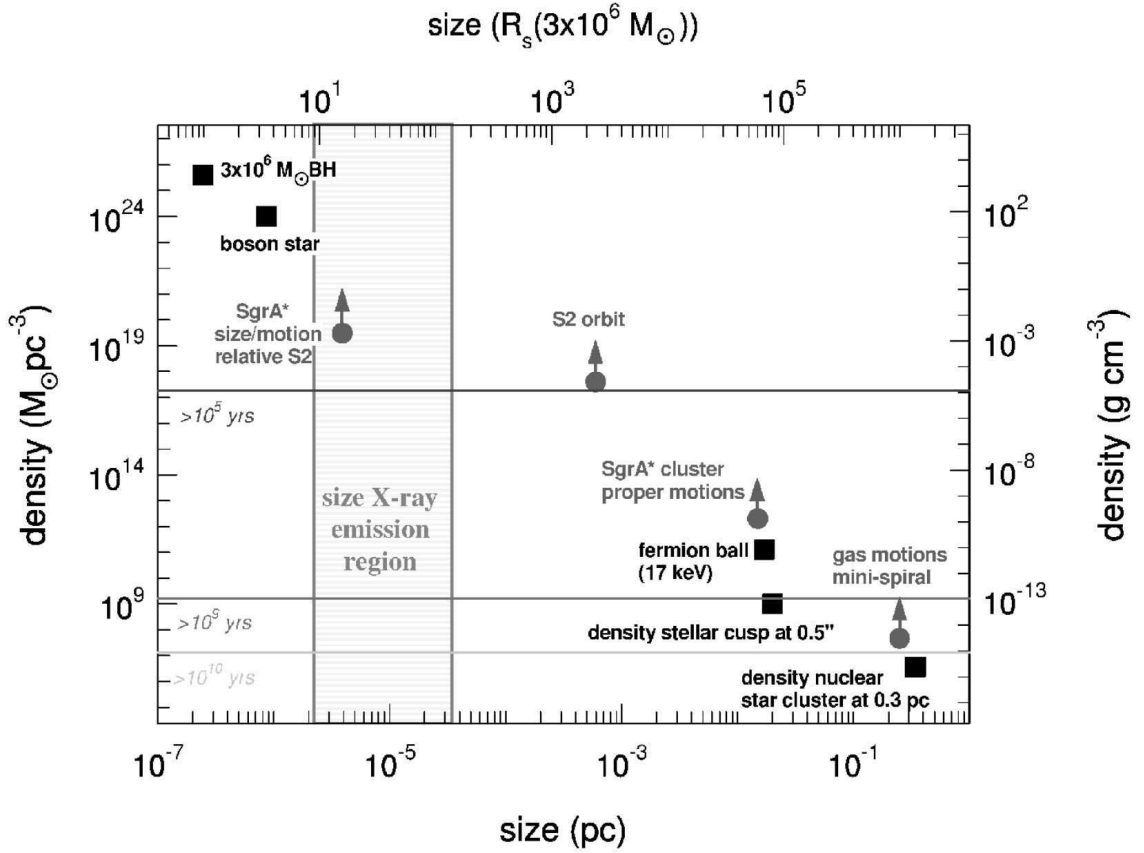


Figure 4.5: Compilation of the constraints on the nature of the dark mass in the GC (Schödel et al. 2003). Filled circles: Lower limits on the size and density of the dark mass. Grey area: Constraints on the size of the variable X-ray emitting region (Baganoff et al. 2001). Filled squares: Different dark mass candidates, including the visible star cluster and its central cusp, the heavy fermion ball (Tsiklauri & Viollier 1998), the boson star (Torres et al. 2000) and a $3 \times 10^6 M_\odot$ MBH. Horizontal lines: Lifetimes of hypothetical dark clusters of astrophysical objects, neutron stars, white dwarfs, or stellar black holes (Maoz 1998). The tightest constraint on the mass density, $\rho > \mathcal{O}(0.1 \text{ g cm}^{-3})$ (not shown) come from the radio proper motion of SgrA* compared to the velocities in the surrounding star cluster (Reid & Brunthaler 2004) under the assumption that the dark mass is enclosed in the millimeter radio source (Doeleman et al. 2001). All configurations are excluded except a black hole and a boson star. (Reprinted with permission from the *Astrophysical Journal*)

$\rho = \rho_0 / [1 + (r/r_0)^2]^{5/2}$), so as to minimize the collision rate; (2) it is composed of equal-mass objects, since otherwise mass segregation would accelerate its dynamical evolution; (3) the objects are at zero temperature, so as to minimize their radius for a given mass and thus minimize the collision rate (Eq. 3.11). A maximal lifespan t_m was obtained for each galaxy in the sample, based on the measured values of m and r_m , and by choosing the dark object that maximizes t_m ($0.6 M_\odot$ WDs in the case of the GC). The dark mass in the GC was estimated to have $t_m < 10^8 \text{ yr} \ll t_H$. This argues against the possibility that the dark mass is a dark cluster.

4.2.2 Exotic elementary particles

One interesting MBH alternative is that the dark masses in the centers of galaxies are the high density peaks of the cold dark matter distribution that is dynamically observed to exist on galactic and intergalactic scales (Tsiklauri & Viollier 1998; Munyaneza & Viollier 2002). This idea’s appeal lies in its economical use of a single component to explain dark mass on all scales. If dark matter is composed of fermionic elementary particles, then a massive compact “Fermion Ball” could support itself against gravity by degeneracy pressure, without having a hard surface (thereby avoiding tell-tale emission from matter impacting on the surface) and without being relativistic. Dynamically, such a configuration would be indistinguishable from a MBH for any process that occurs outside the ball. Deviations from Keplerian motion will become apparent only for orbits that cross through the ball. Also, a Fermi ball, unlike a low-mass MBH, will not necessarily induce tidal disruption since its size can exceed the tidal disruption radius (§6.1).

The maximal Fermi ball mass that can be supported by the degeneracy pressure of a fermion of mass m_f is set by the Oppenheimer-Volkoff limit (Oppenheimer & Volkoff 1939), the GR analog of the Chandrasekhar mass for WDs, $\max m \sim g_f^{-1/2} m_p^3 / m_f^2$, where g_f is the spin degeneracy factor of the fermion and $m_p \equiv \sqrt{\hbar c / G}$ is the Planck mass. By choosing a small enough m_f it is then possible to explain the entire range of galactic central dark masses as Fermi balls. The maximal measured central dark mass ($\max m \lesssim 3 \times 10^9 M_\odot$) then implies an upper limit on the fermion mass of

$$\max m_f = 0.62 (g_f/2)^{-1/4} \sqrt{\frac{m_p}{\max m}} m_p \sim (g_f/2)^{-1/4} 15 \text{ keV } c^{-2}. \quad (4.10)$$

The orbit of S0-2 is consistent, up to the measurement errors, with a Keplerian orbit around a point mass m . This one orbit can be used to rule out the universal Fermi ball alternative to MBHs (Munyaneza, Tsiklauri & Viollier 1998; Schödel et al. 2002). The lack of deviations from a Kepler orbit near the orbital periape implies that the Fermi ball must be wholly contained within the periape r_p . The velocity of S2 at periape is $\lesssim 0.02c$, and so a Fermi ball that fills the enclosed volume can be treated in the non-relativistic limit. The polytrope mass–radius relation (Chandrasekhar 1939) for a cold, non-relativistic degenerate Fermi ball results in a lower limit on the fermion mass

$$\min m_f = 1.76 (g_f/2)^{-1/4} \left(\frac{\ell_p}{r_p} \right)^{3/8} \left(\frac{m_p}{m} \right)^{1/8} m_p \sim (g_f/2)^{-1/4} 70 \text{ keV } c^{-2}, \quad (4.11)$$

where $\ell_p \equiv \sqrt{\hbar G / c^3}$ is the Planck length. Thus, there is no fermion mass that can simultaneously accommodate the orbital constraints of S2 on the extent of the dark mass in the GC and support the largest measured central dark masses. This rules out the possibility that the same component singly explains both the diffuse dark matter on galactic and intergalactic scales and the compact dark matter in the centers of galaxies.

Another proposed exotic particle alternative to a MBH, which cannot be ruled out by the stellar orbits, is the “Boson Star”. Such an object is composed of a scalar field and is supported against collapse by the Heisenberg uncertainty principle (Torres, Capozziello & Lambiase 2000). A wide range of boson star masses can be realized, including MBH masses, depending on the assumptions about the boson particle masses and their self-interactions. A boson star does not extend much beyond its event horizon, and is therefore strongly relativistic, but it does not possess a singularity, an horizon or a hard surface. Because both are so compact, stellar orbits cannot empirically distinguish between a MBH and a boson star. However, there are theoretical arguments against the dark mass being a boson star, since it is not clear that it can avoid accreting some matter and collapsing to a MBH. A boson star, unlike a MBH, has no capture orbits and so high velocity matter, such as that released in tidal disruption events,

will not accumulate in the center. However, this may not be enough to suppress the accretion of compact remnants on tightly bound orbits (§4.2.3) or gas flowing from the inner edge of an accretion disk.

4.2.3 Extended dark mass around the MBH

Even if a MBH does exist in the GC, it is still possible that there are other dark components around it, a cluster of massive compact objects (§3.3), a cusp of exotic particles, or a combination of the two. It should be noted that irrespective of the presence of the MBH, the Galactic dark matter halo is expected to peak at the GC (e.g. Navarro, Frenk & White 1996). The possibility that a steep, high density $\rho \sim \rho_h(r/r_h)^{-\alpha}$ cusp of self-interacting dark matter particles could form under the dynamical influence of the MBH (§3.1.3) was investigated in the hope that the enhanced particle annihilation rate ($\propto \rho^2$) could produce a detectable signal (Gondolo & Silk 1999; but see opposing conclusions by Merritt 2004b). The detection of strong TeV emission from the vicinity of Sgr A* (Kosack et al. 2004; Aharonian et al. 2004), further adds to the interest in this possibility. However, with a (very uncertain) normalization of only $\rho_h \sim 100 M_\odot \text{pc}^{-3}$ (Gnedin & Primack 2004), the mass in the dark matter particles is too small relative to the stellar cusp (Eq. 3.24) to be probed by the stellar orbits.

The smoothed potential of an extended dark mass component can be probed by deviations from an exact Keplerian orbit that will be displayed by a star that passes through the mass distribution. Such orbits will display a retrograde shift of the angle of periaapse (a receding rosette-like orbit), because the stellar acceleration at distance r from the center is proportional to the enclosed mass $M(<r)$ (spherical symmetry assumed), and it decreases as the star approaches periaapse. This shift is in the opposite sense of the effect expected for a GR orbit around a point mass (an advancing rosette-like orbit, §5.1). The retrograde periaapse shift per orbit $\Delta\omega$ due to a small spherical potential perturbation $\delta\phi$ on top of the potential of the MBH, $\phi = \phi_{\text{MBH}} + \delta\phi$, is given by (e.g. Landau & Lifshitz 1969)

$$\Delta\omega(a, e) = \frac{\partial}{\partial J} \left(\frac{2}{J} \int_0^\pi r^2 \delta\phi d\omega \right). \quad (4.12)$$

For a powerlaw extended mass distribution, parametrized as $M_e(<r) = m(r/r_m)^{3/2-p}$ (cf Eq. 3.17), the periaapse shift per orbit can be evaluated numerically by (see also Ivanov, Polnarev & Saha 2005)

$$\Delta\omega(a, e) = \left(\frac{a}{r_m} \right)^{3/2-p} \frac{2(1-e^2)^{3/2-p}}{e(1-2p)} \int_0^\pi \frac{4(2-p)e + [4(2-p) - (3-2p)(1-e^2)] \cos\omega}{(1+e\cos\omega)^{7/2-p}} d\omega. \quad (4.13)$$

Mouawad et al. (2005) show that the lack of detectable deviations from Keplerian motion in the orbit of S2 places an upper limit of $M_e(<r_a)/m < 0.05$ on the extended mass, where $r_a \simeq 0.01 \text{ pc}$ is the apoapse of S2. This upper limit still exceeds by a factor of ~ 30 the dynamical upper limit on the population of SBHs that can exist there (§3.3). Occasional orbital perturbations due to close encounters with individual compact objects can distinguish a dark matter component consisting of compact objects from a smooth particle dark matter distribution. Such perturbations may be detected by future very large telescopes ($\gg 10\text{m}$) (Weinberg, Milosavljević & Ghez 2005).

The orbits are not sensitive to the mass distribution inside the smallest periaapse (provided it is spherical). An upper limit on the fraction of the extended mass on these small scales ($\lesssim \text{few} \times \text{mpc}$) can be obtained from the Brownian motion of the mass that is associated with the radio source Sgr A* due to gravitational interactions with stars around it. The amplitude of the Brownian motion is strongly constrained by the radio limits on the peculiar motion of Sgr A* (motion in excess of the reflex motion induced by the Sun's orbit around the Galaxy). Brownian motion in a gravitating system is different from that in a gas, where the inter-molecular forces are short range forces. Equipartition arguments can not be directly applied. Inside r_h the potential is dominated by the MBH and the stars are “carried away”

with it as it moves; conservation of momentum rather than equipartition dictates the relation between the MBH velocity and mass and those of the stars. Neither is it possible to assign a well-defined temperature to the stellar system; the MBH itself affects the velocity field (“temperature”) of the stars near it (Merritt 2004a), and even outside r_h the stellar distribution is generally not isothermal (Chatterjee, Hernquist & Loeb 2002b, 2002a). Reid & Brunthaler (2004) use the radio observations to first show that if the mass associated with Sgr A* is some fraction of the total central mass, then it must lie very close to the center of the region delimited by the stellar orbits, otherwise it would have orbited rapidly around the dark mass, in contradiction with the upper bound on the peculiar motion of Sgr A* ($\sim 1 \text{ km s}^{-1}$ perpendicular to the galactic disk). They then proceed to assume that Sgr A* does lie in the center, and use N-body simulations of the Brownian motion to translate the upper bound on the peculiar motion to a lower bound of $\gtrsim 0.4 \times 10^6 M_\odot$ on the mass associated with Sgr A* (~ 0.1 of the dynamical mass measured by the orbits). This limit is consistent with the results of a more detailed formal analysis of Brownian motion in gravitating systems (Laun & Merritt 2004). It is unlikely that the large mass fraction (~ 0.9) that remains unconstrained is in fact non-BH dark matter. However, an order of magnitude improvement in the velocity resolution will be needed to confirm that the MBH indeed dominates the dark mass.

4.3 Limits on MBH binarity

Galaxies as observed today are thought to have formed by a chain of successive mergers of smaller galaxies. High redshift quasars and the large number of AGN found at smaller redshifts suggest that these mergers must also involve the formation of a binary MBH in the center of the newly merged galaxy, after the two MBHs rapidly sink in due to dynamical friction (§3.3). The binary subsequently decays, initially by dynamical processes, and finally by the emission of GW, and the two MBHs merge (see review by Merritt & Milosavljević 2004). In a “major merger” the two MBHs have comparable masses, whereas in a minor merger the mass ratio is large. The formation history of the Galactic MBH is not known, but there are several arguments that suggest that the Galactic MBH did not undergo a major merger, at least since it reached its present mass scale. Its small mass can be easily supplied, over time, by the stellar winds near it (§7.3) and so there is no compelling reason to assume mergers. Another argument against a major merger is the observed stellar distribution around the MBH (§3.2). Initially the binary’s orbit decays dynamically, by ejecting stars that pass near it out of the galactic core by 3-body interactions. A total stellar mass of the same order as the binary mass is ejected during a major merger, leaving behind a galaxy with a shallow central density distribution (Milosavljević et al. 2002). The GC, however, has a steep inner cusp. Furthermore, a binary MBH is expected to induce a tangential anisotropy in the stellar orbits by ejecting or destroying stars on radial orbits that approach it (Gebhardt 2003). This is not observed in the GC (Schödel et al. 2003).

Minor mergers, on the other hand, could well have occurred. The presence of a $\sim 10^3 M_\odot$ IBH is in fact suggested by the apparently self-bound stellar cluster IRS13, $\sim 0.15 \text{ pc}$ (projected) from the MBH (Maillard et al. 2004; but see opposing view by Schödel et al. 2005). It is also suggested by the “sinking cluster” model, which seeks to explain the young population in the center as originating in a dense, star forming stellar cluster with an IBH, which sank to the center by dynamical friction (Hansen & Milosavljević 2003; §7.2.3).

The binary MBH hypothesis can be constrained directly by the stellar orbits. The good fit of S2’s motion to a Keplerian orbit suggests that a hypothetical binary MBH must be contained in a region much smaller than the semi-major axis of S2, $\sim 5 \text{ mpc}$ (see Jaroszynski 2000 for a quantitative analysis). However, it is very unlikely that such a tight binary (of moderate mass ratio) exists now in the GC, given its very short lifespan against orbital decay and coalescence by the emission of GW radiation. The orbit of circular binary MBH (masses m_1 and m_2 and semi-major axis a_{12}) would shrink to a point by the

emission of GW radiation in time

$$t_{\text{GW}} = \frac{5}{256} \frac{c^5 a_{12}^4}{G^3 (m_1 + m_2) m_1 m_2}, \quad (4.14)$$

(Peters 1964; Shapiro & Teukolsky 1983 Eq. 16.4.10). For example, if $m_1 = m_2 = m/2 = 1.5 \times 10^6 M_\odot$ and $a_{12} = 0.1$ mpc, then the lifespan of the binary is only $t_{\text{GW}} = 10^4$ yr. MBH Binaries with smaller mass ratios are, however, much longer lived, and cannot be ruled out by this argument.

The MBH motion in the plane of the sky, $v \sim 2 \text{ mas yr}^{-1} = 76(R_0/8 \text{ kpc}) \text{ km s}^{-1}$, is obtained from the full orbital solutions (Ghez et al. 2005). A second BH orbiting the MBH would induce a reflex motion of the MBH around their common center of mass. This can be translated to an upper bound on the mass and distance of such a BH (assuming it lies outside the solved stellar orbits) of

$$m_2 \lesssim v \sqrt{\frac{m_1 r}{G}} \simeq 5 \times 10^5 \sqrt{\frac{r}{0.08 \text{ pc}}} M_\odot, \quad (4.15)$$

assuming a circular orbit in the plane of the sky and $m_2 \ll m_1 = 3 \times 10^6 M_\odot$ (see Hansen & Milosavljević 2003 for a more detailed analysis of the astrometric constraints on m_2 and a)

Tighter upper bounds can be obtained from the limits on the peculiar motion of Sgr A* in the radio of $18 \pm 7 \text{ km s}^{-1}$ in the plane of the galaxy and $0.4 \pm 0.9 \text{ km s}^{-1}$ perpendicular to it (Reid & Brunthaler 2004). However, these are *not* motions measured directly relative to the central cluster, but rather measured relative to extragalactic radio sources, and so include also the reflex motion, Θ_0/R_0 , which can not be subtracted exactly, and the possible Brownian motion of the central cluster relative to the Galactic center of mass, which is unknown. The upper limit on the perpendicular motion of $\sim 1 \text{ km s}^{-1}$ translates through Eq. (4.15) to an upper limit of $m_2 \lesssim 10^4 \sqrt{r/0.005 \text{ pc}} M_\odot$ (for $r > 0.005 \text{ pc}$). This upper bound is still consistent with a 10^3 – $10^4 M_\odot$ IBH in IRS13.

4.4 High-velocity runaway stars

A possible stellar signature of the existence of a MBH, or possibly a binary MBH, would be the discovery of very high velocity stars tens of kpc away from the GC moving with $v \sim \mathcal{O}(1000 \text{ km s}^{-1})$ on nearly radial orbits relative to the GC (the local escape velocity from the Galaxy at the Sun is $\sim 600 \text{ km s}^{-1}$, e.g. Wilkinson & Evans 1999). The stars can acquire such high velocities by exchange interactions deep in the potential of the MBH, either by the break-up of a binary on a nearly radial orbit (Hills 1988), by an encounter with another single star, or an encounter with a binary MBH (Yu & Tremaine 2003). A slow-moving star with velocity v_∞ far from the MBH will acquire near periaapse a very high velocity, $v^2 \sim 2Gm/r_p \gg v_\infty^2$. A small velocity perturbation by a gravitational interaction with a second mass, δv , can add $v\delta v \gg v_\infty^2/2$ to the orbital energy of the star, and take away the same amount from the other mass (a similar mechanism forcefully expels tidal ejecta, see §6.1.2). Yu & Tremaine (2003) find that stellar binary exchanges or encounters with a binary MBH can populate the Galaxy with high velocity stars at a substantial rate ($\gtrsim 10^{-5} \text{ yr}^{-1}$), resulting in up to $\sim 10^3$ high velocity stars ($v_\infty > 1000 \text{ km s}^{-1}$) inside the Solar circle.

Intriguingly, Brown et al. (2005) report the discovery of the highest velocity star ever observed in the Galactic halo, moving with a radial velocity of 710 km s^{-1} at a distance of $\sim 55 \text{ kpc}$. Its direction of motion could be consistent with radial motion away from the GC, if the (unknown) transverse velocity components are small. The stellar spectrum does not identify its spectral type unambiguously, but one of the two possibilities is a B9 MS star, such as those found in the S-cluster (the other possibility is a blue horizontal branch giant).

5 Probing post-Newtonian gravity near the MBH

General Relativity (GR) is the least tested of the theories of the four fundamental forces of nature. An important goal of the study of stars near the Galactic MBH is to detect post-Newtonian effects and probe GR in the weak and strong field limits near a super-massive object. Three classes of effects are discussed in this context. The first is relativistic celestial mechanics. Stars are observed moving with velocities of up to $v \sim \text{few} \times 0.01c$ at distances of $\lesssim 10^3 r_S$ from a mass of $\sim 4 \times 10^6 M_\odot$. This regime of GR dynamics is virtually unexplored¹⁴ (§5.1). For comparison, the high precision confirmation of the predictions of GR in the Hulse-Taylor binary pulsar (PSR 1913+16) were for masses of $\sim 1.4 M_\odot$ with $v \sim 0.003c$ at $r_p \sim 2 \times 10^5 r_S$ (Taylor & Weisberg 1989). The second class of weak field phenomena that may be relevant in the GC is gravitational lensing (§5.2). The lensed stars are not necessarily related to the stars near the MBH, since it is only their projected angular distance to the MBH that has to be small, but their true (3D) position can be anywhere behind the MBH. The third class of GR effects that may be relevant in the GC is the emission of GW from very low-mass stars that spiral into the MBH. This dissipative process is discussed separately in (§6.2.2).

5.1 Relativistic orbital effects

At present, all the available orbital data can be adequately modeled, within the measurement errors, in terms of Newtonian motion. With improved resolution, higher precision and a longer baseline, deviations from Keplerian orbits may be detectable. This will likely be a challenging task. The chances of success will be much improved if future observations detect fainter stars on even tighter and more eccentric orbits than the relatively bright ones observed today. This is because post-Newtonian effects are larger the tighter the orbit, while the uncertainty due to the dynamical influence of the unknown amount of extended mass around the MBH (§4.2.3) is minimized. However, it is not clear how many faint, low-mass stars exist in the inner few mpc, since mass segregation and possibly also collisional destruction by the massive remnants there are expected to suppress their numbers there.

The highest stellar velocity recorded to date in the GC was that of the star S0-16 during periape passage (Ghez et al. 2005), which reached $\sim 12000 \text{ km s}^{-1}$ ($\beta \sim 0.04$, $\beta \equiv v/c$) at a distance of $r_p \sim 600 r_S$ from the MBH. This corresponds to a relativistic parameter $\Upsilon \equiv r_S/r$ at periape of $\Upsilon(r_p) \sim 1.6 \times 10^{-3}$. For comparison, the relativistic parameter on the surface of a WD is a few $\times 10^{-4}$ and on a NS a few $\times 10^{-1}$. The relativistic parameter changes along the orbit. When the orbit is only mildly relativistic, it obeys a nearly Keplerian energy equation (Eqs. 3.15, 3.16) and Υ can be expressed as

$$\Upsilon = \beta^2 + \frac{Gm}{c^2 a} \equiv \beta^2 + \Upsilon_0. \quad (5.1)$$

When $e \gg 0$ and the star is near periape, $\beta^2 \gg \Upsilon_0$ and $\Upsilon \sim \beta^2$. The deviations from Newtonian mechanics become more pronounced as Υ increases. For $\Upsilon \ll 1$ (as is the case here) it is useful to expand the post-Newtonian deviations in β , and classify each effect by the order of its β -dependence (equivalently, by the order of its $\sqrt{r_S/r_p}$ or $\sqrt{r_S/a}$ dependence).

¹⁴Gas processes probe the dynamics much closer to the MBH, but are also much harder to interpret both observationally and theoretically. Emission from accreting gas is observed from the strong field near the event horizon of MBHs. There is tentative evidence of gravitational redshift in the Fe $K\alpha$ line profiles in AGN (e.g. Fabian et al. 1995, but see e.g. Page et al. 2004). The emission from Galactic SBHs and AGN sometimes display quasi-periodic oscillations that can be interpreted as coming from the last stable orbit around a spinning BH (see Genzel et al. 2003a; Aschenbach et al. 2004 for such evidence from the Galactic MBH).

5.1.1 Gravitational redshift

The measurement of stellar proper motions and accelerations in the inner arcsecond of the GC (Eckart & Genzel 1996; Ghez et al. 1998) preceded by more than a decade the measurement of radial velocities for these stars (Ghez et al. 2003b; Eisenhauer et al. 2003). For this reason, most theoretical studies of the detection of post-Newtonian orbits in the GC focused exclusively or mainly on proper motions and effects related to them, such as periaapse shift (Jaroszynski 1998b; Fragile & Mathews 2000; Rubilar & Eckart 2001; see also general treatise on relativistic celestial mechanics by Brumberg 1991). However, with the advent of adaptive optics assisted IR imaging spectroscopy, it now appears that it is the radial velocities, rather than the proper motions, that may provide the tightest constraints on deviations from Newtonian orbits. The current quality of spectroscopic observations allows the determination of radial velocities from the Doppler shift of stellar spectra to within $\delta v \sim 25 \text{ km s}^{-1}$, or $\delta \lambda / \lambda \sim 10^{-4}$ (Eisenhauer et al. 2005). This limit is partly instrumental and partly due to the fact that the stars very close to the MBH have hot (“early type”) stellar spectra (§2.2, §7) with only a few strong IR lines, which are typically broad with $\langle v_{\text{rot}} \sin i \rangle \sim 150 \text{ km s}^{-1}$ (Ghez et al. 2003b; Eisenhauer et al. 2005; Fig. 4.1).

The observed radial velocity β_r can be expanded in terms of the true magnitude of the 3D stellar velocity β as

$$\beta_r = \Delta \lambda / \lambda = B_0 + B_1 \beta + B_2 \beta^2 + \mathcal{O}(\beta^3). \quad (5.2)$$

Several Newtonian and post-Newtonian terms contribute to the three leading orders. The relativistic Doppler shift

$$\beta_D = \frac{1 + \beta \cos \vartheta}{\sqrt{1 - \beta^2}} - 1 \simeq \beta \cos \vartheta + \frac{1}{2} \beta^2, \quad (5.3)$$

can be decomposed to the first order classical Doppler effect (ϑ is the angle between the velocity vector β and the line of sight) and to the second order transverse relativistic Doppler redshift. The gravitational redshift of a source at distance r from the MBH as measured by an observer at infinity (Eq. 5.1) is

$$\beta_z = \frac{\Delta \lambda}{\lambda} = \left(1 - \frac{r_S}{r}\right)^{-1/2} - 1 \simeq \frac{1}{2} \Upsilon(r) = \frac{1}{2} [\Upsilon_0(a) + \beta^2]. \quad (5.4)$$

The gravitational redshift contributes a constant term, which depends on the orbital semi-major axis, or equivalently, the energy, and a second order term of the same magnitude as the transverse Doppler redshift.

The Roemer (or light travel time) delay is a Newtonian effect caused by the fact that the light travel time from the star to the observer changes with the orbital phase when the orbital plane is not observed face-on (see also Loeb 2003). The phase-dependent mismatch between the signal’s emission and arrival times leads to apparent deviations from the Newtonian orbit. The exact value of the effect depends on the orbital parameters. Its magnitude and β -dependence can be estimated by considering a circular edge-on orbit, in which case the maximal delay is the light crossing time of the diameter of the orbit $\delta t \sim 2a/c$ and the maximal apparent velocity shift is $\beta_R \sim |\dot{\beta}_r| \delta t \sim (Gm/ca^2) \delta t = 2\beta^2$. The Roemer time delay enters radial velocity measurements as a $\mathcal{O}(\beta^2)$ correction, with a pre-factor B_R that is typically larger than that of either the transverse Doppler shift or the gravitational redshift. Note that the Roemer delay expresses itself in the proper motions as a *relative* shift $\delta r/a$ of order $\mathcal{O}(\beta)$, since $\delta r/a \sim (2a/a)(\delta t/P) \sim 2\beta$.

The observed radial velocity (Eq. 5.2) can therefore be written as

$$\beta_r = \left[\beta_\odot + \beta_{z,\text{gal}} + \beta_{z,*} + \frac{1}{2} \Upsilon_0 \right] + [\cos \vartheta] \beta + [1 + B_R] \beta^2 + \mathcal{O}(\beta^3), \quad (5.5)$$

where the constant coefficient B_0 is expressed in terms of (1) the constant velocity shift β_\odot due to the compound motion of the Sun and the Earth relative to the GC as well as the blueshift due to the potential wells of the Sun, Earth and planets ; (2) the constant velocity shift $\beta_{z,\text{gal}}$ due to redshift by the potential of the Galaxy; (3) the gravitational redshift $\beta_{z,*}$ due to the star's potential¹⁵, and (4) The constant contribution $\Upsilon_0/2$ from the gravitational redshift of the star in the potential well of the MBH.

Since stars are observed with $\beta \sim \text{few} \times 0.01$ at periape and since $B_2 = 1 + B_R \sim \mathcal{O}(1)$, it follows that second order effects are detectable with existing instruments, $B_2\beta^2 \sim 10^{-3} > \delta\lambda/\lambda \sim 10^{-4}$. Third order GR effects, such as frame dragging (§5.1.3), Gravitational lensing and the Shapiro delay (relevant only for a nearly edge-on orbit and even then very small, Kopeikin & Ozernoy 1999), or GR periape shift (§5.1.2), which is only a $\Delta\beta \sim \Delta\omega r_p/\tau_p \sim \mathcal{O}(\beta^3)$ (Eq. 5.6) effect in the radial velocities (although it is a $\mathcal{O}(\beta^2)$ effect in the proper motions) will not be detectable with the available radial velocity data. It should be noted that second order effects involving proper motion, such as the relativistic periape shift, will be very hard to detect with the present astrometric precision.

In practice, the ability to measure the post-Newtonian deviations from a Newtonian orbit requires an accurate determination of the Keplerian parameters, and so reliable proper motion data are still needed. In particular, radial velocity data for a single star on a $\mathcal{O}(\beta^2)$ post-Newtonian orbit can always be expressed as a Newtonian orbit (including the classical Roemer effect) with suitably modified orbital parameters (the degeneracy between Υ_0 and β_\odot in Eq. 5.5 is an expression of this fact). Multiple orbits and proper motions are needed to break this degeneracy (Zucker & Alexander 2005, in preparation). Post-Newtonian orbit solving simulations with proper motions and radial velocities, such as those conducted by Weinberg, Milosavljević & Ghez (2005) for Newtonian orbits, are needed to assess the practical observational requirements for detecting these effects.

A similar approach to detecting post-Newtonian effects with radio pulsars, which may exist around the MBH, was studied by Pfahl & Loeb (2004). The problems are that it is unknown whether such a population exists, and that radio observations at the required sensitivity will be extremely challenging (cf §3.3).

5.1.2 Periape shift

The deviation of the GR potential from the Newtonian $1/r$ point mass potential leads to rosette-like orbits with a prograde shift in the argument of pericenter ω (see footnote 12) of $\Delta\omega$ per orbit, which for a non-rotating black hole is (Weinberg 1972, Eq. 8.6.11)

$$\Delta\omega = \frac{3\pi}{(1-e^2)} \frac{r_S}{a}. \quad (5.6)$$

The periape advance is a $\mathcal{O}(\beta^2)$ effect. The effect of the periape advance on the orbital shape is maximal at the apoapse. The change in the angular position of the apoapse, \mathbf{p}_a , per orbit (neglecting corrections for the orbital orientation) depends only on the orbital eccentricity,

$$\Delta p_a \sim \Delta\omega \frac{a(1+e)}{R_0} = \frac{3\pi r_S}{(1-e)R_0}. \quad (5.7)$$

¹⁵The constant terms β_\odot , $\beta_{z,\text{gal}}$ and $\beta_{z,*}$ are very small compared to $B_2\beta^2$ ($cB_2\beta^2 \sim \mathcal{O}(100\text{km s}^{-1})$ at periape for S2/S0-2). The peculiar radial motion of the sun relative to the GC is estimated to be $< 10\text{km s}^{-1}$ (Gould & Popowski 1998) and the transverse Doppler redshift is $\Theta_0^2/2c \simeq 0.08\text{km s}^{-1}$. The constant gravitational redshift due to the Galactic potential (in addition to that of the BH, which is taken into account by Eq. 5.4) is $c\beta_{z,\text{gal}} \sim \Theta_0^2/c \simeq 0.16\text{km s}^{-1}$. The gravitational blueshift due to the proximity of the Sun is only $-v_\oplus^2/c = -0.003\text{km s}^{-1}$, where $v_\oplus \simeq 30\text{km s}^{-1}$ is the Earth's orbital velocity. Likewise, the redshift due to the star's potential and the blueshift due to the Earth's potential are only $c\beta_{z,*} \sim 1\text{km s}^{-1}$ and $-GM_\oplus/cR_\oplus \simeq -0.0002\text{km s}^{-1}$ respectively.

For S2/S0-2, the shortest period star detected to date ($P \sim 15$ yr, $a \sim 4.5$ mpc, $e \sim 0.88$ Eisenhauer et al. 2005; Ghez et al. 2005), the shift is $\Delta p_a \sim 1$ mas per period. A similar shift is predicted for the star S14/S0-16 with the most eccentric orbit solved to date ($P \sim 38$ yr, $e \sim 0.94$). A more efficient use of the orbital data is to fit an orbital model including the periastron shift (i.e. with a variable argument of periastron ω) to all the data points. Either way, unless a very eccentric, very short period star is discovered, the detection of the periastron advance will require very long monitoring (see detailed discussions of the observability of the effect by Jaroszynski 1998b; Fragile & Mathews 2000; Rubilar & Eckart 2001; Weinberg, Milosavljević & Ghez 2005).

The prospects of discovering the GR periastron advance are further complicated by the likely existence of a distribution of faint stars and dark stellar remnants around the MBH, which introduces a retrograde periastron shift (§4.2.3, §3.3). Measurements of the periastron shifts in several stellar orbits will be needed to disentangle the two countervailing effects (Rubilar & Eckart 2001).

5.1.3 Frame dragging

There is some evidence from the variability of the IR and X-ray accretion flares that the Galactic MBH is spinning in at least half its maximal allowed rate (Genzel et al. 2003a; Aschenbach et al. 2004). A spinning mass with specific spin S_\bullet induces secular changes in the trajectory of a test particle orbiting it through gravitomagnetic GR effects known as “frame dragging” or Lense-Thirring precession¹⁶. The S_\bullet -induced change in the longitude of the ascending node Ω (see footnote 12) corresponds to the precession of the orbital angular momentum vector \mathbf{J} around the MBH spin vector \mathbf{S}_\bullet . The change in the argument of pericenter, ω , corresponds to a periastron shift, in addition to the S_\bullet -independent shift (Eq. 5.6).

In the weak field limit, the change per orbital period in Ω is (Thirring & Lense 1918)

$$\Delta\Omega_{\text{LT}} = \sqrt{2}\pi \frac{s}{(1-e^2)^{3/2}} \left(\frac{r_S}{a}\right)^{3/2}, \quad (5.8)$$

and the period of the precession is

$$P_{\Omega_{\text{LT}}} = 4\pi \frac{r_S}{c} \frac{(1-e^2)^{3/2}}{s} \left(\frac{a}{r_S}\right)^3, \quad (5.9)$$

where $s \equiv S_\bullet/(Gm/c)$ is the dimensionless spin parameter ($0 \leq s \leq 1$). The change per orbital period in the argument of pericenter is

$$\Delta\omega_{\text{LT}} = -3\Delta\Omega_{\text{LT}} \cos i, \quad (5.10)$$

where $\cos i \equiv \mathbf{J} \cdot \mathbf{S}_\bullet / JS_\bullet$. The frame dragging shifts are $\mathcal{O}(\beta^3)$ effects.

The predicted magnitude of the effect in the GC is small (Jaroszynski 1998b), and it is unlikely that it will be measured directly from the orbits even with the proposed Thirty Meter Telescope (Weinberg, Milosavljević & Ghez 2005). However, over the lifespan of one of the young S-stars near the MBH, $t_\star \sim 10$ Myr, the accumulated precession can be substantial if the orbit is eccentric enough. Levin & Beloborodov (2003) note that for the eccentric, short-period star S2/S0-2 ($P_\star = 15.2$ yr, $e = 0.87$, Schödel et al. 2002) the Lense-Thirring period is $P_{\Omega_{\text{LT}}} \sim \mathcal{O}(10^7)$ yr. They propose that S2 was initially a member of the thin star disk (§2.2), orbiting in the plane of the disk but on a particularly eccentric orbit, and that it was gradually dragged out of the plane by the Lense-Thirring effect, to the point where its orbit today appears unrelated to the disk. Such effect, if measured in two stars could be used to determine the

¹⁶A related but distinct gravitomagnetic effect, not discussed here, is the Lense-Thirring precession of the spin of the test particle itself.

spin axis. They further propose that this could be the origin of the other S-stars as well. However, the orbital solutions of several other S-stars do not support this idea, since for a large fraction of the S-stars $P_{\Omega_{LT}} \gg t_*$ (Eisenhauer et al. 2005).

5.2 Gravitational lensing

Gravitational lensing of stars by the Galactic MBH differs from the other stellar processes discussed here in that it is a process that affects the light emitted by the stars, rather than the stars themselves, and in that the lensed stars are typically well outside the dynamical region of influence of the MBH. However, the lensed images can masquerade as stars near the MBH or as accretion flares from the MBH and complicate the interpretation of the observations. On the other hand, gravitational lensing may be used to probe the dark mass and the stars around it, and to locate the MBH on the IR grid, where the stars are observed.

There is yet no clear evidence for gravitational lensing by the MBH. This is consistent with various estimates that suggest that there are not enough luminous sources behind the MBH for gravitational lensing to be important for present-day observations, although future, deep observations may detect lensing events (Wardle & Yusef-Zadeh 1992; Jaroszynski 1998a; Alexander & Sternberg 1999; Alexander & Loeb 2001). Nevertheless, it is worthwhile to consider the possible roles of gravitational lensing in the observations and study of the Galactic Center. This is important not only in anticipation of future observations, but also because the estimates of the lensing probability are quite uncertain (they involve models of the unobserved far side of the Galaxy) and may under-estimate the true rate of such events.

5.2.1 Point mass gravitational lens

The MBH dominates the central potential and so gravitational lensing in the GC can be described to first approximation as lensing by a point mass. A light ray arriving from a background source to the observer is bent by an angle α_L as it passes near a point mass lens (Fig. 5.1). In the small angle approximation, which is valid as long as the impact parameter b_L is much larger than the event horizon ($b_L \gg r_S$), the bending angle is given by

$$\alpha_L = 2r_S/b_L, \quad (5.11)$$

(see Schneider, Ehlers & Falco 1992 for a comprehensive treatment of gravitational lensing). The bending angle of a point mass gravitational lens diverges towards the center ($b_L=0$) and decreases as the impact parameter grows. This is in the opposite sense to a spherical glass lens, where the bending angle is zero when the ray goes through the lens center and increases with the impact parameter. Thus, unlike a spherical lens, a point mass gravitational lens does not produce a faithful image of the lensed source, but rather breaks, warps and/or flips the image. A point mass lens creates two images of the source, one on either side of the lens. The two images are always in focus at the observer, regardless of the distance of the source behind the lens. By symmetry, the two images, the lens and the (unobserved) source all lie on one line (Fig. 5.2). The typical angular cross-section of the lens is given by the Einstein angle,

$$\theta_E = \sqrt{2r_S \frac{D_{LS}}{D_{OS}D_{OL}}}, \quad (5.12)$$

where D_{OL} is the observer-lens distance (R_0 for the Galactic MBH), D_{LS} is the lens-source distance, and D_{OS} is the observer-source distance¹⁷. The physical size of the Einstein angle at the source plane is

¹⁷In a flat background spacetime, which is the relevant background for lensing on Galactic scales, $D_{OS}=D_{OL}+D_{LS}$. In curved spacetime, which is the relevant background for lensing on cosmological scales, the distances are

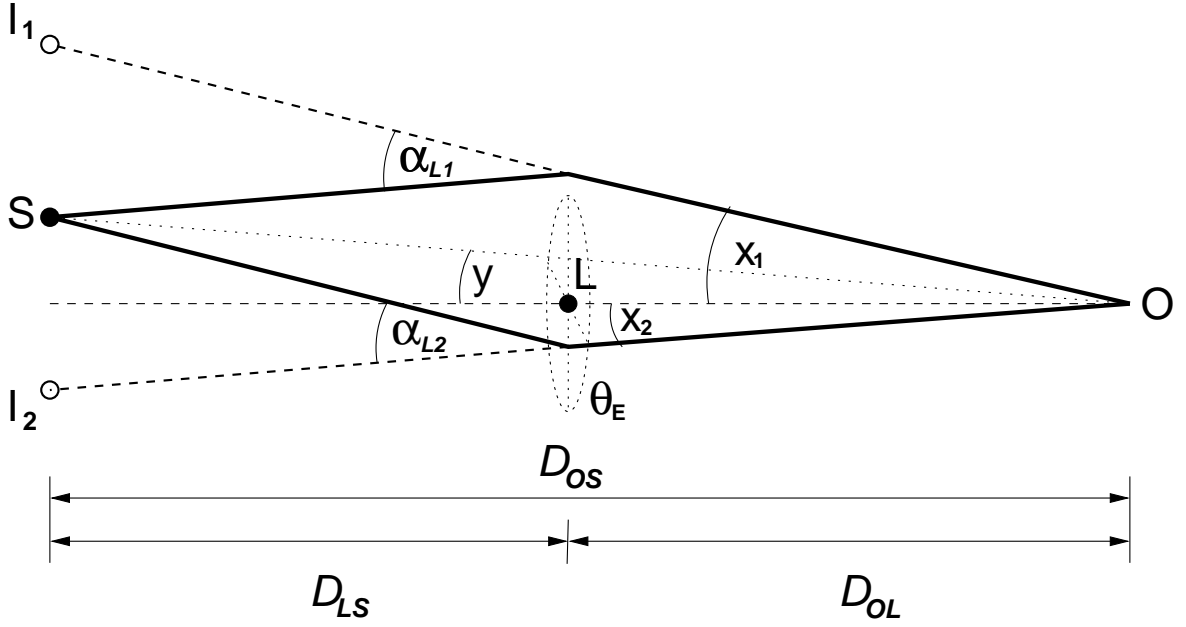


Figure 5.1: Schematics of gravitational lensing by a point mass in the small bending angle limit. An observer (O) sees light rays from a background source (S), which is located at a distance D_{OS} away, deflected by angles α_{L1} , α_{L2} in the potential of a massive lens (L), which is located at a distance D_{OL} from the observer and D_{LS} from the source. The lens mass and the distances define an Einstein ring of angular opening θ_E (Eq. 5.12), perpendicular to the optical axis (O–L). The source (S), which is not observed directly, is located at an angle $y\theta_E$ relative to the optical axis. It appears as two lensed images (I_1 , I_2) at angular positions $x_1\theta_E$ and $x_2\theta_E$, one inside the Einstein ring and one outside it.

$R_E = D_{OS}\theta_E$. At a fixed observer-lens distance, θ_E reaches a maximal value for a source at infinity,

$$\theta_E = \theta_\infty \sqrt{\frac{D_{LS}}{D_{OS}}}, \quad \theta_\infty = \sqrt{\frac{4Gm}{c^2 D_{OL}}} \sim 2'' \text{ in the GC.} \quad (5.13)$$

The relation between y , the angular position of the source relative to the observer-lens axis (the optical axis) and $x_{1,2}$, the angular positions of the images, can be derived from the geometry of the light paths in the small bending angle limit (Fig. 5.1),

$$y = x_{1,2} - 1/x_{1,2}, \quad \text{or} \quad x_{1,2} = \frac{1}{2} \left(y \pm \sqrt{4 + y^2} \right) \quad (5.14)$$

where $x_{1,2}$ and y are measured in terms of θ_E and $x_2 < 0$ by definition. The angular separation between the two images is $\mathcal{O}(\theta_E)$. Gravitational lensing conserves surface brightness, and so the magnification $A_{1,2}$ in the flux of each image relative to that of the unlensed source is proportional to the apparent change in the angular area of the source,

$$A_{1,2} = \left| \partial \mathbf{y} / \partial \mathbf{x}_{1,2} \right|^{-1} = \left| 1 - x_{1,2}^{-4} \right|^{-1}. \quad (5.15)$$

the angular diameter distances, and this simple sum no longer holds.

The primary image at x_1 is always magnified. The secondary image at x_2 can be demagnified to zero. The two magnifications obey the relations

$$A_1 = A_2 + 1 \geq 1, \quad A \equiv A_1 + A_2 = \frac{y^2 + 2}{y\sqrt{y^2 + 4}}. \quad (5.16)$$

When $y=0$ the magnification formally diverges and the image appears as a ring of angular size θ_E , the Einstein ring. This divergence is avoided in practice by the finite size of the source (e.g. a star). Finite sized sources are also sheared tangentially around the Einstein ring as the magnification increases. In the limit of high magnification, or small source angle ($y \ll 1$), $A \sim 1/y$. It is customary to define $A(y=1)=1.34$ as the threshold of a microlensing event.

Relative motion between the source, lens and observer will manifest itself as two moving images with time-variable magnifications (Fig. 5.2). The term “macrolensing” is used to describe the situation where the images can be resolved, and “microlensing” the situation where the images are not separately resolved, and only their joint variable magnified flux is observable. When the relative angular velocity \dot{y} between the source and lens is constant, the microlensing light-curve is given by substituting $y(t) = [y_0^2 + \dot{y}^2(t-t_0)^2]^{1/2}$ in Eq. (5.16), where y_0 is the angular impact parameter of the source trajectory relative to the lens and t_0 is the time of maximal magnification when $y=y_0$ (Fig. 5.2). Microlensing light-curves are distinguished from other astrophysical flares by their characteristic time-symmetric functional form and by their wavelength-independence, which is a consequence of the equivalence principle.

5.2.2 Gravitational lensing by the Galactic MBH

In order to plan the observational strategy for detecting gravitational lensing, or to estimate how likely it is that an observed flare is due to lensing, it is necessary to evaluate the detection probability. Two quantities are commonly used for this purpose, the optical depth and the lensing rate. The probability $P_L = 1 - \exp(-\tau_L)$ for finding at any given time a star lensed by the Galactic MBH is defined in terms of an optical depth $\tau_L = \int_{D_{OL}}^\infty n_\star \pi R_E^2 dD_{OS}$, which expresses the mean number of background sources within an angle θ_E of the line of sight to the MBH. Rough estimates predict $\tau_L \sim \mathcal{O}(1)$ (Alexander 2001; Alexander & Loeb 2001) for lensing by the MBH (assuming no limits on the photometric sensitivity).

The optical depth is a useful quantity in situations such as Galactic microlensing searches ($\tau_L \sim \mathcal{O}(10^{-6})$, e.g. Afonso et al. 2003), when there are many possible lensed lines of sights, and $\sim \tau_L^{-1} \sim 10^6$ background stars must be monitored simultaneously to find the rare one that is lensed by an intervening star. The observational situation for gravitational lensing by the MBH in the Galactic Center is different because the position of the lens is known and fixed, and so there is only one line of sight to monitor. The optical depth does not take into account the relative motions of the observer, lens and source, which reshuffle their random alignment and introduces a timescale to the problem. A more relevant quantity in this situation is the lensing rate Γ_L , which indicates how long it is necessary to monitor the GC on average to detect a lensing event with peak flux above a flux detection threshold F_0 ,

$$\Gamma_L(> F_0) \simeq \int_{D_{OL}}^\infty n_\star v_\perp \frac{2R_E}{A} dD_{OS}, \quad \text{for } A \geq \frac{F_0}{L_\star / 4\pi D_{OS}^2}, \quad (5.17)$$

where v_\perp is the velocity of the sources perpendicular to the line of sight relative to the optical axis, including the contribution from the reflex motion due to the observer, L_\star is the source luminosity and $A \gg 1$ is assumed. For practical applications, equation (5.17) has to be modified to take into account the range of stellar luminosities and velocities, dust extinction, the total duration of the observations T and the sampling rate ΔT (the mean duration of events amplified by more than A is $\bar{t}_L = \pi R_E / 2A v_\perp$; only events with $\Delta T < \bar{t}_L < T$ can be detected) (Alexander & Sternberg 1999).

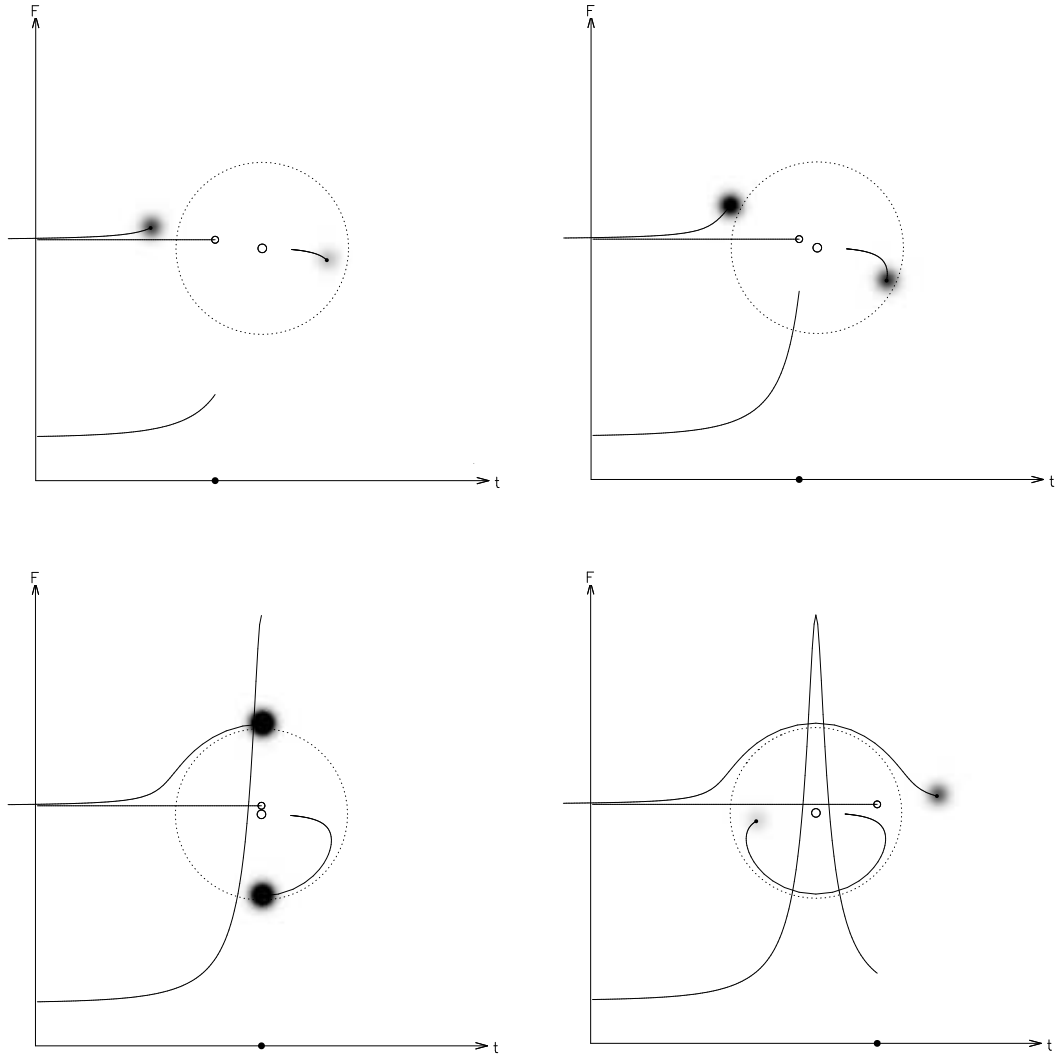


Figure 5.2: A time sequence (left to right, top to bottom) of a gravitational lensing event of a point source by a point mass. The two resolved images and their trajectories (fuzzy circles, whose size and shade are proportional to the flux, with curved lines tracking the image trajectories) are superimposed on a plot of the microlensing light-curve (total flux F from both images as function of time t in arbitrary units). Note that the tangential shear of the images is not shown here. The background source, which is not observed directly, (open circle with straight line tracking the source trajectory) moves in projection from left to right behind the MBH (open circle at center) with an impact parameter of $0.1\theta_E$. The two images move in tandem clockwise about the Einstein ring (large dotted circle). The strongly magnified image (top) is always outside the Einstein ring and is always brighter than the source. The weakly magnified image (bottom) is always inside the Einstein ring and can be strongly demagnified.

The observational limitations, F_0 , T and ΔT and the telescope's angular resolution $\delta\phi$, place restrictions on D_{LS} and the impact parameter for which sources can be detected, and affect the appearance of the lensing event, the typical timescales and the peak magnifications that are likely to be observed. The angular distance between the two images close to peak magnification is $\sim 2\theta_E$ (Eq. 5.14). A lensed star

will appear as a microlensing event if it is closer than D_μ behind the MBH,

$$D_\mu = \frac{R_0}{(\theta_\infty/\delta\phi)^2 - 1} \sim 0.2 \text{ pc} \left(\frac{R_0}{8 \text{ kpc}} \right) \left(\frac{\delta\phi/10 \text{ mas}}{\theta_\infty/2''} \right)^2. \quad (5.18)$$

Stars farther away will appear as two resolved images. The Einstein angle grows from zero to θ_∞ with source distance behind the MBH (Eq. 5.13), and so the lensing cross-section and the lensing duration (for a given $\max A$ and for constant v_\perp) also increase. In addition, high magnification events typically have longer time scales because the source trajectory must have a smaller impact parameter and so spends more time inside the Einstein radius. Therefore, observations with limited temporal sampling will tend to pick out high magnification events.

A couple of early detections of transient flaring events very close to Sgr A* (Genzel et al. 1997; Ghez et al. 1998) were considered as lensing event candidates. For one of these a light curve was recorded, but as it was under-sampled only estimates of a timescale (~ 1 yr) and a typical magnification ($\sim A > 5$) could be derived from it. The a-posteriori probability of detecting a lensing event (for the relevant observational limitations) was estimated to be only 0.5%, but on the other hand, the observed timescale and magnification were close to the expected median value (Alexander & Sternberg 1999). The interpretation of this event remains inconclusive. The likely alternative to lensing is that these were faint stars near the MBH that were observable only intermittently when they were well separated from the more luminous stars nearby. It should be noted that the K -band IR flares observed from Sgr A* have a typical timescale of $\mathcal{O}(1 \text{ hr})$ (although year-long variability is observed in longer IR wavelengths, Cl  net et al. 2004a). They are too frequent to be microlensing of near background stars and furthermore, their irregular light-curves and quasi-periodic oscillations are inconsistent with the time-symmetric microlensing light-curves (Genzel et al. 2003a).

Macrolensed image pairs, if hidden among the many stars observed around the MBH, can be used to pinpoint the MBH on the IR grid directly from the astrometric data, independently of other methods (§4.1) and with no assumptions about m , R_0 or the distribution of stars behind the MBH (Alexander 2001). The MBH lies on the line connecting the two images of any background source it gravitationally lenses (Fig. 5.2), and so the intersection of these lines fixes its position. The point-mass lensing equations (Eqs. 5.14, 5.16) imply simple relations between the fluxes of the two images, and between their angular positions and velocities and as measured relative to the projected position of the MBH,

$$-\theta_1/\theta_2 = -\dot{\theta}_{r,1}/\dot{\theta}_{r,2} = \dot{\theta}_{t,1}/\dot{\theta}_{t,2} = \sqrt{F_1/F_2}, \quad (5.19)$$

where $\dot{\theta}_{r,i}$ is the radial component of the projected angular velocity of image i ($i=1,2$), $\dot{\theta}_{t,i}$ is the tangential component and F_i the flux of the image. The simultaneous search for the position of the MBH and for lensed image pairs proceeds by enumerating over a grid of possible MBH positions. For each trial position, scores are assigned to all possible pairs of stars according to how well they satisfy Eq. (5.19). The MBH position is then chosen as the one maximizing the total lensing score, and the likeliest lensed image pair candidates can be recorded for spectroscopic validation (lensed image pairs should have exactly the same spectra, up to small deviations due to differences in the dust extinction along the two light paths). Such a search on an early astrometric data set produced a statistical detection of the MBH inside the error region on the center of acceleration (Fig. 4.3), with a chance detection probability of only 5×10^{-4} , where most of the signal came from the intersection of two pairs of lensed image candidates, tentatively identified as far background blue and red supergiants (simple models of the distribution of stars and dust in the far side of the Galaxy predict none within θ_E of the MBH). However, a subsequent recalibration of the data, and additional color information on the lensed image candidates

(Cl  net et al. 2004b), cast strong doubt on this result. This method has yet to be applied to the newer, more comprehensive and accurate astrometric data sets.

The MBH can modify the observed stellar surface density inside $\sim \theta_\infty$ (Wardle & Yusef-Zadeh 1992). A lens magnifies by enlarging the angular size of the unlensed sky behind it. Since surface brightness is conserved, the fluxes of sources are magnified by the same amount. If all the stars can be detected even without magnification, then the effect of lensing is to decrease the surface density of sources. However, if the magnification reveals faint stars, which could not be observed unlensed, then the observed surface density can be larger than the unlensed density if enough faint sources are magnified above the detection threshold to over-compensate for the decrease in surface density (“positive magnification bias”), or it could be smaller if the converse is true (“negative magnification bias”). The lensed luminosity function (stellar number surface density Σ per flux interval) is related to the unlensed one by

$$\left(\frac{d\Sigma}{dF} \right)_{\text{lensed}} \bigg|_F = A^{-2} \left(\frac{d\Sigma}{dF} \right)_{\text{unlensed}} \bigg|_{F/A}. \quad (5.20)$$

In many cases the luminosity function is well approximated by a power-law, $d\Sigma/dF \propto F^{-s}$ (§2.1). For $s=2$ the decrease in the total surface density is exactly balanced by the magnification of faint stars above the detection threshold. The chances for the detection of this effect in the Galactic Center appear small. A statistically meaningful detection requires a very high surface density that probably exceeds even that around the MBH (Wardle & Yusef-Zadeh 1992), and furthermore, models of the stellar luminosity function in the inner Galactic Center suggest that $s \sim 2$ (Alexander & Sternberg 1999).

Gravitational lensing will also affect the astrometric measurements of stars in the near vicinity of the MBH (Jaroszynski 1998a). The bright lensed image of a star on nearly edge-on orbits (within about $\pm 5^\circ$ of the line-of-sight to the MBH, as measured in a coordinate system centered on the MBH) will exhibit a small astrometric deviation of $\mathcal{O}(0.1 \text{ mas})$ in the Keplerian orbit as it passes behind the MBH (Nusser & Broadhurst 2004). The astrometric precision required to detect such a tiny effect is well beyond present-day capabilities. If measured by future telescopes, the form of the orbital deviation can distinguish between different dark mass distributions (§4.2) and be used to break the m/R_0^3 degeneracy of astrometric Keplerian orbits (§4.1.2).

5.2.3 Beyond the point lens approximation

The point mass lens model and the small deflection angle assumption provide a very useful approximation for describing gravitational lensing by the Galactic MBH. Nevertheless, there are several reasons to explore more complicated mass distributions and large angle lensing. First, it would be useful if gravitational lensing could be used to dispel any remaining doubts that the dark compact mass in the Galactic Center is indeed a MBH, and not some other extended distribution of matter (e.g. Capozziello & Iovane 1999; Nusser & Broadhurst 2004; §4.2). Unfortunately, it can be shown that the behavior of high-magnification light curves near peak magnification is universal and independent of the details of the lens (Schneider, Ehlers & Falco 1992, Eq. 11.21b). For spherically symmetric mass distributions this implies that the light curves differ only in the low magnification tails, which are much harder to observe. The astrometric effects of lensing may provide a more promising way to probe the dark matter distribution (§4.2). Second, large angle lensing probes GR in the strong field limit. GR corrections to the small angle approximation result in a variety of interesting effects (Virbhadra & Ellis 2000; Petters 2003; Bozza & Mancini 2004), such as “retrolensing”, where the Galactic MBH can redirect by $\theta \sim \pi$ the light from a close luminous *foreground* source (for example the star S2) back at the observer (De Paolis et al. 2003). However, these effects are minute and will be extremely hard to observe even by

the next generation of instruments. Third, the MBH is surrounded by a massive stellar cluster. Because the stellar mass is not smoothly distributed but is composed of discrete point masses, its effect on the lensing properties of the MBH is much larger than one may naively estimate by adding the stellar mass to that of the MBH (Alexander & Loeb 2001). Enhanced lensing by the presence of discrete stellar mass objects may be used to discover SBHs that have accumulated near the MBH due to mass segregation (Miralda-Escudé & Gould 2000; Chanamé, Gould & Miralda-Escudé 2001; §3.3).

The effect of stars on lensing by the MBH is similar to that of planets on microlensing by a star, a phenomenon that was studied extensively for the purpose of planet detection (e.g. Gould & Loeb 1992). The lensing cross-section of an isolated star is $\theta_E^2(M_*)/\theta_E^2(M_\bullet) = M_*/M_\bullet \lesssim 10^{-6}$ times smaller than that of the MBH (Eq. 5.12). However, when the star lies near $\theta_E(M_\bullet)$, the shear of the MBH distorts its lensing cross-section, which develops a complex topology, becomes radially elongated and is increased by up to an order of magnitude. As stars orbit the MBH, their elongated cross-sections scan the lens plane. If these happen to intersect one of the images of a background source that is lensed by the MBH, the image will be split into 2 or 4 sub-images whose angular separation will be of order $\theta_E(M_*)$, and so the sub-images will not be individually resolved. However, their combined flux will be significantly magnified. This will increase the probability of high magnification events over what is expected for lensing by the MBH alone. The light curves of such events will no longer be symmetric as they are for a point mass, but will exhibit a complex temporal structure, and their typical variability timescales will increase sharply for images that lie near $\theta_E(M_\bullet)$ because of the increased stellar cross-section for lensing. Enhanced lensing by stars in the Galactic Center is estimated to increase the probability of $A > 5$ lensing events by ~ 2 and of $A > 50$ events by ~ 3 (Alexander & Loeb 2001).

6 Strong star–MBH interactions

Some of the most spectacular stellar phenomena that can occur in the GC involve strong interactions with the MBH. In this context “strong” is defined as any interaction that cannot be described by Newtonian gravity operating on point masses. This could be because the stars’ internal degrees of freedom can no longer be ignored, or because dissipative interactions have to be included, or because GR effects must be taken into account.

Early interest in such processes focused on the consumption of stars by the MBH, either directly, when a whole star crosses the event horizon, or indirectly, when the gaseous debris left after the tidal disruption of a star is accreted by the MBH (Hills 1975; Frank & Rees 1976; Lightman & Shapiro 1977; Frank 1978; Rees 1988). The interest was driven by the implications for the growth of MBHs, for feeding luminous accretion in AGN and for detecting MBHs in quiescent galaxies by tidal disruption flares. However, tidal disruption is only one of several possible modes of interaction with the MBH. A useful analogy can be made between the MBH and the stars around it and an atomic nucleus and its surrounding electrons. In spite of the fundamental differences between a macroscopic classical system and a microscopic quantum one, the analogy to atomic processes suggests a classification scheme for the various modes of strong star–MBH interactions. This not only provides the “bookkeeping” needed to keep track of all the permutations, but also provides some analytical tools for calculating cross-sections, rates and branching ratios. The following atomic-like processes, and their possible observational signatures, are discussed here.

Annihilation Direct infall preceded by tidal disruption, where a substantial fraction of the stellar mass-energy is released (§6.1).

Absorption Direct infall where the stellar mass-energy is absorbed by the MBH (§6.1).

Deep inelastic scattering Tidal scattering, where the star is strongly perturbed by the MBH tidal field during a close “fly by”, but is not destroyed (§6.2.4).

Metastable decay vs collisional ionization / de-excitation Gradual orbital inspiral due to a dissipational force, such as gravitational wave emission or tidal heating, in the presence of orbital perturbations that can throw the star into the MBH or deflect it to a wide orbit (§6.2.1).

Charge exchange Three-body exchange where an incoming star knocks out one that is on a bound orbit to the MBH (the 3rd body) and replaces it (§7.2.4).

Ionization Three-body encounters where an incoming star eject a star tightly bound to the MBH into a wide, unbound orbit (§7.2.4).

6.1 Tidal disruption

The tidal interaction between a star and a black hole is characterized by three length-scales: the stellar radius R_* , the Schwarzschild radius r_S and the tidal radius r_t . The ratios of these length-scales can be expressed in terms of the ratios of the masses and escape velocities,

$$\begin{aligned} \frac{r_t}{R_*} &\sim \left(\frac{m}{M_*} \right)^{1/3}, \\ \frac{r_t}{r_S} &\sim \left(\frac{c}{V_e} \right)^2 \left(\frac{m}{M_*} \right)^{-2/3}, \\ \frac{r_S}{R_*} &= \left(\frac{c}{V_e} \right)^{-2} \left(\frac{m}{M_*} \right), \end{aligned} \quad (6.1)$$

where c , the speed of light, is the escape velocity from the BH and $V_e^2 = 2GM_*/R_*$ is the escape velocity from the stellar surface (for a solar type star $V_e \sim 600 \text{ km s}^{-1}$ and $(c/V_e)^2 \sim 2.5 \times 10^5$).

The nature and outcome of a “grazing collision” between a black hole and a star ($r_p \sim r_S + R_*$) depends on the relative magnitude of the black hole’s tidal field, the stellar self-gravity and its gas pressure and whether the disruption occurs in the Newtonian or GR limit (see discussion by Gomboc & Čadež 2005). By definition, the tidal energy extracted from the orbit and deposited in the star as it crosses the tidal disruption radius is of order of its binding energy, E_* . It also follows from the definition of r_t that the periastron crossing time at the tidal radius, τ_t , is of the order of the star’s dynamical timescale, since $\tau_t \sim \sqrt{r_t^3/Gm} = \sqrt{R_*^3/GM_*} = \tau_*$ ($\tau_* \sim 1600 \text{ s}$ for a solar type star). Therefore, *complete* tidal disruption occurs as fast or faster than the time it takes for the stellar gravity or gas pressure to react. These can therefore be neglected during the disruption and the particles composing the star approximately follow free-fall trajectories in the gravitational field of the black hole (Laguna et al. 1993; Kochanek 1994). This approximation holds until the stream of disrupted gas completes an orbit around the black hole and intersects itself. At that point strong shocks likely occur and the gas hydrodynamics have to be taken into account. When $r_p > r_t$, the tidal interaction is weaker and slower, lasting $\tau_p \sim \tau_t b^{3/2}$, where $b^{-1} \equiv r_t/r_p$ is the “penetration parameter”. It may then become longer than the stellar dynamical time scale to the extent that the stellar gravity and hydrodynamics do have to be taken into account. The ratio r_t/r_S determines whether the disruption occurs in the Newtonian limit ($r_t/r_S \gtrsim 10$) or in the GR limit ($r_t/r_S \lesssim \text{few}$).

The different regimes of tidal disruption can be classified by the mass ratio m/M_* and Eq. (6.1). In order of increasing m/M_* , these are

1. $m/M_* \ll 1$, which corresponds to $r_S \ll r_t \ll R_*$. In this case the tidal interaction is overall weak and Newtonian (only a small part of the star overlaps with the tidal disruption zone), and the process is dominated by the star’s gravity and pressure. The star is not disrupted. If the black

hole passes through the star it may accrete a small fraction of its mass. A more significant effect may occur if the black hole is captured inside the star and sinks to the center. This tidal regime could apply to the formation exotic stars that cannot be formed in the course of normal stellar evolution, such as Thorne-Żytkow objects (Thorne & Żytkow 1975), which are giant envelopes with an accreting compact object in their center.

2. $m/M_\star \sim 1$, which corresponds to $r_S \ll r_t \sim R_\star$. In this case a strong Newtonian interaction will occur, which would result in significant mass loss and possible disruption, depending on the central concentration of the stellar density profile. The process will be accompanied by strong shocks. This tidal regime applies to close interaction between a SBH and a massive star (e.g. the 3-body exchange scenario, §7.2.4).
3. $m/M_\star \sim (c/V_e)^2$, which corresponds to $R_\star \sim r_S < r_t$. In this case the disruption is complete and occurs in the Newtonian limit (the subsequent flow of the gaseous debris into the black hole is relativistic). This regime applies to disruption by intermediate mass black holes ($m \sim 10^3 - 10^4 M_\odot$), whose existence is still a matter of speculation (§1.3).
4. $(c/V_e)^2 < m/M_\star < (c/V_e)^3$, which corresponds to $R_\star \ll r_S < r_t$. Tidal disruption by the MBH in the GC falls in this regime ($r_t \sim 9r_S \sim 160R_\star$ for a solar type star). The disruption can be treated as Newtonian to a good approximation.
5. $m/M_\star > (c/V_e)^3$, which corresponds to $R_\star \ll r_t \ll r_S$. This is the case for a MBH with mass $\gtrsim 10^8 M_\odot$ (for solar type stars). The event horizon lies outside the (formal) tidal radius and the star falls into the MBH as a point particle on a General Relativistic trajectory without being significantly perturbed.

The various processes and phenomena associated with the tidal disruption of stars are reviewed by Rees (1988).

6.1.1 Tidal disruption rate

A star is tidally disrupted if the MBH mass is small enough so that $r_t > r_S$ and if its orbital angular momentum J is small enough so that $r_p \leq r_t$. Such orbits are called “loss-cone” orbits¹⁸ and in a spherical potential have

$$J^2 \leq J_{lc}^2(\varepsilon) \equiv 2r_t^2 (\psi(r_t) - \varepsilon) \simeq 2Gmr_t, \quad (6.2)$$

where the last approximate equality assumes that $r_t \ll r_h$ (the potential is dominated by the MBH) and $\varepsilon \ll \psi(r_t)$ (the star is consumed from a weakly bound orbit). In terms of Keplerian orbits (Eq. 3.15), which are a valid approximation inside r_h , tidal disruption requires that $r_p = a(1-e) \leq r_t$, that is either a very tightly bound orbit (small a , high ε) or a very eccentric one (high e , low J). The solid angle subtended by the loss cone is usually very small. The loss-cone’s opening angle for parabolic orbits is easily derived from angular momentum conservation (Frank & Rees 1976)

$$\vartheta_{lc}^2 \sim \frac{r_t}{a} = (1-e) \simeq \frac{1}{2} \left(\frac{J_{lc}}{J_c} \right)^2, \quad (6.3)$$

¹⁸The term “loss-cone” originates in plasma physics. For motion on a straight line (no gravity), the volume in velocity space that corresponds to disruption orbits originating from a point is a cone. With gravity’s effects included, it is actually a cylinder (Miralda-Escudé & Gould 2000).

where the typical radius is taken as $r \sim a$ and where

$$J_c^2 = Gma = (Gm)^2 / 2\varepsilon, \quad (6.4)$$

is the maximal (circular orbit) angular momentum for specific energy ε . For example, $\vartheta_{lc} \sim 10^{-3}$ for a solar mass star on a $a = 1$ pc orbit around a $3 \times 10^6 M_\odot$ MBH.

Loss-cone theory deals with the processes by which stars enter loss-cone orbits, the rate at which this occurs, and how these depend on the parameters of the system. This problem has been studied extensively over the years (Hills 1975; Frank & Rees 1976; Lightman & Shapiro 1977; Cohn & Kulsrud 1978; Magorrian & Tremaine 1999; Syer & Ulmer 1999; Alexander & Hopman 2003; Wang & Merritt 2004). While different approaches and assumptions lead to somewhat different quantitative results, the process is well understood qualitatively.

Any stars that are initially on loss-cone orbits are promptly destroyed on an orbital timescale once they reach periapse. From that time on, the tidal disruption rate, Γ_t , is set by the rate at which these orbits can be replenished by the relaxation processes that redistribute stars in phase space to high- ε or low- J orbits. Diffusion in ε -space occurs on the relaxation timescale, which roughly corresponds to the timescale for ε to change by order unity,

$$t_r \sim \varepsilon / \dot{\varepsilon}. \quad (6.5)$$

The relaxation time is approximately independent of energy in the GC (Eq. 3.7), and is assumed here to be also independent of J . Since t_r is also the timescale for J^2 to change by order J_c^2 (Eq. 6.4), the angular momentum relaxation timescale, which roughly corresponds to the timescale for J to change by order unity, is

$$t_J \sim J^2 / (\dot{J}^2) \sim [J/J_c(\varepsilon)]^2 t_r, \quad (6.6)$$

where the square root dependence of J on t_J reflects the random walk (diffusive) nature of the process¹⁹. Typically, $J_{lc} \ll J_c$. In principle, stars can enter the loss-cone, $J < J_{lc}(\varepsilon)$ either by a decrease in J , or by an increase in ε (up to the last stable orbit). In practice, diffusion in J -space is much faster: although $t_J \sim t_r$ when $J \sim J_c$, once J becomes smaller than J_c by order unity, $t_J \ll t_r$. Because J -diffusion is so much more efficient than ε -diffusion, only J -diffusion need be considered.

The way a star enters the loss-cone depends on $\Delta J(\varepsilon)$, the r.m.s change in $J(\varepsilon)$ over an orbital (dynamical) time $P(\varepsilon)$,

$$\Delta J(\varepsilon) \sim \sqrt{\frac{P(\varepsilon)}{t_r(\varepsilon)}} J_c(\varepsilon). \quad (6.7)$$

The ratio $\Delta J(\varepsilon)/J_{lc}$ defines two dynamical regimes of loss-cone re-population (Lightman & Shapiro 1977). In the “Diffusive regime” of stars with large ε (tight short-period orbits), $\Delta J(\varepsilon) \ll J_{lc}$ and so the stars slowly diffuse in J -space. The loss-cone remains nearly empty at all times since any star inside it is promptly destroyed. At $J \gg J_{lc}$ the DF is nearly unperturbed by the existence of the loss cone. In particular, it can remain very nearly spherically symmetric and depend only on ε (§3.2), but it falls logarithmically to zero at $J \gtrsim J_{lc}$. In the “full loss-cone regime” (sometimes also called the “pinhole” or “kick” regime) of stars with small ε (wide long-period orbits), $\Delta J(\varepsilon) \gg J_{lc}$ and so the stars can enter

¹⁹In fact, it is the velocity component perpendicular to the velocity vector, Δv_\perp , that executes a symmetric random walk, and not directly J itself. This introduces a drift term ($\propto t$) to the evolution of J , which is small compared to the diffusive term ($\propto \sqrt{t}$) as long as $t \lesssim t_J$ and can be neglected (Hopman & Alexander 2005).

and exit the loss-cone many times before reaching periapse. As a result, the DF is nearly isotropic at all $J \gtrsim J_{lc}$.

The tidal disruption flux density (stars disrupted per $d\epsilon$) in the diffusive regime, F_{dif} , is derived from the orbital diffusion coefficients for two-body scattering via the Fokker-Planck equation, with the boundary conditions that the stellar density fall to zero for $J \rightarrow J_{lc}$ and approach the isotropic distribution $n_{\text{iso}}(\epsilon)$ for $J \rightarrow J_c$ (Lightman & Shapiro 1977),

$$F_{\text{dif}}(\epsilon; J_{lc}) \sim \frac{n_{\text{iso}}(\epsilon)}{\ln[J_c(\epsilon)/J_{lc}(\epsilon)]t_r(\epsilon)}. \quad (6.8)$$

The diffusion flux is regulated mainly by the relaxation time and is only weakly dependent on the size of the loss-cone (typically $5 \lesssim \ln(J_c/J_{lc}) \lesssim 10$)²⁰. The logarithmic term reflects the fact that the diffusion occurs in a 2D space of solid angle (Lightman & Shapiro 1977). It can also be understood qualitatively by analogy to heat diffusion on the surface of a sphere from the equator (“ J_c ”), to a small hole at the pole (“ J_{lc} ”) (Frank & Rees 1976).

In the full loss-cone regime far from the MBH, where the DF is nearly isotropic, the tidal disruption flux density is simply $\propto \pi \vartheta_{lc}^2$. Since the loss-cone is refilled every orbital time, the flux density is

$$F_{\text{pin}}(\epsilon; J_{lc}) \sim \frac{J_{lc}^2(\epsilon)}{J_c^2(\epsilon)} \frac{n_{\text{iso}}(\epsilon)}{P(\epsilon)}. \quad (6.9)$$

The transition between the two regimes occurs at a critical energy ϵ_c (or equivalently a critical typical orbital radius r_c), where $F_{\text{dif}}(\epsilon_c) = F_{\text{pin}}(\epsilon_c)$, or approximately where $\Delta J(\epsilon) \sim J_{lc}$. The total tidal disruption rate is then given by

$$\Gamma_t \sim \int_0^{\epsilon_c} F_{\text{pin}}(\epsilon; J_{lc}) d\epsilon + \int_{\epsilon_c}^{\infty} F_{\text{dif}}(\epsilon; J_{lc}) d\epsilon. \quad (6.10)$$

An analysis of the behavior of the integrands in Eq. (6.10) for typical observed values of stellar cusp slopes, reveals that most of the contribution comes from the diffusive regime at values near $\epsilon_{\text{max}} \sim \max(\epsilon_c, \epsilon_h)$, where $\epsilon_h \sim \psi(r_h)$, or equivalently, near $r_{\text{max}} = \min(r_c, r_h)$ (Lightman & Shapiro ; Syer & Ulmer 1999; for numeric examples see Magorrian & Tremaine 1999). In most galaxies $r_c \lesssim r_h$ (Wang & Merritt 2004). Making use of this property, the tidal disruption rate can be approximated to within an order of magnitude by

$$\Gamma_t \sim \frac{N_*(< r_h)}{\ln(\sqrt{r_h/r_t})t_r(r_h)}. \quad (6.11)$$

Taking for the GC $r_h \sim 2$ pc, $r_t \sim 10^{13}$ cm, $N_*(< r_h) \sim m / \langle M_* \rangle \sim 3.5 \times 10^6$ and $t_r(r_h) \sim 4 \times 10^9$ yr (Eq. 3.8), the estimated rate is $\Gamma_t \sim 10^{-4} \text{ yr}^{-1}$, in agreement with more detailed calculations ($\Gamma_t \sim 5 \times 10^{-5} \text{ yr}^{-1}$, Syer & Ulmer 1999).

It should be noted that there are dynamical mechanisms that may increase the tidal disruption rate beyond that predicted by two-body scattering in a spherical system. The possibilities include the effects of massive perturbers, for example giant molecular clouds (Zhao, Haehnelt & Rees 2002), which indeed exist in the GC on scales of 1–2 pc from the MBH; enhanced rates due to resonant scattering (factor of ~ 2 rate increase; Rauch & Tremaine 1996; Rauch & Ingalls 1998); deviations from spherical symmetry (factor of ~ 2 rate increase; Magorrian & Tremaine 1999); or chaotic orbits in triaxial potentials (factor of 10–100 rate increase; Poon & Merritt 2002; Merritt & Poon 2004).

²⁰The diffusion timescale is longer than t_r by the logarithmic factor because the stellar phase-space density approaches zero near the loss-cone.

6.1.2 Tidal disruption and its aftermath

The observations of tidal disruption in the GC are realistically limited to those after-effects that persist for at least $\Gamma_t^{-1} \sim 10^4 \text{ yr}$ (the mean time between events). As described below, there are two main channels by which energy is released in a tidal disruption event: one is a luminous accretion flare lasting a few years, and the other, which is much less luminous but longer-lasting, is a shock wave, analogous to a supernova blast, that sweeps through the interstellar medium and can energize it substantially for $\sim 10^5 \text{ yr}$ (e.g. Khokhlov & Melia 1996). Observationally, the two effects complement each other. While tidal disruption flares may be, and perhaps were already observed in cosmological galaxy surveys (e.g. Komossa 2002), the supernova-like shock wave may be observed in the GC.

The hydrodynamics, radiative properties, early and late evolution of tidal disruption in the Newtonian and relativistic limits were studied extensively by numerous authors, both analytically (Rees 1988; Phinney 1989; Cannizzo, Lee & Goodman 1990; Kochanek 1994; Loeb & Ulmer 1997; Ulmer, Paczyński & Goodman 1998; Ulmer 1999; Menou & Quataert 2001; Ivanov & Novikov 2001; Ivanov, Chernyakova & Novikov 2002) and by simulations (Nolthenius & Katz 1982; Evans & Kochanek 1989; Khokhlov, Novikov & Pethick 1993; Frolov et al. 1994; Laguna et al. 1993; Diener et al. 1997; Ayal, Piran & Livio 2000; Bogdanović et al. 2004; Gomboc & Čadež 2005). While there is considerable uncertainty about details, a general picture has emerged.

It is useful to begin by considering the energy budget of a tidal disruption event. The star starts on a nearly parabolic orbit ($E_{\text{orb}} \simeq 0$) and so the total energy of the system (ignoring for now its rest-mass energy) is the stellar binding energy, $E_* < 0$. The outcome of tidal disruption is that some energy is extracted out of the orbit to unbind the star and accelerate the debris. Initially about $M_{\text{in}} \sim M_*/2$ of the stellar mass becomes tightly bound to the MBH with energy E_{in} , ($-E_{\text{in}} \gg |E_*|$), while the remainder $M_{\text{out}} \sim M_*/2$ of the stellar mass is forcefully ejected with energy E_{out} , ($+E_{\text{out}} \gg |E_*|$), so that $E_{\text{in}} + E_{\text{out}} = E_*$.

There are 3 distinct energy scales in the process, each associated with a different time scale. The lowest is the stellar binding energy E_* . By virtue of the virial theorem, the internal heat of the star is of order $U \sim -E_*/2$. During the disruption, on the periaapse passage timescale $\tau_p \sim \mathcal{O}(1 \text{ hr})$, the inner parts of the star are exposed as it is stretched and the heat can be radiated away. This may lead to a short flare immediately after disruption (Gomboc & Čadež 2005).

Next in scale is the kinetic energy of the ejecta. While the *mean* specific energy of the debris is $-E_*/M_* \sim V_*^2$ (V_* is the circular velocity on the stellar surface), the spread about this value can be orders of magnitude larger. As the star is disrupted, tidal torquing spins it up in the direction of the orbit, imparting an excess velocity $\gtrsim V_e = \sqrt{2}V_*$ above the mean orbital velocity $v_p \gg V_*$ to the stellar hemisphere on the far side from the MBH, and a comparable velocity deficit on the near side. The difference in velocities leads to a spread in the specific kinetic energies of about $(v_p + V_e)^2/2 - (v_p - V_e)^2/2 = 2^{3/2}v_p V_* \gg V_*^2$ (Rees 1988). The spread in energy can also be expressed in terms of the work done on the stellar debris by the tidal force (Lacy, Townes & Hollenbach 1982),

$$W \sim M_* \Delta\phi_{\text{MBH}}(r_p) \sim \frac{GmM_*}{r_p^2} R_* \sim -b^{-2} \left(\frac{m}{M_*} \right)^{1/3} E_* \gg -E_*, \quad (6.12)$$

where $\Delta\phi_{\text{MBH}}(r_p)$ is the MBH's gravitational potential difference across the star at periaapse. In a typical disruption event in the GC, $W \gtrsim 100E_*$ (for $b \sim 1$) and thus the debris is released with specific energies in the range $(E_* \pm W)/M_*$. Note that while $W \gg -E_*$, it is still much smaller than the orbital kinetic energy of the star at disruption, $-b^{-1}(m/M_*)^{2/3}E_*$. The kinetic energy carried by the ejected debris can significantly exceed that released by a normal supernova ($\sim 10^{51} \text{ erg}$) if the orbit is highly penetrating,

$$E_{\text{out}} \sim W \sim 4 \times 10^{52} \text{ erg} \left(\frac{M_*}{M_\odot} \right)^2 \left(\frac{R_*}{R_\odot} \right)^{-1} \left(\frac{m/M_*}{10^6} \right)^{1/3} \left(\frac{b}{0.1} \right)^{-2}. \quad (6.13)$$

Unlike a spherical supernova explosion, the mass will be ejected mostly in one half of the orbital plane (Khokhlov & Melia 1996).

The highest energy scale is that due to accretion onto the MBH. The bound debris will eventually circularize around the MBH after the stream of orbiting gas will cross itself, collide and shock. In order to fall into the MBH, the gas has to lose its angular momentum. If a mechanism exists that can exert torque on the rotating gas (for example shear due to effective viscosity mediated by magneto-hydrodynamic turbulence), it will gradually spiral inward on a viscous dissipation timescale. The gravitational binding energy of the gas to the MBH will be converted to heat, until it reaches the last stable circular orbit around the MBH ($3r_S$ for a Schwarzschild BH), where it will promptly fall into the event horizon on a dynamical timescale. If the gas can dissipate the heat by the emission of radiation, or acceleration of particles, then between $\eta=0.057$ (for a non-rotating BH) to $\eta=0.42$ (for a maximally spinning BH) of its rest mass energy can be extracted by the time it reaches the last stable orbit (e.g. Shapiro & Teukolsky 1983). If, on the other hand, energy dissipation is inefficient, the heat may be carried by the flow (advected) into the MBH and add to its rest mass (advection dominated accretion flow [ADAF] solution; Rees et al. 1982, Abramowicz et al. 1995; Narayan & Yi 1994, 1995; Narayan, Yi & Mahadevan 1995). Alternatively, the gas will not fall into the MBH but will escape as a wind (advection dominated inflow-outflow solutions [ADIOS], Blandford & Begelman 1999) or by convection outward (convection dominated accretion flow [CDAF], Quataert & Gruzinov 2000; Narayan, Igumenshchev & Abramowicz 2000). In the case of high radiative efficiency,

$$E_{\text{acc}} \sim \eta(M_*/2)c^2 \sim \eta b^2 \left(\frac{M_*}{m}\right)^{1/3} \left(\frac{c}{V_e}\right)^2 E_{\text{out}} > E_{\text{out}}. \quad (6.14)$$

Immediately after the disruption and acceleration at periaapse, the debris' self gravity and gas pressure are dynamically insignificant compared to its kinetic energy, and the gas streams follow ballistic (free falling) Keplerian orbits. The orbits are very eccentric $1-\langle e \rangle = r_p/a = 2b(M_*/m)^{2/3}$ with a large spread in orbital period and apoapse, extending from $P \rightarrow \infty$ ($r_a \rightarrow \infty$) of the barely bound gas, down to a minimal period P_{min} , ($r_a \simeq r_t(m/M_*)^{1/3}$), which corresponds to that of the most tightly bound gas with specific binding energy $b^{-2}(m/M_*)^{1/3}V_*^2$ (Eqs. 6.12, 3.15; Rees 1988; Evans & Kochanek 1989). The minimal period is

$$P_{\text{min}} = \frac{\pi}{\sqrt{2}} \sqrt{\frac{m}{M_*}} b^3 \tau_* \sim 0.1 \text{ yr} \left(\frac{m/M_*}{10^6}\right)^{1/2} \left(\frac{R_*}{R_\odot}\right)^{3/2} \left(\frac{M_*}{M_\odot}\right)^{-1/2} b^3. \quad (6.15)$$

After an initial delay of P_{min} the debris will start returning to the point of disruption at a rate $\dot{M} = (dM/dE)(dE/dP)$. Simulations show that the spread in energy of the bound debris is nearly uniform, $dM/dE \simeq \text{const}$ (e.g. Evans & Kochanek 1989; Ayal, Piran & Livio 2000), and so (Eq. 3.15)

$$\dot{M}_{\text{in}}(t) \simeq \frac{M_*}{3P_{\text{min}}} \left(\frac{t}{P_{\text{min}}}\right)^{-5/3}, \quad (t > P_{\text{min}}). \quad (6.16)$$

When $r_p \gtrsim r_S$, GR correction have to be taken into account. These lead to a stronger tidal interaction, and consequently a higher spread in energies (Eq. 6.12), a shorter P_{min} and larger peak debris return rate (Ulmer 1999).

Initially, the mass return rate exceeds the Eddington-limited accretion rate²¹

$$\max \dot{M} = \frac{\dot{M}_{\text{Edd}}}{\eta} \simeq 0.03 \left(\frac{m}{10^6 M_{\odot}} \right) \left(\frac{\eta}{0.1} \right)^{-1} M_{\odot} \text{yr}^{-1}. \quad (6.17)$$

In the GC, $\max \dot{M} \sim 0.1 M_{\odot} \text{yr}^{-1}$. The return rate remains higher than the Eddington-limited rate for no more than a few years,

$$t_{\text{in}} = \left(\frac{\pi}{3\sqrt{6}} \right)^{2/5} \eta^{3/5} b^{6/5} \left(\frac{M_{\star}}{m} \right)^{2/5} \left(\frac{\tau_{\star}}{\tau_{\text{Edd}}} \right)^{2/5} \tau_{\text{Edd}} = 4 \left(\frac{\eta}{0.1} \right)^{3/5} b^{6/5} \left(\frac{m/M_{\star}}{10^6} \right)^{-2/5} \left(\frac{\tau_{\star}}{10^4 \text{s}} \right)^{2/5} \text{yr}, \quad (6.18)$$

where $\tau_{\text{Edd}} \equiv m/\dot{M}_{\text{Edd}}$ is the e -folding timescale of Eddington accretion with unit efficiency. A similar estimate is obtained by considering the time for accretion of all the debris at the Eddington-limited rate if all the mass returned at once, $t_{\text{Edd}} \sim M_{\text{in}}/\max \dot{M} \sim 5 \text{yr}$. The high initial mass return rate does not necessarily imply an early phase of Eddington-limited accretion. In order for the disruption event to produce a luminous flare, both the time for circularization, which sets the flow pattern required for dissipation, and the timescale for viscous dissipation, which extracts the angular momentum, have to be short enough so as not to be an impediment to the accretion. This indeed appears to be the case.

Circularization is expected to be efficient. The evolution of the bound debris is driven by shocks between streams of gas that converge to their common point of origin at periaapse. Relativistic precession (Eq. 5.6) will also lead to shocks between incoming and outgoing streams. These shocks will redistribute angular momentum and energy between the gas streams. Some fraction of the initially bound debris will become unbound after undergoing strong shocks and heating on the second periaapse crossing, leaving perhaps $\sim M_{\star}/4$ of the gas bound to the MBH (Ayal, Piran & Livio 2000). While the exact details are uncertain, it is expected that circularization will occur rapidly, on a timescale of $t_{\text{circ}} \sim \text{few} \times P_{\text{min}}$ (Ulmer 1999).

The viscous accretion timescale at the tidal radius is $t_{\text{acc}} \sim 2\pi\tau_t/\alpha\pi h^2 = 3 \times 10^{-4} (\tau_{\star}/\tau_{\star,\odot})/\alpha\pi h^2 \text{yr}$, where α is the dimensionless viscosity parameter (the proportionality factor between the viscous stress tensor and the pressure) and h is the ratio of the thickness of the accretion disk to its radius ($h \sim 1$ for a thick disk). When $\dot{M} \gtrsim \dot{M}_{\text{Edd}}$, the radiation pressure puffs up the disk ($h \rightarrow 1$) and decreases t_{acc} . The value of α is uncertain, but $10^{-3} \lesssim \alpha \lesssim 10^{-1}$ seems plausible²² (Ulmer 1999), so that probably $t_{\text{acc}} \lesssim 0.01 \text{yr}$. It then follows that $t_{\text{acc}} < t_{\text{circ}} < t_{\text{Edd}}$, which means that for the first few years after a disruption event the accretion will probably proceed at a super-Eddington rate ($L \sim L_{\text{Edd}}$, small η , $\dot{M} > \dot{M}_{\text{Edd}}$) with a radiatively inefficient accretion flow, such as ADAF, ADIOS and/or CDAF (Rees 1988; Menou & Quataert 2001).

Most of the work on the observational signature of tidal disruption concentrated on “tidal flares”, which correspond to this initial luminous phase, lasting months to years. Tidal flares are expected to peak in the UV/X-ray range, as can be estimated by assuming that the Eddington luminosity is emitted

²¹The luminosity released by matter accreting on a mass m exerts an outward radiation pressure on the infalling mass. The radiation pressure balances gravity and halts the accretion when the luminosity reaches the Eddington luminosity, $L_{\text{Edd}} = 1.5 \times 10^{38} (m/M_{\odot}) \text{erg s}^{-1}$ (for isotropic luminosity and pressure due to Thomson scattering). The Eddington accretion rate $\dot{M}_{\text{Edd}} \equiv L_{\text{Edd}}/c^2 = 3 \times 10^{-9} (m/M_{\odot}) M_{\odot} \text{yr}^{-1}$ is defined as the maximal possible for unit efficiency. The actual Eddington-limited accretion rate is $\max \dot{M} = \dot{M}_{\text{Edd}}/\eta$.

²²Alternatively, if $10^{-5} \lesssim \alpha \lesssim 10^{-3}$ and $\eta \gtrsim \text{few} \times 0.01$, the configuration may be analogous to a Thorne-Żytkow object, in the form of a large ($\sim 100r_t$) optically thick star-like object with $T_{\star} \sim 10^4 \text{K}$, powered by accretion. Such an object will emit at the Eddington limit mainly in the optical (Loeb & Ulmer 1997), unlike the UV/X-ray flares discussed here.

as blackbody radiation from a surface whose typical size probably lies between the last stable orbit and the tidal radius. The blackbody temperature is then $T_{\text{bb}} = (L_{\text{Edd}}/4\pi r^2 \sigma_{\text{SB}})^{1/4}$, and

$$T_{\text{bb}}(r_t) \sim 3 \times 10^5 \left(\frac{m}{10^6 M_{\odot}} \right)^{1/12} \text{ K}, \quad \text{or} \quad T_{\text{bb}}(3r_S) \sim 7 \times 10^5 \left(\frac{m}{10^6 M_{\odot}} \right)^{-1/4} \text{ K}, \quad (6.19)$$

(Assuming a solar-type star for r_t), almost independently of the MBH mass. This temperature corresponds to a blackbody peak at ~ 0.1 keV.

There are a few tentative detections of tidal flares in other galaxies (see review by Komossa 2002). However, the short duration of the flare and the mean time between tidal disruption events in the GC (§6.1.1) translate to a very low duty cycle of $\sim 10^{-4}$. The probability of directly observing a tidal flare in the Galaxy is small.

A few years after the tidal disruption event, when the return rate drops below the Eddington rate, the gas will cool efficiently and accrete via a radiatively efficient, geometrically thin accretion disk, at a rate set by the viscous timescale. The accretion rate in the thin disk is expected to fall off slowly with time (Cannizzo et al. 1990). However, this result is at odds with observations. The predicted average luminosity due to accretion of debris from a past tidal disruption event is 2–4 orders of magnitude higher than that observed in the GC, or in the centers of nearby galaxies M31 and M32 (Menou & Quataert 2001; §6.2.5). This discrepancy has been interpreted as indicating that most of the debris was blown away during the early super-Eddington accretion phase. Following that, the luminous accretion phase shuts off early, either because the low-mass accretion disk spontaneously switches over to a low radiative efficiency solution when $\dot{M} \lesssim 10^{-2} \dot{M}_{\text{Edd}}$, or else because increasingly larger parts of the cold outer disk become neutral, unable to sustain magneto-hydrodynamic turbulence and therefore effectively inviscid (Menou & Quataert 2001).

6.1.3 Signatures of tidal disruption

While there is as yet no clear evidence of tidal disruption in the GC, there are several ideas about the form such evidence could take.

The ejection of tidal debris with energies that far exceed those released in normal supernovae could provide a long-term signature of tidal disruption, in the form of unusual supernova remnant-like structures. This was suggested as the origin of the Sgr A East radio source (Khokhlov & Melia 1996). Sgr A East is a prominent non-thermal radio continuum source with an elongated shell-like structure extending over 10–20 pc, offset from Sgr A*, but engulfing it at the edge of the structure (e.g. Yusef-Zadeh & Morris 1987). The shell structure and the non-thermal spectrum are reminiscent of a supernova remnant. Early estimates of the energy required to evacuate the radio-emitting cavity inside the dense surrounding molecular clouds yielded an extreme lower bound of $E > 4 \times 10^{52}$ erg (Mezger et al. 1989). The high energy requirement, large size and non-spherical shape are in line with what is expected from a deep tidal disruption event. However, more recent estimates of the energy from X-ray observations (Maeda et al. 2002; Sakano et al. 2004) yield a much lower value, which together with the metal-rich abundances observed in Sgr A East, are consistent with the energy and elemental output of a single normal core collapse supernova (but see §6.1.4 about the possibility of nucleosynthesis during a tidal detonation of a low mass star). The single supernova interpretation is also supported by observations of molecular transitions, which allow an estimate of the kinetic energy in molecular gas that is being swept by the expansion of Sgr A East (Herrnstein & Ho 2005).

A tidal disruption event is expected to produce a short luminous UV/X-ray accretion flare (§6.1.2), which will likely also have a hard X-ray component, as is seen from accreting MBHs in AGN. These primary X-ray photons will encounter gas clouds as they propagate from the MBH, and will be Thomson-scattered into the line-of-sight or absorbed and re-emitted as fluorescence lines, primarily in the 6.4 keV

$K\alpha$ line from neutral Iron (“X-ray reflection nebula”). The reflected photons arriving at the observer at any given time were scattered (or re-emitted) from a parabolic surface around the MBH. Reflected X-ray emission is not an exclusive signature of tidal disruption. There could well be other causes for episodic accretion flares or short high-state epochs. However, the spatial distribution and temporal changes in the scattered X-ray continuum photons and the emission lines can at least provide information on the position of the source and the time and duration of the flare, as the paraboloid of equal arrival time sweeps the volume around the MBH at the speed of light (Sunyaev & Churazov 1998). The X-ray reflection effect could effectively lengthen by ~ 2 orders of magnitude the time available for detecting an accretion flare. However, even if the distribution of gas clouds extends far from the center, it is unlikely that the fluorescence could be detected as long as $\Gamma_t^{-1} \sim 10^4$ yr years after the tidal disruption event ($\lesssim 1$ kpc from the center) due the geometrical dilution of the primary X-ray flux with distance.

The present observed level of diffuse X-ray emission from the central ~ 700 lyr of the GC was used to argue that Sgr A* has not radiated at the Eddington level for even a day in the last 400 yr (Sunyaev, Markevitch & Pavlinsky 1993). The detected 6.4 keV line emission from several sites near the GC (Koyama et al. 1996; Murakami et al. 2000, 2001) was found to be well reproduced by an X-ray reflection nebula model. The luminosity required to reproduce the 6.4 keV line exceeds by 3 orders of magnitude any observed X-ray point source in the region, and by 6 orders of magnitude the present average X-ray luminosity of Sgr A* (Baganoff et al. 2001; Goldwurm et al. 2003). This was taken as evidence that Sgr A* was active > 300 yr ago. The detection of high energy X-rays (≤ 200 keV) from a giant molecular cloud further supports this interpretation (Revnivtsev et al. 2004). The reconstructed X-ray luminosity and hard X-ray spectrum slope are characteristic of low-luminosity AGN, and suggest that Sgr A* was active for at least 10 yr some 300–400 years ago. However, recent X-ray observations with high spectral resolution (Predehl et al. 2003) do not support this interpretation, due to the absence of a strong 7.1 keV absorption edge that is expected to accompany the 6.4 keV emission line in X-ray reflection nebulae, and due to the lack of the expected inverse correlation between the 6.4 keV line surface brightness and distance from the center.

Another possible long-term after-effect of a strong tidal encounter is tidal stripping, the partial disruption of evolved giants (Davies & King 2005). Evolved giant stars have an extended, cool, low density envelope and a hot, massive compact core. Because of its low surface gravity, the envelope can be stripped off the core even at large periaapse distances where denser main-sequence stars are safe. The bare core, while no longer burning, will likely remain hot ($T > 10^5$ K) and luminous ($L > 10^2 L_\odot$) for 10^3 – 10^6 yr after the tidal stripping event. The hot core will appear as a “supersoft X-ray source”, which can be detected in the GC and in the centers of other nearby galaxies (Di Stefano et al. 2001). The challenge lies in distinguishing tidally stripped cores from normal young hot white dwarfs and the He cores of massive stars that lost their envelopes by strong winds or by interactions with a binary companion. In addition, Collisional stripping (§3.4.1) is expected to produce a similar effect.

6.1.4 Tidal detonation

When a disrupted star crosses deep inside the tidal radius, $b^{-1} \gtrsim 5$, it experiences a very strong and rapid tidal compression during periaapse passage. Figure (6.1) shows a qualitative demonstration of the effect by a simple (low-resolution Newtonian) Smoothed Particle Hydrodynamics (SPH) simulation²³. The

²³SPH is an algorithm for simulating the hydrodynamics of 3D self-gravitating fluids, which is commonly used in the study of stellar collisions (Lucy 1977; Gingold & Monaghan 1977; see review by Monaghan 1992). The star is represented by discrete spherical mass elements, each with an internal density distribution that peaks in the center and falls to zero at the edge. The total density at a point is the sum of densities in all overlapping spheres that include the point. The resulting density field is continuous and differentiable, and so its thermodynamic properties can be evaluated everywhere once an equation of state is specified. Every time step, the positions of the mass elements are updated according to the gravitational force and the pressure gradient, and the sphere sizes

compression occurs perpendicular to the orbital plane and it more than compensates for the stretching of the star along the orbit, resulting in a rapid increase in the central density. This happens despite the fact that the tidal force tensor is traceless (i.e. the force lines do not converge)—Both the inward- and outward-directed tidally induced velocities relative to the star’s center, $V_t \sim R_*/\tau_p$, are of the same order of magnitude. However, expansion along one dimension leads to a relative increase in that dimension of only order unity, whereas collapse in another dimension leads to an arbitrarily large relative decrease in that dimension, so the net effect is a vanishing volume with diverging central density (i.e., on the periaapse passage timescale τ_p the volume shrinks roughly as $R_*^3 \rightarrow R_*(R_* + V_t\tau_p)(R_* - V_t\tau_p) \rightarrow 0$). An order of magnitude estimate indicates that the maximal central compression ratio can be as high as $\max \rho_c/\rho_c \sim b^{-3}$, where ρ_c is the initial stellar central density. This upper limit is derived by assuming the full conversion of the kinetic energy of the adiabatically collapsing stellar ellipsoids into internal heat (Carter & Luminet 1983). The actual compression ratio that can be achieved, and its ultimate consequences depend on the uncertain details of the response of the gas hydrodynamics and geometry to the sudden compression via increased nuclear energy production and shocks. Simulations indicate that the maximal compression ratio is significantly smaller than the kinematic upper limit (Luminet & Marck 1985; Khokhlov, Novikov & Pethick 1993), but still very high, $\max \rho_c/\rho_c \sim b^{-1.5} - b^{-2}$ (Bicknell & Gingold 1983; Laguna et al. 1993).

It has been suggested that such a strong tidal compression could lead to a ignition of nuclear reactions and the sudden release of energy, thereby producing a supernova-like explosion and an energetic outflow of metal-enriched stellar debris (Carter & Luminet 1982; 1983; Carter 1992). The nuclear energy produced during the compression is $E_{\text{nuc}} \sim Q\tau_p$, where Q is the nuclear power. The nuclear power from a tidally compressed burning core scales very roughly as $Q \sim L_*(\rho_c/\rho_*)^k (T_c/T_*)^n$, where L_* , ρ_* and T_* are the initial equilibrium luminosity, central stellar density and temperature. For hydrogen burning, $k=1$, $n \sim 4$ for the p - p chain and $n \sim 16$ for the CNO cycle; for helium burning (triple- α), $k=2$ and $n \sim 40$. As a crude estimate, consider a simplified scenario where the compressed stellar core continues burning by the same nuclear process, but with scaled-up power. Assuming adiabatic contraction of an ideal gas (i.e. neglecting nuclear burning during the contraction), with $P \propto \rho^\gamma$ and $T \propto \rho^{\gamma-1}$ for $\gamma=5/3$, including the scaling of the periaapse passage time, $\tau_p \sim \tau_* b^{3/2}$, and parameterizing $\max \rho_c/\rho_c \sim b^{-u}$ ($u=3/2$ will be assumed below), the nuclear energy produced varies with b as

$$E_{\text{nuc}} \sim \tau_* L_* b^{-s}, \quad s \equiv u[k+n(\gamma-1)]-3/2. \quad (6.20)$$

For a solar type star (p - p burning, $E_* \sim 4 \times 10^{48}$ erg and $\tau_* = 1600$ sec, $s=10$), the energy produced is negligible, $E_{\text{nuc}}/E_* \sim 2 \times 10^{-12} b^{-10} \ll 1$, as long as $b^{-1} < 13$. The p - p chain is too slow to be an important source of energy during the brief tidal compression. However, for a $10M_\odot$ main sequence star, such as are observed near the Galactic MBH (CNO cycle burning, $E_* \sim 8 \times 10^{49}$ erg, $\tau_* \sim 4800$ sec and $L_* \sim 6 \times 10^3 L_\odot$, $s=16$), $E/E_* \sim 10^{-9} b^{-16} \sim 1$ even for a moderate penetration parameter of $b^{-1} \sim 3.6$. CNO cycle burning accelerated by the tidal compression will cause the star to explode while it is being disrupted. A helium burning giant, where $E_{\text{nuc}} \propto b^{-41.5}$, will be even more susceptible to tidal detonation.

Since the cross-section for a close encounter with the MBH with periaapse $\leq r_p$ scales as r_p (§6.2), tidal detonation events are expected to occur at an even smaller rate than that of tidal disruption events, $\Gamma_d \simeq \Gamma_t b \lesssim 10^{-5}$ yr (§6.1.1), and so it is not likely that such an event will be observed in the GC in real time. Moreover, the tidal detonation is energetically negligible compared to the kinetic energy that is transferred to the debris by the tidal field from the stellar orbital energy (§6.1.2). However, tidal detonation can affect the aftermath of a tidal disruption event more subtly. By increasing the velocity at which debris is expelled relative to its center of mass along the orbital plane, it can modify the properties

are readjusted to reflect the changes in the local space density of elements.

of the subsequent accretion on the MBH by making the bound matter more tightly bound and strongly relativistic. An additional effect of “pancake detonation” is to modify the chemical composition of the interstellar medium around the MBH. Pichon (1985) finds that nucleosynthesis by pancake detonation leads to the synthesis of proton-enriched isotopes, in contrast with core-collapse supernovae, which synthesize neutron-enriched isotopes. Unusual nucleosynthesis may also be associated with a related process, the tidal detonation of a WD caused by a combination of tidal compression and enhanced self-gravity due to GR terms. The compression can lead to pyconuclear reactions and a thermonuclear runaway under highly degenerate conditions, even when the WD mass is well below the Chandrasekhar mass (Wilson & Mathews 2004).

6.2 Dissipative interactions with the MBH

A star whose orbit passes just outside the tidal disruption radius, or the event horizon if $r_S > r_t$, will survive the close encounter with the MBH. Such “near misses” often involve some orbital energy loss, ΔE , for example by the emission of GW (when $r_S < r_p \lesssim \text{few} \times r_S$) or by the work invested in raising stellar tides and exciting stellar oscillations (when $r_t < r_p \lesssim \text{few} \times r_t$). If the star maintains its nearly radial trajectory for many orbital periods, the dissipational energy losses will gradually accumulate and cause the orbit to shrink and the star to spiral in. This will continue until either the dissipation shuts off, or the star is destroyed by the MBH, or is disrupted by the dissipational energy. An initial close encounter with the MBH is in itself not enough to guarantee that the star will reach the final stages of inspiral. The inspiral timescale is usually orders of magnitude longer than the orbital timescale. During that time the star is vulnerable to the same scattering process that deflected it into the low- J orbit in the first place. It can be scattered again to an orbit with a larger periaapse, where dissipation is inefficient, or to a loss-cone orbit where it is promptly destroyed. Thus the probability for completing inspiral is small, and the rate of inspiral events is much smaller than that of direct infall events (§6.2.1). In the GC $r_t > r_S$, and most stars that undergo a non-disruptive close tidal encounter with the MBH are subsequently scattered to a wide orbit and survive after experiencing an extreme tidal distortion, spin-up, mixing and mass-loss that may affect their evolution and appearance. Such “tidally scattered” stars eventually comprise a few percents of the stellar population within the MBH radius of influence (§6.2.4).

If the inspiraling star avoids being scattered to a wider orbit or falling directly into the MBH, its orbital period P will decrease every peri-passage and the mean dissipated power, $\sim \Delta E/P$, will increase. If the emitted power grows high enough, it may have observed in the form of GW emission (§6.2.2), or high tidal luminosity (§6.2.3). A different class of mechanisms for orbital energy dissipation (not relevant for the present-day GC) is by drag against a massive accretion disk, if one is present (§6.2.5). This may play a role in feeding stars to MBHs.

6.2.1 Orbital inspiral into the MBH

Inspiral can be treated as an extension of loss-cone theory. The inspiral problem was studied in the context of GW emission from compact objects orbiting a MBH (Hills & Bender 1995; Freitag 2001; Sigurdsson & Rees 1997; Sigurdsson 1997; Ivanov 2002; see review by Sigurdsson 2003; Hopman & Alexander 2005), and was generalized to arbitrary dissipation mechanisms and applied to tidal capture by Alexander & Hopman (2003) and Hopman, Portegies-Zwart & Alexander (2004).

Inspiral processes are characterized by an inspiral timescale, $t_0(\varepsilon_0, J_0)$, which is the time needed for a star starting at an orbit with initial energy ε_0 and angular momentum J_0 to complete the inspiral ($\varepsilon \rightarrow \infty$, $P \rightarrow 0$). The dissipated specific energy per orbit, $\Delta \varepsilon$, typically increases sharply as r_p is decreased and correspondingly t_0 decreases sharply with r_p (Eq. 6.29). Over the range of interest the inspiral time satisfies $P \ll t_0 \ll t_r$ (when $P \lesssim t_0$, r_p is so small that the inspiral is indistinguishable from direct

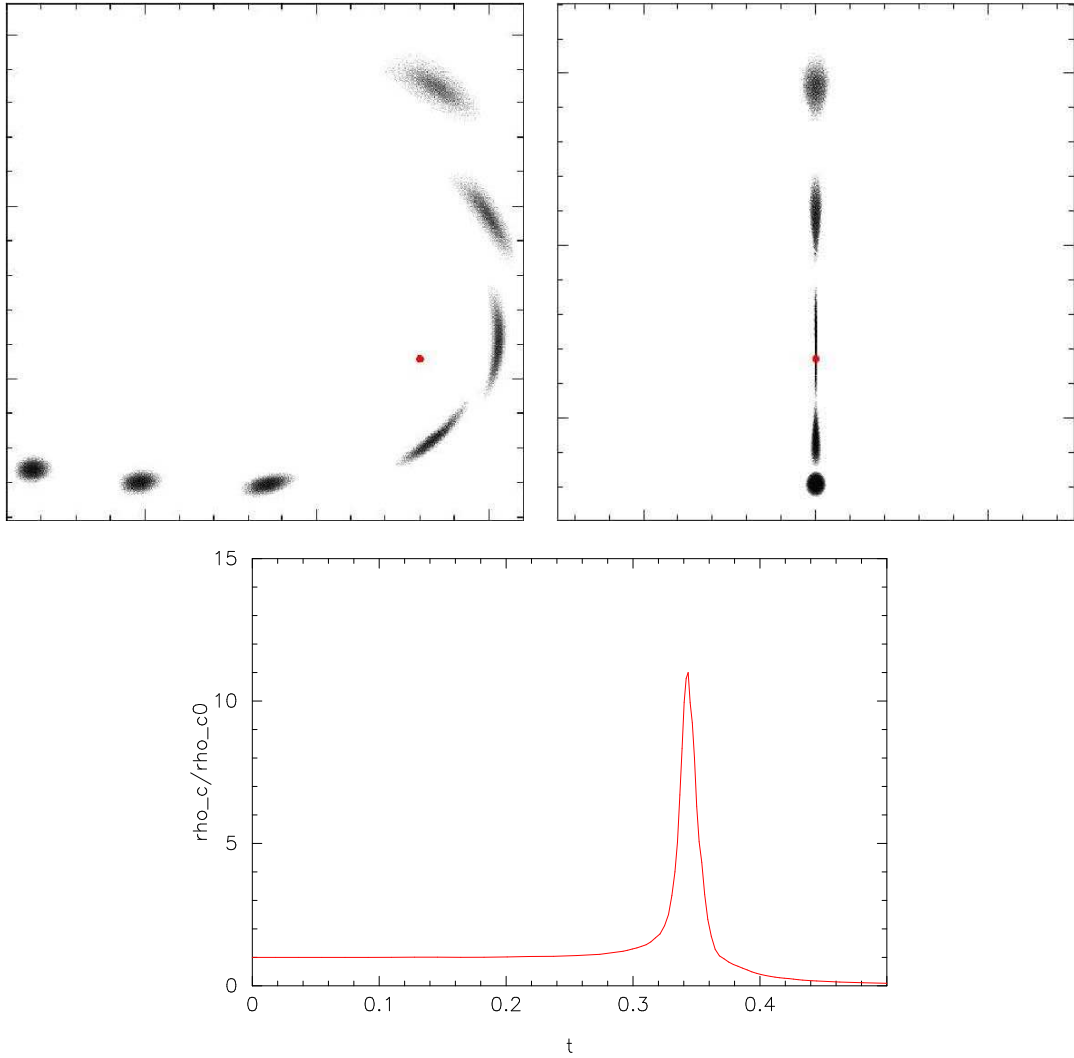


Figure 6.1: A sequence of snapshots from an SPH simulation of a $M_\star = 10 M_\odot$, $R_\star = 4.5 R_\odot$ star (represented by an $n = 1.5$ ideal gas polytrope) being disrupted by a very close passage to a $3 \times 10^6 M_\odot$ MBH on a parabolic orbit with $r_p = 4 R_\star = 0.06 r_t = 1.4 r_S$. The simulation assumes Newtonian gravity and neglects nuclear burning, and so while the results are qualitatively correct, they are quantitatively inaccurate: GR effects analogous to periape shift, omitted here, will actually cause the expanding debris in penetrating encounters ($b^{-1} \gg 1$) to fan out in a thin crescent-like shape centred on the MBH (Laguna et al. 1993). Top left: face-on view of the star as it orbits (counter clockwise) the MBH (dot at bottom right corner). Top right: edge-on view of the same orbit (the two left-most snapshots shown in the face-on view are omitted from the edge-on view, for clarity). Bottom: time evolution of the central density. Time is measured in terms of the star’s dynamical time $\tau_\star = 4840$ s. Note the strong and rapid tidal compression at periape (a density increase by a factor of 11 on a timescale of ~ 100 s).

infall. Conversely, when $t_0 \lesssim t_r$, r_p is so large that dissipation is negligible). The condition $t_0 \ll t_r$ also implies that ε -diffusion by scattering is negligible during the inspiral. The same is not generally true for J -diffusion. However, when the initial inspiral time is also much shorter than the angular momentum

relaxation timescale (Eq. 6.6),

$$t_0(\varepsilon_0, J_0) \ll t_J(\varepsilon_0, J_0), \quad (6.21)$$

then the inspiral is completed with $J \sim J_0$ nearly constant. When Eq. (6.21) is satisfied the star decouples from the random perturbations that governed its dynamics in the initial scattering-dominated phase, and it enters the final dissipation-dominated phase where its orbit is deterministic and governed by the MBH potential and the dissipation mechanism only.

It is not necessary to specify J_0 to obtain a *statistical* description of t_0 . The mean inspiral time \bar{t}_0 of stars that complete the inspiral is effectively a function of ε_0 only because as long as $t_J < t_0 < t_r$, J -diffusion by scattering will continue until such time when J satisfies $t_0 \ll t_J$. Thus, the requirement of successful inspiral, together with the dynamics of random walk in J -space in the presence of dissipation, define a mean value of angular momentum in the inspiral phase, $\bar{J}_0(\varepsilon_0)$. The value of \bar{J}_0 and the distribution of J_0 around it can be calculated once the specific properties of the stellar system and the dissipation mechanism are given (Hopman & Alexander 2005).

In analogy to the case of direct disruption, Eq. (6.21) sets a lower limit, ε_c , on the initial energy (or an upper limit, r_c , on the initial orbital radius) that is required for completing inspiral. Stars with $\varepsilon_0 > \varepsilon_c$ (the diffusive regime) will typically complete inspiral, whereas stars with $\varepsilon_0 < \varepsilon_c$ will be typically scattered to high- J or loss-cone orbits and therefore have a vanishingly small chance of completing inspiral. Because $t_0 \gg P$, the phase-space volume available for the diffusive regime of inspiral is much smaller than that of direct infall ($\varepsilon_c^{\text{inspiral}} \gg \varepsilon_c^{\text{infall}}$, $r_c^{\text{inspiral}} \ll r_c^{\text{infall}}$) and consequently the inspiral rate is generally much smaller than that of direct infall. Inspiral can be likened to a race between scattering and dissipation, in which dissipation can win only if the track is short.

It is sometimes the case that the energy dissipated per orbit, $\Delta\varepsilon$, is constant over the course of the inspiral to a good approximation (for example when $\Delta\varepsilon$ depends mainly on the periaapse distance, which remains nearly fixed when $t_0 \ll t_J$ and when the dissipated angular momentum ΔJ is small). In that case, the inspiral timescale in a Keplerian potential, \hat{t}_0 (calculated relative to a given time based on the values of $\Delta\varepsilon$, ε_0 and P_0 at that time), is

$$\hat{t}_0 = \frac{1}{\Delta\varepsilon} \int_{\varepsilon_0}^{\infty} P(\varepsilon) d\varepsilon = 2 \frac{\varepsilon_0 P_0}{\Delta\varepsilon} \propto \frac{1}{\varepsilon_0^{1/2} \Delta\varepsilon}, \quad (6.22)$$

and the period and the semi-major axis evolve simply as

$$P = P_0(1 - t/\hat{t}_0)^3, \quad a = a_0(1 - t/\hat{t}_0)^2. \quad (6.23)$$

The number of inspiral orbits by time $t < \hat{t}_0$ is then given by

$$N_{\text{orb}} = \frac{\hat{t}_0}{2P_0} \left[\left(1 - \frac{t}{\hat{t}_0}\right)^{-2} - 1 \right]. \quad (6.24)$$

6.2.2 Gravitational wave emission

A compact enough object that can survive tidal disruption at a distance of $r_p \sim \text{few} \times r_S$, will dissipate its orbital energy and angular momentum by the emission of GW radiation. As the orbit decays, both the emitted power and frequency of the GW increase. The specific orbital energy and angular momentum (per unit stellar mass) lost each orbit by the emission of GW are ($r_p > 3r_S$, $m \gg M_*$) (Peters 1964)

$$\Delta\varepsilon_{\text{GW}} = -\frac{8\pi}{5\sqrt{2}} f(e) \frac{M_* c^2}{m} \left(\frac{r_p}{r_S} \right)^{-7/2}, \quad f(e) = \frac{1 + \frac{73}{24}e^2 + \frac{37}{96}e^4}{(1+e)^{7/2}}. \quad (6.25)$$

$$\Delta J_{\text{GW}} = -\frac{16\pi}{5} g(e) \frac{GM_\star}{c} \left(\frac{r_p}{r_S} \right)^{-2}, \quad g(e) = \frac{1 + \frac{7}{8}e^2}{(1+e)^2}. \quad (6.26)$$

An orbit in the Schwarzschild metric ends in the MBH if its angular momentum is smaller than some threshold, which for bound orbits is almost independent of ε . The effective loss cone is therefore defined as the threshold angular momentum for a zero-energy orbit (e.g. Shapiro & Teukolsky 1983)

$$J_{lc} = \frac{4Gm}{c}. \quad (6.27)$$

Stars begin their inspiral on extremely eccentric orbits. The interplay between dissipation and scattering in the presence of a mass sink conserves the trend toward very high eccentricity until the very last stages of the inspiral (Hopman & Alexander 2005). For $e \sim 1$ the periastron can be expressed as $r_p/r_S = 4(J/J_{lc})^2$ and

$$\Delta \varepsilon_{\text{GW}} = \varepsilon_1 \left(\frac{J}{J_{lc}} \right)^{-7}, \quad \varepsilon_1 \equiv \frac{85\pi}{3 \times 2^{13}} \frac{M_\star c^2}{m}. \quad (6.28)$$

The GW inspiral time increases rapidly with J ,

$$\hat{t}_0 \simeq 2P_0 \frac{\varepsilon_0}{\varepsilon_1} \left(\frac{J}{J_{lc}} \right)^7. \quad (6.29)$$

GW inspiral in the GC is of interest in anticipation of the planned *Laser Interferometer Space Antenna* (LISA) mission. LISA is expected to detect GW emitted by compact objects spiraling into MBHs²⁴ at cosmological distances (Barack & Cutler 2004; Gair et al 2004). The estimated rates are 10^{-9} – 10^{-8} WD yr⁻¹ per galaxy (Hils & Bender 1995; Sigurdsson & Rees 1997; Freitag 2001; Ivanov 2002; Hopman & Alexander 2005) and 10^{-8} – 10^{-4} SBH yr⁻¹ per galaxy (Miralda-Escudé & Gould 2000; see review article on rate estimates by Sigurdsson 2003). For typical galactic density profiles, the rate depends only weakly on the relaxation time, because of the near cancellation of the t_r -dependence of the scattering rate into the “inspiral cone” and that of the volume of the diffusive regime (§6.2.1). Furthermore, the rate depends only weakly on m because of the m/σ relation (Eq. 1.1) (Hopman & Alexander 2005). Thus, the chances of detecting GW sources in any given galaxy are low, irrespective of its dynamical properties.

The one exception is the Milky Way, where the proximity of the MBH makes it possible to detect even very low-mass objects with a weak GW signal ($\Delta E_{\text{GW}} \propto M_\star^2$, Eq. 6.25) (Freitag 2003). Very low-mass MS stars dominate the population and their numbers far exceed those of compact objects (table 2.1). The mean density of a star increases with decreasing stellar mass and reaches a maximum at $M_\star < 0.1 M_\odot$, near the transition to brown dwarfs. Such stars can therefore survive the tidal field of a

²⁴LISA is sensitive to GW in the frequency range $10^{-4} \lesssim \nu \lesssim 10^{-1}$ Hz and is optimized for the range $10^{-3} \lesssim \nu \lesssim 10^{-2}$ Hz, which corresponds to the frequency at the last stable circular orbit (LSCO) for MBHs of up to $\lesssim 10^7 M_\odot$ ($\nu_{\text{LSCO}} \sim \sqrt{Gm/(3r_S^3)}/2\pi = c^3/(12\sqrt{6}\pi Gm) \sim 2 \times 10^{-3} (m/10^6 M_\odot)^{-1}$ Hz). Extreme mass-ratio GW sources are of special interest because they are the cleanest probes of spacetime near a MBH, albeit with a weak signal (Eq. 6.25; see review by Glampedakis 2005). This is to be contrasted with the yet intractable GR physics of 2 merging MBHs or NSs. The expected GW signal from inspiralling stellar mass objects at any given time is below the detector noise, but over the mission’s lifetime of several years, $\sim 10^5$ orbital periods can be observed from an active source. It should then be possible to extract the signal from the noise by utilizing the properties of the GW waveforms, which depend on the orbital parameters, in particular the eccentricity.

$\sim 10^6 M_\odot$ MBH and become GW sources. The mean number of active GW sources in the GC at any given time is $N_{GW} \sim \Gamma_i \hat{t}_0$, where \hat{t}_0 is the inspiral time from an initial orbit with $P_0 \sim 10^4$ s, the lowest frequency detectable by LISA. Freitag (2003) finds a capture rate of $\Gamma_i \sim 10^{-6} \text{ yr}^{-1}$ for low mass MS stars in the GC (but see Alexander & Hopman 2003 who find a significantly smaller rate). This correspond to a few active GW sources at any given time in the GC, $N_{GW} \sim \Gamma_i \hat{t}_0 > 1$ for $\hat{t}_0 = 2 \times 10^6$ yr (Eqs. 6.28, 6.29 with $m = 3 \times 10^6 M_\odot$, $M_\star = 0.05 M_\odot$, $r_p/r_S = 10$ and $P_0 = 10^4$ s). It is not likely that LISA will detect GW from compact objects in the GC. The rates quoted above translate to $N_{GW} \ll 1$ for the inspiral of SBHs and NSs and to $N_{GW} < 1$ for WDs (Freitag 2003).

6.2.3 Tidal heating, squeezars, and tidal capture

Dissipative interactions of MS stars with the Galactic MBH proceed primarily via tidal heating, because the tidal disruption radius for a solar mass star lies well outside the event horizon, at $r_t \sim 10 r_S$. At that distance the tidal interaction dominates over the energy released by GW emission and the interaction can be treated to good approximation in the Newtonian limit.

Inspirals by GW emission differs from inspiral by tidal heating in that the GW radiation is not localized in the star (the typical wavelength is $\lambda_{GW} \sim r_p > r_S \gg R_\star$). In contrast, the tidal energy extracted from the orbit is localized and thermalized *inside* the star. A star that is initially on a zero energy (parabolic) orbit has to dissipate many orders of magnitude its own binding energy in order to circularize,

$$E_c = \frac{GmM_\star}{2r_p} \sim \frac{1}{2} \left(\frac{m}{M_\star} \right)^{2/3} \frac{E_\star}{b} \sim 10^4 E_\star \quad (6.30)$$

where it is assumed that the circularization occurs at the initial periastron radius²⁵. It is therefore unlikely that the star will survive tidal inspiral around a MBH. It will ultimately be destroyed, either by expanding beyond its tidally limited maximal size and breaking up (r_t increases with R_\star until it overtakes r_p ; Eq. 3.2), or by exceeding its own Eddington luminosity and evaporating. Before that happens, the star will exist in a transient phase as a “squeezar”, a star whose atypically high luminosity is powered by tidal interactions with the MBH rather than by its own nuclear burning (Alexander & Morris 2003). It should be noted that tidal capture is possible around an IBH because in that case $E_c/E_\star \sim \mathcal{O}(10)$ (Eq. 6.30), and the tidal heat can be radiated away in $\mathcal{O}(10^4)$ yr (Hopman, Portegies Zwart & Alexander 2004).

The energy deposition in the star in one periastron passage can be parametrized as (cf §3.4.2, Eq. 3.30)

$$\frac{\Delta E_t}{E_\star} = \frac{T_2(b^{3/2})}{b^6} \left[\frac{R_\star(t)}{R_\star(0)} \right]^5, \quad (6.31)$$

where possible stellar expansion is taken into account by the last term. As energy and angular momentum are exchanged between the orbit and the star, the star’s mechanical and thermal properties change, and with them its response to the tidal force. Because of the feedback between the tidal interaction and the stellar properties, it is difficult to predict how the star and its orbit evolve in the course of tidal inspiral. A similar problem is encountered in studies of the circularization of tidal capture stellar binaries in clusters. The results of such studies suggest two useful limits that likely bracket the true response: surface heating with radiative cooling (McMillan, McDermott & Taam 1987) in “hot squeezars”, and bulk heating with adiabatic expansion (Podsiadlowski 1996) in “cold squeezars”. Hot squeezars dissipate the tidal heat in a very thin surface layer that expands moderately and radiates at a significantly

²⁵If the impulsive relation holds between the tidal energy and angular momentum (Eq. 3.32), then $r_p = \text{const}$ and the initial r_p is also the circularization radius. Conversely, if orbital angular momentum is conserved, then the circularization radius is $2r_p$.

increased effective temperature. This may apply to stars with large convective envelopes, where most of the energy in the oscillations is carried by eigenmodes that attain their maximal amplitude at the surface and dissipate there. Cold squeezars dissipate the tidal heat in their bulk, due to possible non-linear coupling between the high-amplitude, low-order oscillations that are directly excited by the tidal force, and an infinitude of high order modes which effectively dissipate instantaneously. Bulk heating leads to quasi-adiabatic, self-similar expansion at roughly constant effective temperature that doesn't rise much above its original value.

With these and a few additional simplifying assumptions (motion in a Keplerian potential with constant r_p) it is possible to calculate the evolution of the stellar properties and the orbit. The orbital evolution is simple when the approximation $\Delta E_t = \text{const}$ is valid (Eqs. 6.22, 6.23, 6.24). This is assumed for hot squeezars, but is not applicable to cold squeezars where ΔE_t is not constant due to the adiabatic expansion (Eq. 6.31). In that case the evolution has to be calculated numerically.

Numeric modeling of squeezer evolution (Alexander & Morris 2003) show that cold squeezars can brighten by up to $\Delta K \sim 3$ mag. The temperature of hot squeezars can rise up to $\lesssim 5$ time the original effective temperature, and the star can brighten by up to $\Delta K \sim 4$ mag (Fig. 6.2). The luminosity and temperature increase could place low mass MS squeezars ($M_\star \gtrsim 2M_\odot$) for the last $\lesssim 10^4$ yr of their life in the range of the S-stars. However, none of the S-stars for which an orbital solution is known approach the MBH close enough for tidal heating to be significant. Neither does the short squeezer cooling time allow for the possibility that these stars were tidally heated in the past and then scattered to wider orbits. Estimates of the inspiral rate for various tidal dissipation laws and their corresponding squeezer lifespans suggest that the mean number of squeezars in the GC at any given time is 0.1–1. Thus, the chances of detecting squeezars in the GC appear to be low.

The end result of tidal inspiral (sometimes also called tidal capture) is disruption and the accretion of a sizable fraction of the stellar mass by the MBH. Tidal capture was hypothesized to be an important channel of stellar mass supply to a MBH, equal to, or exceeding by up to a factor of two the contribution of direct disruption (Frank & Rees 1976; Novikov, Pethick & Polnarev 1992; Magorrian & Tremaine 1999). Simulations indicate that lower-mass MBHs ($m \lesssim 10^7 M_\odot$) in low density galactic cores obtain most of their mass from direct stellar disruption (Murphy, Cohn & Durisen 1991; Freitag & Benz 2002). If tidal capture were indeed so efficient, this would have implied that such MBHs could be wholly constructed from the disruption of stars in the radius of influence, in seeming contradiction with the empirical m/σ relation (Eq. 1.1), which holds on the much larger scale of the bulge (§1.1). The contradiction is resolved by noting that tidal capture, like any slow inspiral process, is strongly suppressed compared to direct infall. When the effects of scattering are properly taken into account (§6.2.1), it is found that tidal capture can contribute only an additional few percent above the mass supplied by direct disruption (Alexander & Hopman 2003).

6.2.4 Tidal scattering

Inspirals are very inefficient, and therefore most stars that are scattered to “near-miss” orbits pass by the MBH once and are then deflected to wider orbits. When the encounter is very close, the star will undergo an extreme non-disruptive tidal interaction and experience strong distortion, spin-up, mixing, and possibly some mass loss (Fig. 6.3). These effects may alter the star's subsequent appearance and evolution. While it is difficult to predict the long-term observational signature of such a “tidal scattering” event, plausible arguments suggest that the stellar luminosity will increase, photospheric abundances will be enriched by hydrogen-burning products (enrichment of ^4He , ^{14}N , ^{13}C and ^{26}Al and depletion of ^{12}C , ^{16}O and ^{15}N) and the stellar colors will be bluer than expected for a normal star of that mass (Alexander & Livio 2001). It is interesting to note that precisely such abundance anomalies are observed in the M supergiant IRS 7, $\sim 0.2\text{pc}$ from Sgr A* in projection (Carr, Sellgren & Balachandran

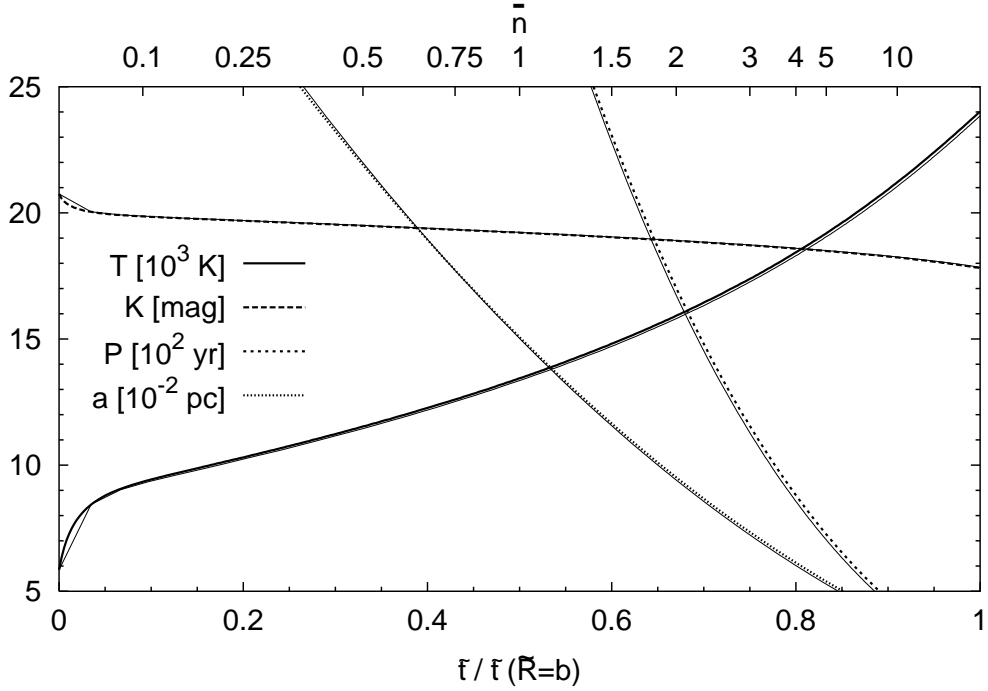


Figure 6.2: The evolution of the orbit (period and semi-major axis) and properties (temperature and K -band magnitude) a $1M_{\odot}$ hot squeezar in the GC, initially deflected into an orbit with $r_p = 1.5r_t(t=0)$ and $P_0 = 1.4 \times 10^4$ yr, which corresponds to an inspiral time of $t_0 = 4.9 \times 10^5$ yr. Time is shown relative to $t_{\text{disrupt}} = 3.7 \times 10^5$, the time when $r_p = r_t(t_{\text{disrupt}})$ and the star expands to the point where it is tidally disrupted. At disruption the tidal luminosity is $642L_{\odot}$, $P = 210$ yr and $e = 1 - 2.3 \times 10^{-4}$. For \bar{n} squeezars in the GC at any given time, the mean properties of the one in the most advanced stage of its inspiral can be read off the top axis. (Alexander & Morris 2003. Reprinted with permission from *The Astrophysical Journal*).

2000). This suggests that IRS 7 has undergone mixing in excess of values predicted by standard models or observed in supergiants elsewhere, and has prompted Carr et al. (2000) to hypothesize that “extra mixing induced by rapid rotation may indeed be the fundamental difference between the evolution of massive stars in the GC and those elsewhere in the Galaxy.”

Whatever the exact nature of the after-effects of tidal scattering, their magnitude must increase with decreasing periapse. The definition of what constitutes a strong tidal interaction depends on the tidal effect that is of interest, and this in turn corresponds to some maximal periapse r_p , beyond which the effect becomes insignificant. In spite of the smallness of the tidal radius, $r_t/r_h \sim 10^{-6}$, the number of tidally scattered stars that accumulate inside the MBH radius of influence over the age of the Galaxy can be large (up to $\lesssim 0.1$ of the population). This can be shown qualitatively by noting that most of the stars that are deflected into low angular momentum orbits originate from $a \sim r_h$ orbits (Eq. 6.11) at the transition between the diffusive regime and full-loss cone regimes. These orbits are approximately Keplerian and the DF is approximately isotropic, so that stars are deflected with equal probability to all directions. The cross-section for deflection into an eccentric orbit is then $\Sigma(<r_p) \propto r_p$, due to gravitational focusing (Hills 1975; Eq. 6.3). The rate at which stars are initially deflected into orbits with periapse smaller than r_p but larger than r_t is related to the direct disruption rate by $\Gamma_s = (r_p/r_t - 1)\Gamma_t$. This is also the tidal scattering rate to good approximation, because inspiral is a low probability process and most of

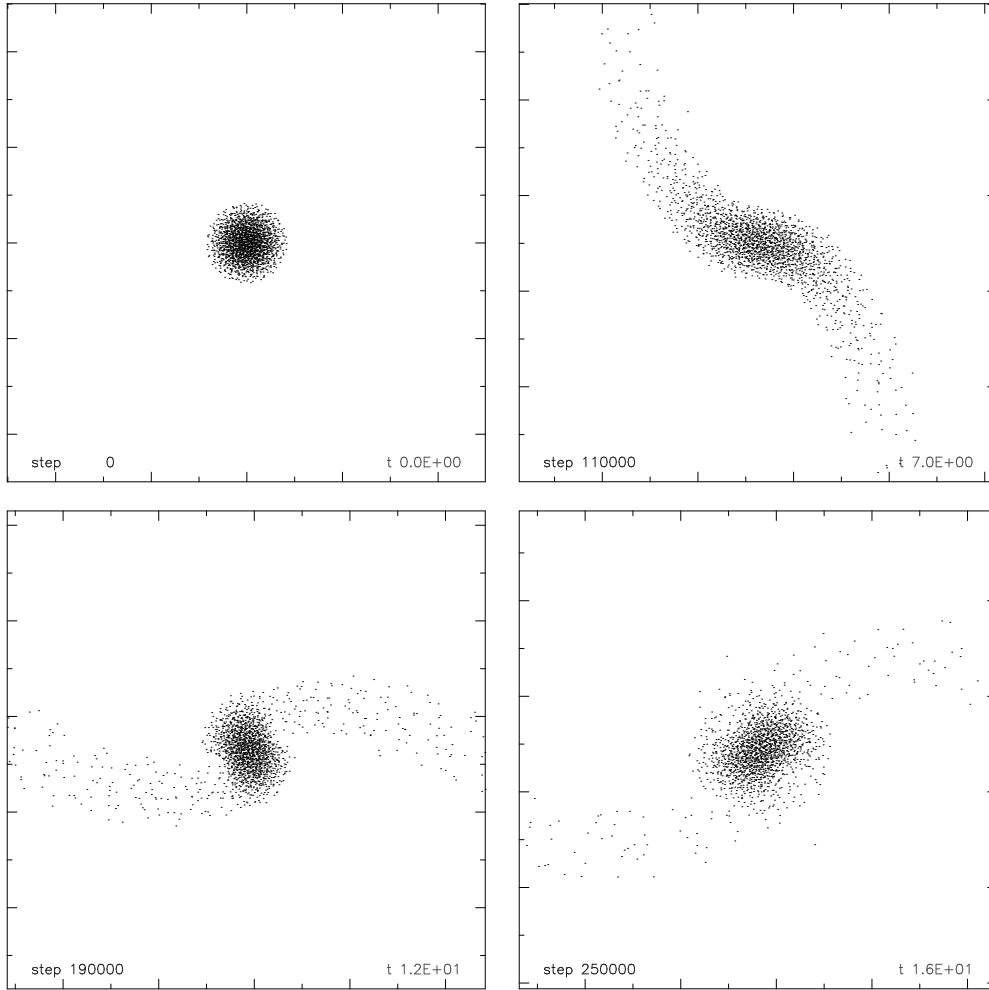


Figure 6.3: A sequence of snapshots (left to right, top to bottom) from an SPH simulation of a $10M_{\odot}$, $R_{\star}=4.5R_{\odot}$ star (represented by an $n = 1.5$ ideal gas polytrope) undergoing an extreme non-disruptive tidal interaction (“tidal scattering”) as it passes near a $3 \times 10^6 M_{\odot}$ MBH. Time is measured in units of the stellar dynamical time $\tau_{\star}=4840$ s. The star passes near the black hole (located outside of the frame) on a parabolic orbit with $r_p=100R_{\star}=1.5r_t=35.4r_S$. After periaapse passage (at $t=2.2$) the star appears to be on the verge of breaking in two (bottom left panel). However, by the end of the simulation, the two fragments coalesce, leaving a distorted, mixed and rapidly rotating bound object.

these stars will be rescattered to a wider orbit (the star can also be scattered into the loss-cone, but the probability for that is smaller because loss-cone orbits occupy a smaller volume in phase-space than wide orbits). Another effect that will prevent once-scattered stars from interacting again with the MBH is its Brownian motion (§4.2.3). The apoapse of the scattered star’s almost radial orbit will be $r_a \sim 2r_h$, where the potential is no longer dominated by the MBH. The MBH executes Brownian motion relative to the stars inside r_h with an amplitude $\sim (r_h / \langle R_{\star} \rangle) (\langle M_{\star} \rangle / m)^{5/6} r_t \gg r_t$ and a period $\sim P(r_h)$ (Bahcall & Wolf 1976). Therefore, while the star is near apoapse the MBH position will shift relative to the stellar mas inside r_h without changing much the potential at r_a , so that on its return to the center the star will miss the MBH.

More accurate calculations (Alexander & Hopman 2003) show that the tidal scattering rate in a

power-law cusp $n_\star \propto r^{-\alpha}$ in the diffusive limit is,

$$\Gamma_s(< r_p) \sim \left[\left(\frac{r_p}{r_t} \right)^\delta - 1 \right] P_s \Gamma_t, \quad \delta \equiv \frac{9-4\alpha}{8-2\alpha}, \quad (6.32)$$

where $P_s \sim 0.9$ is the survival probability against capture by the MBH and where typical values for the power-law index are $\delta=0.60$ for $\alpha=3/2$, to $\delta=0.44$ for $\alpha=7/4$. For the full loss cone regime $\delta=1$, and so the actual effective power-law index is expected to lie in the range $0.5 \lesssim \delta \lesssim 1$.

A substantial fraction f_t of the total mass of a low-mass MBH (10^6 – $10^7 M_\odot$) is supplied by tidally disrupted stars, which contribute each a fraction $f_m \lesssim 0.5$ of their mass to the MBH (§6.1.2). Simulations indicate that the total mass in tidally disrupted stars over the MBH lifetime lies in the range $0.15m \lesssim (f_t/f_m)m \lesssim 0.65m$, with the higher values typical of low-density nuclei where the population is weighted toward low mass stars (Murphy, Cohn & Durisen 1991; Freitag & Benz 2002). Assuming for example $f_t/f_m=0.25$, $\delta=0.75$ and a maximal periapse for strong tidal interaction of $r_p=1.5r_t$, it then follows from Eq. (6.32) that the mass fraction of tidally scattered stars within the MBH volume of influence is $(f_t/f_m)(\Gamma_s/\Gamma_t) \sim 0.07$. The possibility that some of the unusual stars observed in the GC may be tidally scattered stars is intriguing. However, a better understanding of the long-term observable consequences of tidal scattering is needed to make progress on this issue.

6.2.5 Star–disk interactions

Drag against an accretion disk surrounding a MBH can dissipate orbital energy, as well as affect the disk itself (e.g. Ostriker 1983; Syer, Clarke & Rees 1991; Artymowicz, Lin & Wampler 1993; Vilkuviskij & Czerny 2002). There is no evidence today for an accretion disk in the GC. It is conceivable, however, that a dim, cold, low-viscosity “fossil” disk still exists around the MBH as a remnant of past periods of activity, perhaps associated with the creation and fragmentation of the gaseous disks that may have formed the observed star disks (§7.2.1), or that a small disk is continuously fed by cooling stellar winds from the young stars around the MBH (Cuadra et al 2005; §7.3). Stellar interaction with the disk can reveal its presence, or constrain its properties (extent, optical depth). If it is optically thick, the disk can eclipse stars behind it. Stars passing through the disk will likely emit X-ray and IR flares (Nayakshin & Sunyaev 2003; Nayakshin, Cuadra & Sunyaev 2004). The disk can reprocess the stellar UV light and re-emit it in the IR (Cuadra et al. 2003). However, observations do not support the presence of a disk. IR observations of the star S2 show no eclipses or IR flares and are consistent with the absence of a disk. Furthermore, the observed IR flares coincide to within a few milli-arcseconds with Sgr A* and display a ~ 17 min quasi-period (Genzel et al. 2003a), which can not be explained by passage through a disk. The temporal structure observed in the X-ray flares (2004) is likewise inconsistent with X-ray production by passage through a disk.

7 The riddle of the young stars

The existence of young stars in the extreme environment so close to a MBH (§2.2) poses a challenge for theories of star formation and stellar dynamics (Genzel et al 2003b; Ghez et al 2003b). It has proved difficult to find a satisfactory explanation of how they could have formed so close to the MBH, or alternatively, of how they could have migrated inward from farther away in the course of their short lifespans. This is the so-called “paradox of youth”. The question applies to any of the young stars in the inner parsec, but particularly so to the central cluster of the “S-stars”, which exist a mere few hundredths of a parsec from the MBH. The problem of the young stars has become one of the major outstanding issues in GC research.

The young population in the inner ~ 1 pc is often loosely described as the “OB-stars”. This general designation can be misleading, as it fails to convey the significant systematic differences that exist in the population. An important open question is the nature of the connection, if any, between the S-stars inside ~ 0.04 pc and the luminous emission line stars further out, on the 0.04 – 0.4 pc scale. While it is plausible to assume that these are different components of the same parent population, it should be noted the two groups have distinct locations, kinematics and stellar properties. The stars detected so far in the two young star disks at $p \sim 1''$ – $10''$ are luminous OB supergiants, giants and WR stars of various types (Genzel et al. 2003b; Paumard et al. 2001; Paumard et al. 2004). In contrast, orbital solutions (Ghez et al. 2005; Eisenhauer et al. 2005) show that the S-star orbits are randomly aligned and uncorrelated with the planes of the disks. Spectral identifications (Eisenhauer et al. 2005) reveal the S-stars to be B dwarfs (S2, the brightest, is a transitional O8V–B0V star; Ghez et al. 2003b). This distinction is important, because B-stars are more numerous, less massive (by about an order of magnitude) and longer lived (by 1–2 orders of magnitude) than the luminous O-stars and WRs (Fig. 2.1). This significantly relaxes the constraints on models attempting to explain the central cluster. Thus there may actually be two separate issues: how to explain the presence of the OB stars on the >0.04 scale, and an even more acute problem, how to explain the presence of the B-stars on the <0.04 pc scale. Some of the scenarios discussed below (§7.2) attempt to address both populations with a single solution, others focus only on one or the other.

The stars in the central parsec can be described by stellar population synthesis models. Such models assume an IMF and a star formation history and use theoretically calculated stellar evolution tracks to follow the stellar population in time. Population synthesis models do not in themselves explain how the stars are born, or why the IMF and star formation history have a particular form. However, by fitting the models to the observed stellar population, it is possible to constrain these input parameters and estimate the total mass in the stars. Krabbe et al. (1995) find that the luminous early- and late-type stars can be modeled by a 7 ± 1 Myr old short burst of star formation with an IMF of $dN_*/dM_* \propto M_*^{-2}$ between $1 M_\odot$ and $120 M_\odot$ (that is, skewed to high masses as compared to the generic Salpeter IMF, $dN_*/dM_* \propto M_*^{-2.35}$), which formed ~ 3000 stars containing in total $\sim 1.5 \times 10^4 M_\odot$. An additional, older star burst $\sim 10^8$ yr ago is indicated by the intermediate-mass asymptotic branch giants. This picture is consistent with the fact that the overall population in the central few parsecs is well represented by a continuous star formation model (Alexander & Sternberg 1999; §2.2). It appears that there is ongoing episodic star formation in the GC. This suggests that we are not observing the GC at a very special epoch, but rather that the presence of young stars there is a quasi-steady state situation.

Any explanation of the luminous OB-stars on the >0.04 pc scale should account for their distinctive, disk-like distribution and kinematics and for the presence of the cluster-like structure IRS13. Any explanation of the S-stars should account for three principal properties.

1. *The stellar properties.* The stars appear to be *entirely normal* MS O8V/B0V to B9V stars, in terms of their (extinction corrected) luminosities, their absorption lines equivalent widths and line ratios (Eisenhauer et al. 2005). In particular, their rotational velocities are similar to those of nearby Galactic disk B-stars. The central cluster does not contain any star earlier than O8V, although such stars do exist outside the central arcsecond.
2. *The spatial concentration.* The relative fraction of the young stars increases toward the center, to the near exclusion of any old giant stars in the inner ~ 0.02 pc (90% of all stars with $K < 16$ mag in the central 0.02 pc are young main-sequence stars, Eisenhauer et al. 2005).
3. *The orbital properties.* The orientations of the stellar orbits appear overall random, in marked contrast to the ordered planar rotation observed for the much more luminous emission line stars farther out. There are some statistically marginal trends observed in the orbital properties: higher than random eccentricity (Schödel et al. 2003) and a lower bound on the orbital apoapse of ~ 0.01 pc.

The apparent normalcy of the B-stars is intriguing. This would seem to argue against any process that involves strong perturbations of the star, such as mergers (Genzel et al. 2003b), tidal heating (Alexander & Morris 2003) or stripping (Hansen & Milosavljević 2003). However, this is by no means a conclusive argument, because it is not clear how efficiently a star relaxes after a major perturbation, and in particular how angular momentum is lost from the star or redistributed in it.

A relevant comparison can be made with the properties of blue stragglers in clusters (MS stars that appear younger than the cluster’s single age population), whose formation is thought to involve mergers, binary coalescence or 3-body interactions (Bailyn 1995). In spite of their violent birth, observations show that in many cases, late-B blue stragglers in intermediate age globular clusters, and early-B and O blue stragglers in open clusters do not seem to rotate faster than normal stars of the same mass in the field, in spite of the fact that, unlike lower-mass stars (later than F5V), they do not have efficient magnetic braking (Leonard & Livio 1995 and references therein; §3.4.2). In this context it is interesting to note the claimed detection of a circumstellar disk around a blue straggler (de Marco et al. 2004), which may provide a breaking mechanism via magnetic anchoring. Neither is it clear whether collisional merger products should be mixed, and consequently, whether they should display unusual photospheric abundances. Lombardi, Rasio & Shapiro (1995,1996) find that the mixing by the collision itself is minimal (at least for lower mass stars near a globular cluster’s turnoff-mass). Sandquist, Bolte and Hernquist (1997) find similar results. However, subsequent convection or meridional circulation can still induce mixing (Leonard & Livio 1995; Lombardi et al 1995), although this was not found to be the case in detailed numerical work by Sills et al. (1997) and Ouellette & Pritchett (1998). In summary, “absence of proof is not proof of absence”; if the analogy to blue stragglers is justified, then it appears that the lack of unusual spectral features in the S-stars does not place strong constraints on their origin.

7.1 The difficulties of forming or importing stars near a MBH

There is little evidence for star formation in the inner parsec at this time²⁶. At present only low-density ionized gas is observed interior to the circum-nuclear molecular disk, which encircles the MBH at a radius of ~ 1.5 pc. Estimates of the molecular hydrogen density and the total mass in the disk vary from $n_{\text{H}_2} \lesssim 10^6 \text{ cm}^{-3}$ (tidally unstable, see Eq. 7.2 below) and $M \sim \text{few} \times 10^4 M_\odot$ (based on molecular line ratios; Genzel et al. 1985; Jackson et al. 1993; Marr, Wright & Backer 1993; Marshall, Lasenby & Harris 1995) to $n_{\text{H}_2} \sim 10^7 \text{ cm}^{-3}$ (tidally stable) and $M \sim 3 \times 10^5 M_\odot$ (assuming that the molecular clumps are gravitationally bound; Shukla, Yun & Scoville 2004). An additional $\lesssim 10^3 M_\odot$ may be contained in the gas and dust lanes (the “spiral”) that extrude from circum-nuclear molecular disk inward (Liszt 2003; Paumard et al. 2004; Paumard et al. 2004). Even if $> 10^4 M_\odot$ of cold molecular gas existed in the past in the central parsec, as is implied by the mass in the observed blue and red giants (Krabbe et al. 1995), it is not clear how stars could condense from the gas so close to the MBH. The minimal proto-stellar cloud density that can resist the MBH tide is extremely high compared to values typically encountered in molecular clouds elsewhere in the Galaxy ($n \lesssim 10^4 \text{ cm}^{-3}$), where star formation normally takes place. For $r \lesssim 1$ pc,

$$\min n \sim \frac{(m/m_u)}{r^3} \sim 10^8 \left(\frac{m}{3 \times 10^6 M_\odot} \right) \left(\frac{r}{1 \text{ pc}} \right)^{-3} \text{ cm}^{-3}, \quad (7.1)$$

²⁶Some resolved infrared sources were initially explained as newly born stars still enshrouded in their dust cocoons (Ott, Eckart & Genzel 1999). However, more detailed observations later revealed these to be massive stars interacting with dust lanes extruding from the circum-nuclear molecular disk inward (Tanner et al 2002; Geballe et al. 2004; Paumard et al. 2004; Tanner et al. 2005).

where m_u is the atomic mass unit and where the gravitational potential of extended stellar mass is ignored. For $r \gtrsim 1$ pc,

$$\min n \sim \frac{3(\alpha-1)M_0}{4\pi r_0^3 m_u} \left(\frac{r}{r_0}\right)^{-\alpha} \sim 4 \times 10^7 (\alpha-1) \left(\frac{M_0(1 \text{ pc})}{4 \times 10^6 M_\odot}\right) \left(\frac{r}{1 \text{ pc}}\right)^{-\alpha} \text{ cm}^{-3}, \quad (7.2)$$

where M_0 is the total mass enclosed within r_0 and it is assumed that all the mass is distributed in a $r^{-\alpha}$ cusp. These high minimal densities exceed, or are just at the inferred densities in the circum-nuclear molecular disk. In addition, the molecular clouds in the GC have large turbulent velocities ($\sim 10 \text{ km s}^{-1}$), which may provide pressure support against fragmentation, and unusually strong magnetic fields (~ 1 mG, e.g. Aitken, Moore & Roche 1998) are observed in the GC, which, if they permeate the clouds, would provide additional support against fragmentation and collapse (Morris 1993). The unavoidable conclusion is that if the young stars well inside the central parsec were formed locally, then they must have done so by a different mechanism than the collapse of self gravitating cold molecular gas clouds that occurs in normal star forming regions.

The young stars are also too short-lived and too light to have formed far from the MBH, where the tidal field is weak, and then to have migrated in by dynamical friction. The “collection basin” for the migration of young MS stars of mass of $M_\star = 15 M_\odot$ and lifespan $t_\star = 2 \times 10^7$ yr (§2.2) is only $\max r_{\text{df}} \sim 0.2 \text{ pc}$ (Eq. 3.27), and for stars of mass $M_\star = 3 M_\odot$ and lifespan $t_\star = 4 \times 10^8$ it is only $\max r_{\text{df}} \sim 0.5 \text{ pc}$.

7.2 Proposed solutions

The solutions proposed so far for the riddle of the young stars (see reviews by Genzel et al. 2003b; Ghez et al. 2005) fall into three main categories: unusual modes of star formation near the MBH; rejuvenation of old stars from the local population; and dynamic migration or capture from farther out, where stars can form. While each has some attractive features, none is quite satisfactory. The paradox of youth remains unsolved at this time.

7.2.1 Unusual *in-situ* star formation

One class of *in-situ* star formation models invokes external pressure to trigger cloud collapse. Because the clouds are stabilized against collapse by their high turbulent velocities and magnetic fields, star formation in such clouds will be skewed toward massive stars, as are observed in the GC. Cloud–cloud collisions and the resulting shocks and cooling could in principle initiate fragmentation (Morris 1993). The near identical age of the two star disks could perhaps be explained by two colliding clouds, each fragmenting to form a disk (Genzel et al. 2003b). However, it is not clear that the required very high compression ratio (Eq. 7.1) can be achieved in such collisions. An additional objection to any scenario that postulates the existence of dense clouds near the MBH is that those clouds that are dense enough to resist the tidal forces at $r \lesssim 2$ pc will also be Jeans-unstable and will fragment and presumably form stars on that large scale before reaching the center (Vollmer & Duschl 2001).

Alternatively, Morris, Ghez & Becklin (1999) propose a scenario of recurrent nuclear activity regulated by a limit cycle. At the current phase of the cycle, the circum-nuclear molecular gas disk, which has a central cavity inside ~ 1.5 pc, is prevented from filling the cavity by the radiation pressure from the hot massive stars in the center. However, once these stars die (in $\lesssim 10^7$ yr), the internal viscosity of the disk will set an inflow. The central cavity will be filled and the gas will reach the center, setting off a strong burst of luminous accretion. The radiation pressure will shock and compress the inner parts of the gas disk, presumably triggering an intense phase of star formation. Stellar winds and the combined radiation from the young massive stars and the accretion on the MBH will evacuate a central cavity, which will remain empty of gas as long as there are enough massive luminous stars inside, thereby

starting the limit cycle again. This scenario has yet to be studied in detail. Here again, the problem is that it is unclear whether radiation pressure can lead to the very high compression ratio that is required for fragmentation.

Another class of models for *in-situ* star formation propose that the young stars were formed by the fragmentation of a gaseous disk around the MBH that gradually grew in mass (perhaps fed by tidally disrupted molecular clouds, Sanders 1998) to the point it became self gravitating (Levin & Beloborodov 2003; Milosavljević & Loeb 2004; Nayakshin & Cuadra 2005). The outer parts of thin massive disks are susceptible to fragmentation (Paczynski 1978), so much so that it is, in fact, difficult to explain theoretically the observed existence of extended disks (Goodman 2003). While such a disk does not exist in the GC today, Milosavljević & Loeb (2004) point out that masering disks observed around MBHs in other galaxies (disks emitting coherent radio emission due to population inversion by shocks) have properties similar to those needed to create the star disks in the GC.

The criterion for disk fragmentation due to self-gravity (Paczynski 1978) can be expressed, up to factors of order unity, as a tidal limit, $\rho = \Sigma/h > m/r^3 \equiv \rho_c$, where Σ is the disk's surface density. The disk's scale height $h \sim c_s/\Omega$ is set by the maximal height z an atom can reach when launched from the disk mid-plane with the sound speed c_s against a vertical acceleration $a_z \simeq \Omega^2 z$ ($z \ll r$), where $\Omega = \sqrt{Gm/r^3}$ is the local Keplerian frequency. At the critical density, Ω equals the disk's gravitational free-fall rate, $\Omega = \sqrt{G\rho_c} \equiv t_{\text{ff}}^{-1}$. The Jeans (minimal) radius, R_J , and mass, M_J , of a collapsing fragment are set by the condition that the free-fall time be shorter than the sound crossing time (the time for the propagation of a gravity-resisting pressure adjustment), $R_J > c_s t_{\text{ff}}$, and $M_J > \rho_c c_s^3 / \Omega^3 = c_s^4 / (G^2 \Sigma_c)$. In addition, the gas must cool faster than the dynamical time to offset the increased pressure support from the contracting gas. For the mass and distance scales of the GC and for reasonable assumptions about the disk properties, $M_J \sim \text{few} \times 1 M_\odot$ (Levin & Beloborodov 2003). The collapsing proto-stellar cloud then begins to accrete gas from the disk within its tidal radius, $\sim (M_J/m)^{1/3} r$. The available mass there exceeds M_J by a few orders of magnitude (Levin 2003; Goodman & Tan 2004). Due to the differential rotation in the disk, the proto-stellar cloud acquires its own mini-accretion disk, which may itself become unstable and fragment to form groups of stars. Milosavljević & Loeb (2004) propose that IRS13 is such a gravitationally bound group of $\sim 2500 M_\odot$ (including low luminosity stars not yet observed), and that the S-stars were internally scattered from such groups by very hard encounters with binaries.

Nayakshin & Cuadra (2005) derive limits on the initial total masses (stars and gas) of the two star disks observed today: a lower limit of $\sim 10^4 M_\odot$ from the requirement of self-gravitation instability, and an upper limit of $10^5 M_\odot$ based on the magnitude of velocity dispersion in the outer disk that is caused by the potential of the inner disk. They are thus able to rule out the possibility that the young stars were formed by gas accretion on low mass stars that got captured in the disk. This would have required disk masses well in excess of the upper limit.

The disk fragmentation model is a promising scenario for the formation of the star disks and the massive young stars on the $\gtrsim 0.1$ pc scale, but it is less clear whether it can account for the S-cluster as well. According to their stellar contents, the two star disks are contemporaneous to better than 1 Myr, and only ~ 5 Myr old (Krabbe et al. 1995; Genzel et al 2003; Paumard et al. 2005, in prep.). Any model that associates the S-stars with the star disks has to explain why it is only B-stars that are found in the S-cluster, and not any of the more massive stars that exist in the disks. Furthermore, if the B-stars are associated with the disks, then the relevant time constraint for redistributing the orbits is the age of the disks, and not the considerably longer MS lifespan of a B-star.

7.2.2 Rejuvenation

The inner $\sim 0.02\text{--}0.03$ pc of the GC, the domain of the S-cluster, roughly coincides with the region where the stellar density is so high that stellar collisions occur more than once over the lifetime of a MS dwarf (Alexander 1999; §3.4). The strong tidal field of the MBH may also affect the stellar structure (§6.2). Rejuvenation models seek to explain the S-cluster in terms of low mass, long-lived stars that had enough time to migrate to the center from their formation sites far from the MBH (however, the central number density of such stars will be suppressed by mass segregation).

All rejuvenation models proposed so far have serious problems in explaining the S-stars. The physical processes were already discussed above in some detail, and are listed here briefly. Envelope stripping collisions (Hansen & Milosavljević 2003) will reveal a hot core, but much fine-tuning is required for the bare core to masquerade as an apparently normal B-star (§3.4.1). Tidal heating (§6.2.3) requires a very small periaapse, $r_p \lesssim 2r_t$ to be effective (Alexander & Morris 2003). Even the smallest measured periaapse to date, that of star S0-16 with $r_p \sim 600r_S \sim 30r_t$ (Ghez et al. 2005) is much too large for tidal heating to be of any relevance (tidal heating and scattering to a wider orbit can be ruled out as an explanation for its present luminosity since the scattering timescale is much longer than the stellar cooling time). Successive mergers of low-mass stars (Genzel et al. 2003b) are inefficient because the mass retention in a high velocity collision is typically very small (§3.4.3). Exotic objects formed by the capture of a compact remnant inside a normal star will probably not look like B-stars (§3.4.3).

7.2.3 Dynamical migration

Stellar dynamics are generally better understood than star formation, or the effects of far from equilibrium conditions on stellar structure and properties. Therefore models that invoke dynamical processes to explain the S-stars tend to have more definite, falsifiable predictions. The orbits and the stellar spatial distribution thus appear to be a more promising way of discriminating between models. One class of dynamical models seeks to accelerate the dynamical friction (§7.1) by attaching the young stars to a massive “anchor”. This allows the stars to form far from the MBH, where star formation is not strongly inhibited, and yet sink into the center within their short lifespans.

A natural candidate for such an anchor is a dense, young, star-forming cluster (Gerhard 2001; §2.1) like the Arches and Quintuplet clusters, which lie within tens of parsecs from the center, and contain a young population closely resembling that near the MBH, in particular He stars (Figer et al. 1999). Such a cluster, being a compact massive object ($M \sim 10^4 M_\odot$), will undergo dynamical friction and can sink to the center in 10^7 yr from a distance of ~ 5 pc (Eq. 3.27). Much more massive clusters than are seen today in the GC, with $M \sim 10^6 M_\odot$ will be able to sink in from a distance of ~ 50 pc. The problem with this scenario is that the cluster will be stripped and dissolved by the tidal field of the GC before it reaches the central parsec (Portegies Zwart, McMillan & Gerhard 2003), unless it has an extremely high central density, $\rho \sim 10^8 M_\odot \text{pc}^{-3}$ (Kim & Morris 2003). Alternatively, the center of the cluster may be stabilized against tidal stripping by a central IBH (Hansen & Milosavljević 2003).

The scenario of the dissolving cluster with an IBH proposes that a very dense stellar cluster containing an IBH, perhaps formed by runaway mergers in the cluster core (e.g. Portegies Zwart et al. 2004), sinks rapidly to the center. The stars most tightly bound to the IBH avoid tidal stripping until the IBH reaches ~ 0.1 pc from the MBH, where they are deposited in a disk-like configuration. Some of them are subsequently scattered to tighter eccentric orbits by repeated interactions with the orbiting IBH. An analogous mechanism operates in the Solar System, where Jupiter scatters comets from the outer Solar System to tightly bound inner orbits. Subsequent, more detailed simulations (Levin, Wu & Thommes 2005) showed that a dissolving cluster with an IBH can deposit its last remaining stars in a fairly thin ring (if moving on a circular orbit), but that even repeated scattering of these stars by the IBH do not lead to the formation of a tightly bound cluster such as the S-cluster. Hansen & Milosavljević

(2003) hypothesize that the S-stars are in fact O-stars from the dissolving cluster that were captured in very bound orbits by a close, nearly disruptive encounter with another star, which stripped their outer envelopes and whittled them down to B-star masses. The general concept of this model is supported by recent claims for an IBH embedded in the IRS13 “cluster” (Maillard et al. 2004; but see dissenting view by Schödel et al. 2005). The weakness of this scenario for explaining the S-stars is that, lacking quantitative calculations, it is unclear whether this method can actually form such a tightly bound cluster, and it is also unclear whether collisional stripping is efficient enough and consistent with the apparent normalcy of the B-stars.

Another objection to this scenario is the large number of massive young stars that are implied by a dissolving $M > 10^5 M_\odot$ cluster (Kim, Figer & Morris 2004; Gürkan & Rasio 2004), and which are not observed in the GC. Gürkan & Rasio (2004) show that a very massive ($M > 10^6 M_\odot$) and dense cluster starting at 10 pc can sink in less than 10^6 yr to the central 0.5 pc, bringing with it $10^4 M_\odot$ of $> 10 M_\odot$ stars while undergoing core collapse and forming a $5000 M_\odot$ IBH. However, if a lower mass cluster is assumed (and a correspondingly smaller initial radius, $r_{\text{df}} \sim 5$ pc) to mitigate the problem of the overabundance of massive stars, then in order to carry stars into the inner parsec, the IBH must have a large mass relative to the cluster, $m \gtrsim 10^4 M_\odot$ and $m/M > 0.1$. This is about 2 orders of magnitude larger than can feasibly grow in runaway mergers, $m/M \sim 10^{-3}$ (Gürkan, Freitag & Rasio 2004; Gürkan & Rasio 2004).

7.2.4 Exchange capture

Another class of dynamical scenarios are those that invoke 3-body interactions to capture the B-star on a tightly bound orbit around the MBH.

The massive binary exchange scenario (Gould & Quillen 2003) postulates that the B-star originally had a very massive binary companion ($\sim 100 M_\odot$). The binary presumably originated in a radially infalling, disintegrating massive cluster. Its radial orbit brought it close to the MBH, where in the course of a 3-body exchange interaction the B-star switched partners and became bound to the MBH. Gould & Quillen (2003) find that the probability per binary for capture in an orbit like that of the star S2 is of the order of a few percent. The weakness of this scenario is the very low joint probability for (i) having a cluster on a radial orbit, (ii) containing a very massive star, (iii) paired in a binary with a much lighter secondary (iv) with the right orbital parameters for 3-body exchange with the MBH. It also does not provide an explanation why it is that only B-stars are captured, and not more massive stars, and why there is a lower bound on the apoapse.

The exchange capture with SBHs scenario (Alexander & Livio 2004) proposes that the B-stars were originally formed far away from the MBH where normal star formation is possible (not necessarily in a massive cluster) and were then deflected into eccentric orbits that intersect the dense central concentration of SBHs (with masses of $\sim 7\text{--}10 M_\odot$), which sank to the center from the inner ~ 5 pc due to mass segregation over the lifetime of the GC (§3.3). The high concentration of the SBHs is also responsible for the collisional destruction of any tightly bound old red giants at the very center. Occasionally one of the B-stars passes very close to a SBH, knocks it out and replaces it in a bound orbit around the MBH (a 3-body exchange involving a MBH–SBH “binary” and the single B-star). This mechanism can naturally explain several of the properties of the S-cluster. The central concentration of the S-cluster follows that of the highly segregated cluster of stellar BHs. The S-cluster is composed of B-stars because they are most closely matched in mass to the stellar BHs and so have the maximal probability for exchange. The lower bound on the apoapse, ~ 0.01 pc corresponds to the point where an exchange requires that the B-star pass so close to the SBH that it is tidally disrupted. The exchange mechanism also predicts a trend toward high eccentricities in the orbits of the captured stars. The weakness of this scenario is the high required central concentration of SBHs and the large required number of B-stars on eccentric

orbits. Detailed calculations of the exchange capture cross-section and rate indicate that the SBH concentration must be close to the drain limit (Eq. 3.29) in order to sustain a steady state population of captured B-stars. These requirements may be relaxed if the source of B-stars is a dissolving cluster that approaches the SBH cluster (Gürkan & Rasio 2004), however, detailed calculations of this possibility have yet to be performed.

The stripped AGB giant capture scenario (Davies & King 2005) suggests that the S-cluster stars are the stripped core of very luminous asymptotic giant branch stars, which are captured at typical S-star periapses and periods by the dissipation of orbital energy required for tidally stripping the extended giant envelopes. The criticism leveled at this scenario is that it requires an unrealistically large number of AGB giants to sustain a steady-state S-cluster population (total mass consumed in AGB stars larger than the stellar mass in r_h); that much fine tuning is required for the stripped cores to masquerade as B stars; and that the work done to strip the envelope will be taken out of the envelope's orbital energy rather than that of the core (Goodman & Paczyński 2005).

7.3 Feeding the MBH with stellar winds

Given the yet unexplained fact that young massive stars do exist very close to the MBH, it is natural to consider the role that the mass ejected by their strong stellar winds may play in the MBH accretion. The massive He stars with their copious mass-loss winds can supply mass for accretion at a rate of $\dot{M}_w \gtrsim 10^{-3} M_\odot \text{ yr}^{-1}$. Estimates of the gas density and temperature from *Chandra* X-ray observations (Baganoff et al. 2003) imply a Bondi accretion rate (Bondi 1952; Melia 1992) of $\dot{M}_B \sim 10^{-5} M_\odot \text{ yr}^{-1} \ll \dot{M}_w$, if the accretion is spherically symmetric. Accretion at this rate by a geometrically thin, optically thick accretion disk, which has a typical radiative efficiency of $\eta \sim 0.1$ (Shakura & Sunyaev 1973; §6.1.2), can be ruled out since it would produce a luminosity of $L_B \sim \eta \dot{M}_B c^2 \sim 10^{41} \text{ erg s}^{-1}$, about 10^5 higher than observed. The implications are that (1) the He stars alone can easily supply all the mass required for accretion, and (2) SgrA* is extremely under-luminous compared to available gas supply rate. It is believed that the dimness problem of SgrA*, which is common to many MBHs in quiescent galactic nuclei, can be explained by radiatively inefficient accretion. The detection of linearly polarized sub-mm emission from SgrA* (Aitken et al. 2000; Bower et al. 2003) as well as the observed spectral energy distribution of SgrA* suggest that only $\dot{M} \sim 10^{-8} M_\odot \text{ yr}^{-1} \ll \dot{M}_B$ is accreted on the MBH, with a low efficiency of $\eta \sim 10^{-3}$. The rest of the mass is presumably carried away by a global outflow (see review by Quataert 2003). Note that $\dot{M}_{tH} \ll \dot{m}$, so the present accretion rate cannot explain the mass of the MBH. Either the MBH was accreting at much higher rates (at the level of the Bondi rate or higher) for most of its past, or else it grew by channels other than gas accretion, for example, a substantial fraction can be supplied by tidal disruption of stars, which can account in steady state for $\sim 0.5 M_\odot \Gamma_{tH} \sim 2.5 \times 10^5 M_\odot \sim 0.1 m$ (§6.1.1).

A more realistic picture of the flow of the stellar winds into the MBH must take into account the discrete distribution of stars (Coker & Melia 1997; Rockefeller et al. 2004). Cuadra et al. (2005) note that stellar mass lost by slow winds ($v \lesssim 300 \text{ km s}^{-1}$) or in a faster wind, but in the direction opposite to the star's orbital motion, will not be shocked to very high temperatures and can cool on a dynamical timescale. They simulate the gas flow from the winds of an ensemble of orbiting stars in the inner $\sim 0.35 \text{ pc}$ (roughly the region where the 2 stellar rings lie, §2.2) and find that a 2-phase gas distribution develops, with hot, X-ray emitting gas in the inner $1''$ around the MBH and a cold, fragile mini-disk further out (containing $\sim 10 M_\odot$). Cold blobs occasionally detach from the disk and flow inward, leading, if they do not evaporate, to a variable accretion rate with a variability timescale of 10^2 – 10^3 yr.

While the low level, quasi-steady state accretion of SgrA* may be supplied by the shocked winds of massive stars in the inner parsec, a time dependent component may be contributed directly by stars on eccentric orbits that approach within $\sim 10^3 r_S$ of the MBH. Loeb (2004) suggest that a fraction of

the stellar wind in the direction oriented toward the MBH can fall ballistically into the MBH, thereby possibly introducing variability that correlates with the orbital phase.

8 Outlook

8.1 Progress report

Table (8.1) summarizes the progress achieved to date (mid 2005) by the study of stars and stellar processes near the MBH in the GC, as well as the many remaining challenges. Several subjects are listed, broken down to sub-topics. For each topic, progress in three categories, theory, predictions and observations, is graded on a qualitative scale, from “unknown” to “known with confidence”. The theory category refers to the level of basic understanding of the particular object or process and the degree of confidence that it should exist or play a role in the GC. The predictions category refers to the ability to predict the observable consequences in the GC, either from a basic theory or from established empirical relations, *assuming* that the object or process is indeed relevant. The observations category refers to the extent at which observations were able to provide information on the matter (either supporting or refuting existence).

For example, concerning the nature of the dark mass, the theoretical expectation is that the dark masses in galactic centers are MBHs (based, among others, on the close analogies with Galactic “micro-quasars” (SBHs accreting from a binary companion) which are not composite objects such as clusters and most probably are not made of exotic dark mass). Furthermore, a basic theory of BHs exists. The theoretical predictions of the effect of a MBH on stellar orbits are firm, and there are empirical expectations for its mass based on the m/σ relation. Even for the less-well defined exotic dark mass alternatives it is possible to predict that there should be deviations from Keplerian motion. The observations of stellar orbits provide a compelling case for a MBH. Consequently, theory, predictions and observations for this topic are all graded as “known with confidence”. Another example, where the situation is less clear, concerns stellar collisions and mergers. While it is theoretically known with confidence that stellar collisions should occur in a high density environment, the predicted observational signature is uncertain, as it depends on the details of stellar physics. Nevertheless, there are promising, albeit still uncertain observational indications that giants are collisionally destroyed very near the MBH.

It should be emphasized that it is often the case that there isn’t one definitive theoretical prediction, either because of the complexity of the process, or because the predictions depends on various unknown parameters. The scores listed here reflect an admittedly subjective assessment of the overall robustness of the theoretical understanding and predictions. Likewise, the question whether or not available observations can come to bear on a particular topic is tied to the theoretical progress. It is quite possible that relevant observations are already available, but remain “hidden in plain sight” due to the lack of a theoretical framework.

8.2 Future directions

The main achievements resulting to date from the study of stars near the Galactic MBH (table 8.1) include the determination of the primary parameters of the central dark object (its nature, mass, location and distance), the detection of an extremely high density stellar cusp, and the observational characterization of the puzzling stellar population near the MBH. There are still many challenges in making the connection between these discoveries and the underlying theories. This review concludes with a brief survey of some of the next research frontiers and the theoretical and observational advances that are required for making progress on these issues.

Table 8.1: Score card and progress report (mid 2005)

Category	Score ^a			Remarks
	Theory/Predict./Obs.			
Primary parameters of the dark mass				
Nature of DM	✓	✓	✓	MBH, from lower limit on density (§4.2). Dynamical upper limits on extended component (§4.2.3).
Position of DM	!	!	✓	Apparent position from orbital solutions (§4.1.2). Line-of-sight distance from radial velocities (§4.1.3).
BH mass	??	!	✓	No basic theory, but mass consistent with m/σ prediction (§4.1).
BH spin ^b	✓	!	!	Quasi-period in IR accretion flares (Genzel et al. 2003a; Aschenbach et al. 2004).
Binary BH	??	!	?	IRS13? Bounds on secondary mass, distance (§4.3).
Properties of the stellar system				
Density distribution	✓	✓	✓	High density stellar cusp observed (§3.2).
Dynamical properties	!	!	✓	Vel. dispersion, anisotropy measured on all scales (§4.1.1).
Population composition	??	?	✓	Mixed old and young stellar populations (§2).
Star formation mode	??	??	?	Many ideas, but still no definite conclusion (§2.1).
Stellar dynamical processes				
Relaxation	✓	!	!	Observed cusp slope and velocity dispersion of old population consistent with relaxation (§3.2).
Mass segregation	✓	!	?	Strong segregation expected. Some evidence for overabundance of compact objects (§3.3).
Collisions/mergers	✓	?	!	Depletion of bright giants toward center (§3.4).
Tidal spin-up	!	?	??	Evidence of (rotational?) mixing (§3.4.2)
Star disks	?	??	✓	Star formation in fragmenting gas disks? (§2.2).
Stellar interactions with the MBH				
Tidal disruption	✓	?	?	Evidence inconclusive (§6.1).
Tidal scattering/heating	!	?	??	Process inevitable, signature uncertain (§6.2.3, §6.2.4).
Interactions with cold disk	??	!	✓	No evidence of cold disk (§6.2.5).
Post Newtonian physics				
Gravitational redshift	✓	✓	—	Awaiting more orbital data (§5.1.1).
Orbital precession	✓	!	—	Awaiting short period, better astrometry orbits (§5.1).
Frame dragging	✓	!	??	Proposed detection depends on untestable assumptions about the star S2 (§5.1).
Gravitational lensing	✓	!	?	Expected lensing probability low (§5.2).
Gravitational waves	!	!	—	Awaiting future detectors (§6.2.2).

^a ‘✓’ known with confidence; ‘!’ promising but uncertain; ‘?’ uncertain; ‘??’ speculative; ‘—’ unknown or not applicable

^b Listed here for completeness. This estimate was derived from gas accretion properties, not stellar processes.

A yet unrealized goal is the detection of post-Newtonian effects in the stellar orbits (§5.1). The prospects of progress will be much improved if stars on even tighter and more eccentric orbits than those observed today are detected. Such stars, if they exist, must be less massive and less luminous than the faintest stars already detected near the MBH, late B-stars ($M_* \gtrsim 3 M_\odot$). The question whether such stars are present near the MBH is closely linked to the issue of mass segregation (§4.2.3). If, as is anticipated, most of the objects near the MBH are massive remnants, then the density of low mass stars there will be significantly suppressed. Furthermore, collisional destruction will limit the lifespan of tightly bound stars (§3.4.1).

To detect and track stellar orbits in a field that becomes increasingly cluttered as more faint stars are revealed (“source confusion”), it will be necessary to increase the photometric, astrometric and spectroscopic sensitivities. This can be achieved by much larger telescopes than the existing 8–10 m class telescopes, which will have a correspondingly smaller diffraction limit (e.g. the proposed Thirty Meter Telescope (TMT), for GC applications see Weinberg, Milosavljević & Ghez 2005). Alternatively, optical/IR interferometers such as the Very Large Telescope Interferometer (VLTI), the Keck interferometer and the Large Binocular Telescope (LBT) will achieve very high angular resolution and may also reach high photometric sensitivity with adaptive optics. Monitoring a short period star will require frequent sampling to avoid losing track of the star in the dense field, and to obtain good coverage of the orbit, especially near periape, where the post-Newtonian deviations are largest (§5.1).

A closely related problem is the detection and characterization of the extended dark mass around the MBH. Orbital monitoring can also detect deviations from Keplerian orbits due to a smooth distribution of dark mass or perturbations due to interactions with discrete objects (compact remnants). It may also reveal gravitational lensing events (§5.2) involving both the MBH and the cluster of compact remnants or faint stars around it (Alexander & Loeb 2001; Chanamé, Gould & Miralda-Escudé 2001). On a scale larger than probed by the orbits, X-ray surveys have already discovered an over-abundance of transient X-ray sources in the central parsec, which are thought to be NSs or SBHs accreting from a binary companion (Muno et al. 2005). Deep surveys at short radio wavelengths may probe the distribution of millisecond pulsars, which, as long-lived light test particles, are expected to be depleted in the center (Chanamé & Gould 2002). The distribution of other long-lived light test particles, such as red clump giants, should also be sensitive to the degree of mass segregation. Theoretical predictions of the details of mass segregation around a MBH are only available for highly idealized situations (Bahcall & Wolf 1977), and the application to real systems is unclear. Dynamical simulations of stellar systems around a MBH (e.g. Freitag & Benz 2002; Preto, Merritt & Spurzem 2004; Baumgardt, Makino & Ebisuzaki 2004) that take stellar evolution and continuous star formation into account will be needed to confirm and refine these predictions.

The detection of evidence of past strong interactions between stars and the MBH and between stars themselves (§6, §3.4) will require large area surveys, in particular spectroscopic surveys, to look for tell-tale peculiar stellar properties. There are however still no robust theoretical predictions of the appearance of stars that were subjected to major perturbations. Any progress on this complex problem will be very relevant for such searches, and conversely, the stellar population in the inner GC can be used test these ideas.

The attempts to solve the riddle of the young stars (§7) raise many interesting possibilities about the contents and history of the inner GC. A deep spectroscopic survey of the inner $\sim 15''$ will help disentangle the different stellar populations there and provide clues about the history and origin of the young stars and the properties of the star disks. Such a survey can establish whether or not apparent concentrations of stars, such as IRS13, are indeed self-bound objects, perhaps harboring an IBH.

The Galactic MBH provides a uniquely accessible laboratory for studying in detail the connections and interactions between a massive black hole and the stellar system in which it grows; for investigating the effects of extreme density, velocity and tidal fields on stars; and for using stars to probe the central

dark mass and post-Newtonian gravity in the weak- and strong-field limits. These issues are relevant for understanding the MBH phenomenon in general. The wealth of observed phenomena in the GC provides the impetus to study stellar processes in the extreme environment near a MBH. As shown in this review, such studies prove to be very fruitful, yielding valuable insights even in cases where they do not fully succeed to explain the observations. Many questions remain—it is quite likely that the most exciting science still lies ahead.

Acknowledgements

Helpful discussions and comments by F. Eisenhauer, R. Genzel, S. Gillessen, C. Hopman and S. Zucker are gratefully acknowledged. Useful comments by the referee, Y. Levin, are much appreciated. This work was supported by ISF grant 295/02-1, Minerva grant 8484 and a New Faculty grant by Sir H. Djangoly, CBE, of London, UK.

References

- Abramowicz, M. A., Chen, X., Kato, S., Lasota, J., Regev, O., 1995. Thermal equilibria of accretion disks. *ApJ* 438, L37–L39. ► See p. 62
- Afonso, C., et al., 2003. Bulge microlensing optical depth from EROS 2 observations. *A&A* 404, 145–156. ► See p. 52
- Aharonian, F., et al., 2004. Very high energy gamma rays from the direction of Sagittarius A*. *A&A* 425, L13–L17. ► See p. 43
- Aitken, D. K., Greaves, J., Chrysostomou, A., Jenness, T., Holland, W., Hough, J. H., Pierce-Price, D., Richer, J., 2000. Detection of Polarized Millimeter and Submillimeter Emission from Sagittarius A*. *ApJ* 534, L173–L176. ► See p. 82
- Aitken, D. K., Smith, C. H., Moore, T. J. T., Roche, P. F., 1998. Mid-infrared polarization studies of SgrA: a three-dimensional study of the central parsec. *MNRAS* 299, 743–752. ► See p. 78
- Alexander, T., 1999. The Distribution of Stars near the Supermassive Black Hole in the Galactic Center. *ApJ* 527, 835–850. ► See p. 9, 20, 21, 25, 26, 50, 52, 55, 80
- Alexander, T., 2001. Pinpointing the Massive Black Hole in the Galactic Center with Gravitationally Lensed Stars. *ApJ* 553, L149–L152. ► See p. 52, 54
- Alexander, T., 2003. Stars and singularities: stellar phenomena near a massive black hole. In: Falcke, H., Hehl, F. (Eds.), *The Galactic Black Hole*. Institute of Physics, Bristol, pp. 246–275. ► See p. 6
- Alexander, T., Hopman, C., 2003. Orbital In-spiral into a Massive Black Hole in a Galactic Center. *ApJ* 590, L29–L32. ► See p. 59, 67, 71, 72, 74
- Alexander, T., Kumar, P., 2001. Tidal Spin-up of Stars in Dense Stellar Cusps around Massive Black Holes. *ApJ* 549, 948–958. ► See p. 27, 28, 29
- Alexander, T., Livio, M., 2001. Tidal Scattering of Stars on Supermassive Black Holes in Galactic Centers. *ApJ* 560, L143–L146. ► See p. 72
- Alexander, T., Livio, M., 2004. Orbital Capture of Stars by a Massive Black Hole via Exchanges with Compact Remnants. *ApJ* 606, L21–L24. ► See p. 23, 24, 81
- Alexander, T., Loeb, A., 2001. Enhanced Microlensing by Stars around the Black Hole in the Galactic Center. *ApJ* 551, 223–230. ► See p. 50, 52, 56, 85
- Alexander, T., Morris, M., 2003. Squeezars: Tidally Powered Stars Orbiting a Massive Black Hole. *ApJ* 590, L25–L28. ► See p. 71, 72, 73, 77, 80
- Alexander, T., Sternberg, A., 1999. Near-Infrared Microlensing of Stars by the Supermassive Black Hole in the Galactic Center. *ApJ* 520, 137–148. ► See p. 10, 54, 76

- Allen, D. A., Hyland, A. R., Hillier, D. J., 1990. The source of luminosity at the Galactic Centre. *MNRAS* 244, 706–713. ► See p. 10
- Allen, D. A., Hyland, A. R., Jones, T. J., 1983. High-resolution images of the Galactic Centre. *MNRAS* 204, 1145–1152. ► See p. 21
- Artymowicz, P., Lin, D. N. C., Wampler, E. J., 1993. Star trapping and metallicity enrichment in quasars and active galactic nuclei. *ApJ* 409, 592–603. ► See p. 75
- Aschenbach, B., Grosso, N., Porquet, D., Predehl, P., 2004. X-ray flares reveal mass and angular momentum of the Galactic Center black hole. *A&A* 417, 71–78. ► See p. 46, 49, 75, 84
- Atakan Gürkan, M., Rasio, F. A., 2004. The Disruption of Stellar Clusters Containing Massive Black Holes near the Galactic Center. *ApJ* In press, [arXiv:astro-ph/0412452](https://arxiv.org/abs/astro-ph/0412452). ► See p. 81, 82
- Ayal, S., Livio, M., Piran, T., 2000. Tidal Disruption of a Solar-Type Star by a Supermassive Black Hole. *ApJ* 545, 772–780. ► See p. 61, 62, 63
- Backer, D. C., Sramek, R. A., 1999. Proper Motion of the Compact, Nonthermal Radio Source in the Galactic Center, Sagittarius A*. *ApJ* 524, 805–815. ► See p. 40
- Baes, M., Buyle, P., Hau, G. K. T., Dejonghe, H., 2003. Observational evidence for a connection between supermassive black holes and dark matter haloes. *MNRAS* 341, L44–L48. ► See p. 4
- Baganoff, F. K., et al., 2001. Rapid X-ray flaring from the direction of the supermassive black hole at the Galactic Centre. *Nature* 413, 45–48. ► See p. 31, 41, 65
- Baganoff, F. K., et al., 2003. Chandra X-Ray Spectroscopic Imaging of Sagittarius A* and the Central Parsec of the Galaxy. *ApJ* 591, 891–915. ► See p. 11, 82
- Bahcall, J. N., Tremaine, S., 1981. Methods for determining the masses of spherical systems. I - Test particles around a point mass. *ApJ* 244, 805–819. ► See p. 34
- Bahcall, J. N., Wolf, R. A., 1976. Star distribution around a massive black hole in a globular cluster. *ApJ* 209, 214–232. ► See p. 17, 74
- Bahcall, J. N., Wolf, R. A., 1977. The star distribution around a massive black hole in a globular cluster. II Unequal star masses. *ApJ* 216, 883–907. ► See p. 17, 85
- Bailey, V. C., Davies, M. B., 1999. Red giant collisions in the Galactic Centre. *MNRAS* 308, 257–270. ► See p. 25
- Bailyn, C. D., 1995. Blue Stragglers and Other Stellar Anomalies: Implications for the Dynamics of Globular Clusters. *ARA&A* 33, 133–162. ► See p. 77
- Balick, B., Brown, R. L., 1974. Intense sub-arcsecond structure in the galactic center. *ApJ* 194, 265–270. ► See p. 3
- Barack, L., Cutler, C., 2004. LISA capture sources: Approximate waveforms, signal-to-noise ratios, and parameter estimation accuracy. *Phys. Rev. D* 69 (8), 082005–+. ► See p. 70
- Baumgardt, H., Makino, J., Ebisuzaki, T., 2004. Massive Black Holes in Star Clusters. II. Realistic Cluster Models. *ApJ* 613, 1143–1156. ► See p. 17, 85
- Beloborodov, A. M., Levin, Y., 2004. Orbital Roulette: A New Method of Gravity Estimation from Observed Motions. *ApJ* 613, 224–237. ► See p. 35
- Bicknell, G. V., Gingold, R. A., 1983. On tidal detonation of stars by massive black holes. *ApJ* 273, 749–760. ► See p. 66
- Biehle, G. T., 1991. High-mass stars with degenerate neutron cores. *ApJ* 380, 167–184. ► See p. 30
- Biehle, G. T., 1994. Observational prospects for massive stars with degenerate neutron cores. *ApJ* 420, 364–373. ► See p. 30
- Binney, J., Tremaine, S., 1987. *Galactic Dynamics*. Princeton University Press, Princeton, NJ. ► See p. 13, 16, 17, 18, 22, 33
- Blandford, R. D., Begelman, M. C., 1999. On the fate of gas accreting at a low rate on to a black hole.

- MNRAS 303, L1–L5. ► See p. 62
- Bogdanović, T., Eracleous, M., Mahadevan, S., Sigurdsson, S., Laguna, P., 2004. Tidal Disruption of a Star by a Black Hole: Observational Signature. *ApJ* 610, 707–721. ► See p. 61
- Bondi, H., 1952. On spherically symmetrical accretion. *MNRAS* 112, 195–+. ► See p. 30, 82
- Bower, G. C., Falcke, H., Herrnstein, R. M., Zhao, J., Goss, W. M., Backer, D. C., 2004. Detection of the Intrinsic Size of Sagittarius A* Through Closure Amplitude Imaging. *Science* 304, 704–708. ► See p. 38
- Bower, G. C., Wright, M. C. H., Falcke, H., Backer, D. C., 2003. Interferometric Detection of Linear Polarization from Sagittarius A* at 230 GHz. *ApJ* 588, 331–337. ► See p. 82
- Bozza, V., Mancini, L., 2004. Gravitational Lensing by Black Holes: A Comprehensive Treatment and the Case of the Star S2. *ApJ* 611, 1045–1053. ► See p. 55
- Brown, W. R., Geller, M. J., Kenyon, S. J., Kurtz, M. J., 2005. Discovery of an Unbound Hypervelocity Star in the Milky Way Halo. *ApJ* 622, L33–L36. ► See p. 45
- Brumberg, V. A., 1991. Essential relativistic celestial mechanics. Institute of Physics, Bristol. ► See p. 47
- Cannizzo, J. K., Lee, H. M., Goodman, J., 1990. The disk accretion of a tidally disrupted star onto a massive black hole. *ApJ* 351, 38–46. ► See p. 61, 64
- Capozziello, S., Iovane, G., 1999. Probing the nature of compact dark object at the Galactic Center by gravitational lensing. *Physics Letters A* 259, 185–193. ► See p. 55
- Carr, J. S., Sellgren, K., Balachandran, S. C., 2000. The First Stellar Abundance Measurements in the Galactic Center: The M Supergiant IRS 7. *ApJ* 530, 307–322. ► See p. 73
- Carter, B., 1992. Cosmic gamma-ray bursts from black hole tidal disruption of stars? *ApJ* 391, L67–L70. ► See p. 66
- Carter, B., Luminet, J. P., 1982. Pancake detonation of stars by black holes in galactic nuclei. *Nature* 296, 211–214. ► See p. 66
- Carter, B., Luminet, J.-P., 1983. Tidal compression of a star by a large black hole. I Mechanical evolution and nuclear energy release by proton capture. *A&A* 121, 97–113. ► See p. 66
- Chakrabarty, D., Saha, P., 2001. A Nonparametric Estimate of the Mass of the Central Black Hole in the Galaxy. *AJ* 122, 232–241. ► See p. 34, 35, 36, 39
- Chanamé, J., Gould, A., 2002. Millisecond Pulsars as Probes of Mass Segregation in the Galactic Center. *ApJ* 571, 320–325. ► See p. 24, 85
- Chanamé, J., Gould, A., Miralda-Escudé, J., 2001. Microlensing by Stellar Black Holes around Sagittarius A*. *ApJ* 563, 793–799. ► See p. 24, 56, 85
- Chandrasekhar, S., 1939. An introduction to the study of stellar structure. Chicago, Ill., The University of Chicago press. ► See p. 42
- Chandrasekhar, S., 1943. Dynamical Friction. I. General Considerations: the Coefficient of Dynamical Friction. *ApJ* 97, 255–+. ► See p. 22
- Chandrasekhar, S., 1944. The Statistics of the Gravitational Field Arising from a Random Distribution of Stars. IV. The Stochastic Variation of the Force Acting on a Star. *ApJ* 99, 47–+. ► See p. 31
- Chatterjee, P., Hernquist, L., Loeb, A., 2002a. Brownian Motion in Gravitationally Interacting Systems. *Physical Review Letters* 88, 121103. ► See p. 44
- Chatterjee, P., Hernquist, L., Loeb, A., 2002b. Dynamics of a Massive Black Hole at the Center of a Dense Stellar System. *ApJ* 572, 371–381. ► See p. 44
- Clénet, Y., Rouan, D., Gratadour, D., Lacombe, F., Gendron, E., Genzel, R., Ott, T., Schödel, R., Léna, P., 2004a. Detection of the Sgr A* activity at 3.8 and 4.8 μm with NACO. *A&A* 424, L21–L25. ► See p. 54

- Clénet, Y., et al., 2004b. The infrared L'-band view of the Galactic Center with NAOS-CONICA at VLT. *A&A* 417, L15–L19. ► See p. 55
- Cohn, H., Kulsrud, R. M., 1978. The stellar distribution around a black hole - Numerical integration of the Fokker-Planck equation. *ApJ* 226, 1087–1108. ► See p. 18, 59
- Coker, R. F., Melia, F., 1997. Hydrodynamical Accretion onto Sagittarius A* from Distributed Point Sources. *ApJ* 488, L149+. ► See p. 82
- Cox, A. N., 2000. Allen's astrophysical quantities. New York: AIP Press; Springer, 4th ed. ► See p. 9, 13
- Cuadra, J., Nayakshin, S., Springel, V., Di Matteo, T., 2005. Accretion of cool stellar winds on to Sgr A*: another puzzle of the Galactic Centre? *MNRAS* 360, L55–L59. ► See p. 75, 82
- Cuadra, J., Nayakshin, S., Sunyaev, R., 2003. Bright stars and an optically thick inactive disk in Sgr A* and other dormant galaxy centers. *A&A* 411, 405–416. ► See p. 75
- Davidge, T. J., Simons, D. A., Rigaut, F., Doyon, R., Crampton, D., 1997. The Stellar Content Near the Galactic Center. *AJ* 114, 2586–+. ► See p. 10
- Davies, M. B., Benz, W., Hills, J. G., 1991. Stellar encounters involving red giants in globular cluster cores. *ApJ* 381, 449–461. ► See p. 25
- Davies, M. B., Blackwell, R., Bailey, V. C., Sigurdsson, S., 1998. The destructive effects of binary encounters on red giants in the Galactic Centre. *MNRAS* 301, 745–753. ► See p. 25
- Davies, M. B., King, A., 2005. The Stars of the Galactic Center. *ApJ* 624, L25–L27. ► See p. 65, 82
- De Marco, O., Lanz, T., Ouellette, J. A., Zurek, D., Shara, M. M., 2004. First Evidence of Circumstellar Disks around Blue Straggler Stars. *ApJ* 606, L151–L154. ► See p. 77
- De Paolis, F., Geralico, A., Ingrosso, G., Nucita, A. A., 2003. The black hole at the galactic center as a possible retro-lens for the S2 orbiting star. *A&A* 409, 809–812. ► See p. 55
- Di Stefano, R., Greiner, J., Murray, S., Garcia, M., 2001. A New Way to Detect Massive Black Holes in Galaxies: The Stellar Remnants of Tidal Disruption. *ApJ* 551, L37–L40. ► See p. 65
- Diener, P., Frolov, V. P., Khokhlov, A. M., Novikov, I. D., Pethick, C. J., 1997. Relativistic Tidal Interaction of Stars with a Rotating Black Hole. *ApJ* 479, 164. ► See p. 61
- Doeleman, S. S., Shen, Z.-Q., Rogers, A. E. E., Bower, G. C., Wright, M. C. H., Zhao, J. H., Backer, D. C., Crowley, J. W., Freund, R. W., Ho, P. T. P., Lo, K. Y., Woody, D. P., 2001. Structure of Sagittarius A* at 86 GHz using VLBI Closure Quantities. *AJ* 121, 2610–2617. ► See p. 38, 41
- Eckart, A., Genzel, R., 1996. Observations of stellar proper motions near the Galactic Centre. *Nature* 383, 415–417. ► See p. 31, 47
- Eckart, A., Genzel, R., 1997. Stellar proper motions in the central 0.1 PC of the Galaxy. *MNRAS* 284, 576–598. ► See p. 36
- Eckart, A., Genzel, R., Ott, T., Schödel, R., 2002. Stellar orbits near Sagittarius A*. *MNRAS* 331, 917–934. ► See p. 31, 36
- Eckart, A., Ott, T., Genzel, R., 1999. The Sgr A* stellar cluster: New NIR imaging and spectroscopy. *A&A* 352, L22–L25. ► See p. 13
- Eich, C., Zimmermann, M. E., Thorne, K. S., Zytow, A. N., 1989. Giant and supergiant stars with degenerate neutron cores. *ApJ* 346, 277–283. ► See p. 30
- Eisenhauer, F., Schödel, R., Genzel, R., Ott, T., Tecza, M., Abuter, R., Eckart, A., Alexander, T., 2003. A Geometric Determination of the Distance to the Galactic Center. *ApJ* 597, L121–L124. ► See p. 4, 9, 15, 31, 32, 39, 40, 47
- Eisenhauer, F., et al., 2005. SINFONI in the Galactic Center: Young Stars and Infrared Flares in the Central Light-Month. *ApJ* 628, 246–259. ► See p. 13, 31, 32, 38, 39, 40, 47, 49, 50, 76
- Evans, C. R., Kochanek, C. S., 1989. The tidal disruption of a star by a massive black hole. *ApJ* 346, L13–L16. ► See p. 61, 62

- Fabian, A. C., Nandra, K., Reynolds, C. S., Brandt, W. N., Otani, C., Tanaka, Y., Inoue, H., Iwasawa, K., 1995. On broad iron K α lines in Seyfert 1 galaxies. *MNRAS* 277, L11–L15. ► See p. 46
- Falcke, H., Hehl, F. W., 2003. The Galactic Black Hole. Institute of Physics, Bristol. ► See p. 6
- Ferrarese, L., 2002. Beyond the Bulge: A Fundamental Relation between Supermassive Black Holes and Dark Matter Halos. *ApJ* 578, 90–97. ► See p. 4
- Ferrarese, L., Ford, H., 2005. Supermassive Black Holes in Galactic Nuclei: Past, Present and Future Research. *Space Science Reviews* 116, 523–624. ► See p. 3
- Ferrarese, L., Merritt, D., 2000. A Fundamental Relation between Supermassive Black Holes and Their Host Galaxies. *ApJ* 539, L9–L12. ► See p. 4
- Figer, D. F., 2003. Massive Stars and The Creation of our Galactic Center. *Astronomische Nachrichten Supplement* 324, 255–261. ► See p. 7
- Figer, D. F., 2005. An upper limit to the masses of stars. *Nature* 434, 192–194. ► See p. 7
- Figer, D. F., Kim, S. S., Morris, M., Serabyn, E., Rich, R. M., McLean, I. S., 1999. Hubble Space Telescope/NICMOS Observations of Massive Stellar Clusters near the Galactic Center. *ApJ* 525, 750–758. ► See p. 7, 80
- Figer, D. F., Rich, R. M., Kim, S. S., Morris, M., Serabyn, E., 2004. An Extended Star Formation History for the Galactic Center from Hubble Space Telescope NICMOS Observations. *ApJ* 601, 319–339. ► See p. 7
- Figer, D. F., et al., 2000. 2 Micron Spectroscopy within 0.3 arcsec of Sagittarius A*. *ApJ* 533, L49–L52. ► See p. 13, 25
- Forrest, W. J., Shure, M. A., Pipher, J. L., Woodward, C. E., 1987. Brackett Alpha Images. In: AIP Conf. Proc. 155: The Galactic Center. pp. 153–+. ► See p. 10
- Fragile, P. C., Mathews, G. J., 2000. Reconstruction of Stellar Orbits Close to Sagittarius A*: Possibilities for Testing General Relativity. *ApJ* 542, 328–333. ► See p. 47, 49
- Frank, J., 1978. Tidal disruption by a massive black hole and collisions in galactic nuclei. *MNRAS* 184, 87–99. ► See p. 56
- Frank, J., Rees, M. J., 1976. Effects of massive central black holes on dense stellar systems. *MNRAS* 176, 633–647. ► See p. 56, 58, 59, 60, 72
- Freitag, M., 2001. Monte Carlo cluster simulations to determine the rate of compact star inspiralling to a central galactic black hole. *Classical and Quantum Gravity* 18, 4033–4038. ► See p. 67, 70
- Freitag, M., 2003. Gravitational Waves from Stars Orbiting the Sagittarius A* Black Hole. *ApJ* 583, L21–L24. ► See p. 70, 71
- Freitag, M., Benz, W., 2002. A new Monte Carlo code for star cluster simulations. II. Central black hole and stellar collisions. *A&A* 394, 345–374. ► See p. 72, 75, 85
- Freitag, M., Benz, W., 2005. A comprehensive set of simulations of high-velocity collisions between main-sequence stars. *MNRAS*, 245–+. ► See p. 30
- Freitag, M., Gürkan, M. A., Rasio, F. A., 2004. Collisions Between Single Stars in Dense Clusters: Runaway Formation of a Massive Object. In: St-Louis, N., Moffat, A. (Eds.), ASP conf. Ser. Vol. 30: Massive Stars in Interacting Binaries. [arXiv:astro-ph/0410327](https://arxiv.org/abs/astro-ph/0410327). ► See p. 30
- Frolov, V. P., Khokhlov, A. M., Novikov, I. D., Pethick, C. J., 1994. Relativistic tidal interaction of a white dwarf with a massive black hole. *ApJ* 432, 680–689. ► See p. 61
- Gair, J. R., Barack, L., Creighton, T., Cutler, C., Larson, S. L., Phinney, E. S., Vallisneri, M., 2004. Event rate estimates for LISA extreme mass ratio capture sources. *Classical and Quantum Gravity* 21, 1595–. ► See p. 70
- Geballe, T. R., Rigaut, F., Roy, J.-R., Draine, B. T., 2004. A Bow Shock of Heated Dust Surrounding Galactic Center Source IRS 8. *ApJ* 602, 770–775. ► See p. 77
- Gebhardt, K., Richstone, D., Tremaine, S., Lauer, T. R., Bender, R., Bower, G., Dressler, A., Faber,

- S. M., Filippenko, A. V., Green, R., Grillmair, C., Ho, L. C., Kormendy, J., Magorrian, J., Pinkney, J., 2003. Axisymmetric Dynamical Models of the Central Regions of Galaxies. *ApJ* 583, 92–115. ► See p. 3, 44
- Gebhardt, K., et al., 2000. A Relationship between Nuclear Black Hole Mass and Galaxy Velocity Dispersion. *ApJ* 539, L13–L16. ► See p. 4
- Genzel, R., Crawford, M. K., Townes, C. H., Watson, D. M., 1985. The neutral-gas disk around the galactic center. *ApJ* 297, 766–786. ► See p. 77
- Genzel, R., Eckart, A., Ott, T., Eisenhauer, F., 1997. On the nature of the dark mass in the centre of the Milky Way. *MNRAS* 291, 219–234. ► See p. 13, 31, 54
- Genzel, R., Hollenbach, D., Townes, C. H., 1994. The nucleus of our Galaxy. *Reports of Progress in Physics* 57, 417–479. ► See p. 6, 7
- Genzel, R., Pichon, C., Eckart, A., Gerhard, O. E., Ott, T., 2000. Stellar dynamics in the Galactic Centre: proper motions and anisotropy. *MNRAS* 317, 348–374. ► See p. 11, 12, 13, 17, 19, 33, 34, 35, 36, 40
- Genzel, R., Schödel, R., Ott, T., Eckart, A., Alexander, T., Lacombe, F., Rouan, D., Aschenbach, B., 2003a. Near-infrared flares from accreting gas around the supermassive black hole at the Galactic Centre. *Nature* 425, 934–937. ► See p. 31, 33, 37, 46, 49, 54, 75, 84
- Genzel, R., Thatte, N., Krabbe, A., Kroker, H., Tacconi-Garman, L. E., 1996. The Dark Mass Concentration in the Central Parsec of the Milky Way. *ApJ* 472, 153–172. ► See p. 10, 17, 19, 20, 25, 34, 36
- Genzel, R., Townes, C. H., 1987. Physical conditions, dynamics, and mass distribution in the center of the Galaxy. *ARA&A* 25, 377–423. ► See p. 6, 34
- Genzel, R., et al., 2003b. The Stellar Cusp around the Supermassive Black Hole in the Galactic Center. *ApJ* 594, 812–832. ► See p. 9, 10, 11, 12, 13, 20, 21, 22, 24, 26, 29, 75, 76, 77, 78, 80
- Gerhard, O., 2001. The Galactic Center HE I Stars: Remains of a Dissolved Young Cluster? *ApJ* 546, L39–L42. ► See p. 80
- Gezari, S., Ghez, A. M., Becklin, E. E., Larkin, J., McLean, I. S., Morris, M., 2002. Adaptive Optics Near-Infrared Spectroscopy of the Sagittarius A* Cluster. *ApJ* 576, 790–797. ► See p. 13
- Ghez, A. M., Becklin, E., Duchjné, G., Hornstein, S., Morris, M., Salim, S., Tanner, A., 2003a. Full Three Dimensional Orbits For Multiple Stars on Close Approaches to the Central Supermassive Black Hole. *Astronomische Nachrichten Supplement* 324, 527–533. ► See p. 39
- Ghez, A. M., Klein, B. L., Morris, M., Becklin, E. E., 1998. High Proper-Motion Stars in the Vicinity of Sagittarius A*: Evidence for a Supermassive Black Hole at the Center of Our Galaxy. *ApJ* 509, 678–686. ► See p. 13, 17, 19, 31, 34, 36, 47, 54
- Ghez, A. M., Morris, M., Becklin, E. E., Tanner, A., Kremenek, T., 2000. The accelerations of stars orbiting the Milky Way’s central black hole. *Nature* 407, 349–351. ► See p. 31, 36, 37
- Ghez, A. M., Salim, S., Hornstein, S. D., Tanner, A., Lu, J. R., Morris, M., Becklin, E. E., Duchêne, G., 2005. Stellar Orbits around the Galactic Center Black Hole. *ApJ* 620, 744–757. ► See p. 13, 38, 39, 45, 46, 49, 76, 78, 80
- Ghez, A. M., Wright, S. A., Matthews, K., Thompson, D., Le Mignant, D., Tanner, A., Hornstein, S. D., Morris, M., Becklin, E. E., Soifer, B. T., 2004. Variable Infrared Emission from the Supermassive Black Hole at the Center of the Milky Way. *ApJ* 601, L159–L162. ► See p. 33, 37
- Ghez, A. M., et al., 2003b. The First Measurement of Spectral Lines in a Short-Period Star Bound to the Galaxy’s Central Black Hole: A Paradox of Youth. *ApJ* 586, L127–L131. ► See p. 13, 31, 32, 39, 47, 75, 76
- Gingold, R. A., Monaghan, J. J., 1977. Smoothed particle hydrodynamics - Theory and application to non-spherical stars. *MNRAS* 181, 375–389. ► See p. 65

- Glampedakis, K., 2005. Extreme mass ratio inspirals: LISA's unique probe of black hole gravity. *Classical and Quantum Gravity* 22, 605–+. ► See p. 70
- Gnedin, O. Y., Primack, J. R., 2004. Dark Matter Profile in the Galactic Center. *Physical Review Letters* 93 (6), 061302–+. ► See p. 17, 43
- Goldwurm, A., Brion, E., Goldoni, P., Ferrando, P., Daigne, F., Decourchelle, A., Warwick, R. S., Predehl, P., 2003. A New X-Ray Flare from the Galactic Nucleus Detected with the XMM-Newton Photon Imaging Cameras. *ApJ* 584, 751–757. ► See p. 65
- Gomboc, A., Čadež, A., 2005. Effects of a Black Hole's Gravitational Field on the Luminosity of a Star during a Close Encounter. *ApJ* 625, 278–290. ► See p. 57, 61
- Gondolo, P., Silk, J., 1999. Dark Matter Annihilation at the Galactic Center. *Physical Review Letters* 83, 1719–1722. ► See p. 43
- Goodman, J., 2003. Self-gravity and quasi-stellar object discs. *MNRAS* 339, 937–948. ► See p. 79
- Goodman, J., Paczynski, B., 2005. On the nature of the S stars in the Galactic Center. [arXiv:astro-ph/0504079](https://arxiv.org/abs/astro-ph/0504079). ► See p. 82
- Goodman, J., Tan, J. C., 2004. Supermassive Stars in Quasar Disks. *ApJ* 608, 108–118. ► See p. 79
- Gould, A., Loeb, A., 1992. Discovering planetary systems through gravitational microlenses. *ApJ* 396, 104–114. ► See p. 24, 56
- Gould, A., Popowski, P., 1998. Systematics of RR Lyrae Statistical Parallax. III. Apparent Magnitudes and Extinctions. *ApJ* 508, 844–853. ► See p. 48
- Gould, A., Quillen, A. C., 2003. Sagittarius A* Companion S0-2: A Probe of Very High Mass Star Formation. *ApJ* 592, 935–940. ► See p. 81
- Gray, D. F., 1992. The observation and analysis of stellar photospheres. Cambridge Astrophysics Series, Cambridge: Cambridge University Press, 1992, 2nd ed., ISBN 0521403200. ► See p. 27
- Gürkan, M. A., Freitag, M., Rasio, F. A., 2004. Formation of Massive Black Holes in Dense Star Clusters. I. Mass Segregation and Core Collapse. *ApJ* 604, 632–652. ► See p. 81
- Haller, J. W., Rieke, M. J., Rieke, G. H., Tamblyn, P., Close, L., Melia, F., 1996. Stellar Kinematics and the Black Hole in the Galactic Center. *ApJ* 456, 194–+. ► See p. 10, 24, 31
- Hansen, B. M. S., Milosavljević, M., 2003. The Need for a Second Black Hole at the Galactic Center. *ApJ* 593, L77–L80. ► See p. 44, 45, 77, 80, 81
- Heggie, D., Hut, P., 2003. The Gravitational Million-Body Problem: A Multidisciplinary Approach to Star Cluster Dynamics. Cambridge University Press, 2003, 372 pp. ► See p. 13
- Herrnstein, R. M., Ho, P. T. P., 2005. The Nature of the Molecular Environment within 5 Parsecs of the Galactic Center. *ApJ* 620, 287–307. ► See p. 64
- Hills, J. G., 1975. Possible power source of Seyfert galaxies and QSOs. *Nature* 254, 295–298. ► See p. 56, 59, 73
- Hills, J. G., 1988. Hyper-velocity and tidal stars from binaries disrupted by a massive Galactic black hole. *Nature* 331, 687–689. ► See p. 45
- Hils, D., Bender, P. L., 1995. Gradual approach to coalescence for compact stars orbiting massive black holes. *ApJ* 445, L7–L10. ► See p. 67, 70
- Hopman, C., Alexander, T., 2005. The orbital statistics of stellar inspiral and relaxation near a massive black hole: characterizing gravitational wave sources. *ApJ* In press, [arXiv:astro-ph/0503672](https://arxiv.org/abs/astro-ph/0503672). ► See p. 59, 67, 69, 70
- Hopman, C., Portegies Zwart, S. F., Alexander, T., 2004. Ultraluminous X-Ray Sources as Intermediate-Mass Black Holes Fed by Tidally Captured Stars. *ApJ* 604, L101–L104. ► See p. 6, 67, 71
- Ivanov, P. B., 2002. On the formation rate of close binaries consisting of a super-massive black hole and a white dwarf. *MNRAS* 336, 373–381. ► See p. 61, 67, 70

- Ivanov, P. B., Novikov, I. D., 2001. A New Model of a Tidally Disrupted Star. *ApJ* 549, 467–482. ► See p. 61
- Ivanov, P. B., Polnarev, A. G., Saha, P., 2005. The tidal disruption rate in dense galactic cusps containing a supermassive binary black hole. *MNRAS* 358, 1361–1378. ► See p. 43
- Jackson, J. M., Geis, N., Genzel, R., Harris, A. I., Madden, S., Poglitsch, A., Stacey, G. J., Townes, C. H., 1993. Neutral gas in the central 2 parsecs of the Galaxy. *ApJ* 402, 173–184. ► See p. 77
- Jaroszynski, M., 1999. Prospects for the Determination of Star Orbits near the Galactic Center. *ApJ* 521, 591–596. ► See p. 40
- Jaroszynski, M., 1998a. Gravitational Lensing and Proper Motions of Stars Surrounding the Galactic Center. *Acta Astronomica* 48, 413–429. ► See p. 50, 55
- Jaroszynski, M., 1998b. Relativistic Effects in Proper Motions of Stars Surrounding the Galactic Center. *Acta Astronomica* 48, 653–665. ► See p. 47, 49
- Jaroszynski, M., 2000. Stellar Kinematics Near the Galactic Center – Possible Test for a Binary Black Hole. *Acta Astronomica* 50, 67–78. ► See p. 44
- Kaaret, P., Prestwich, A. H., Zezas, A., Murray, S. S., Kim, D.-W., Kilgard, R. E., Schlegel, E. M., Ward, M. J., 2001. Chandra High-Resolution Camera observations of the luminous X-ray source in the starburst galaxy M82. *MNRAS* 321, L29–L32. ► See p. 6
- Kent, S. M., 1992. Galactic structure from the spacelab infrared telescope. III - A dynamical model for the Milky Way bulge. *ApJ* 387, 181–188. ► See p. 23
- Khokhlov, A., Melia, F., 1996. Powerful Ejection of Matter from Tidally Disrupted Stars near Massive Black Holes and a Possible Application to Sagittarius A East. *ApJ* 457, L61. ► See p. 61, 62, 64
- Khokhlov, A., Novikov, I. D., Pethick, C. J., 1993. Strong Effects during Close Encounters of a Star with a Massive Black Hole. *ApJ* 418, 181. ► See p. 61, 66
- Kim, S. S., Figer, D. F., Morris, M., 2004. Dynamical friction on galactic center clusters with an intermediate mass black hole. *ApJ* 617, L123–L126. ► See p. 81
- Kim, S. S., Morris, M., 2003. Dynamical Friction on Star Clusters near the Galactic Center. *ApJ* 597, 312–322. ► See p. 80
- Kochanek, C. S., 1994. The aftermath of tidal disruption: The dynamics of thin gas streams. *ApJ* 422, 508–520. ► See p. 57, 61
- Komossa, S., 2002. Ludwig Biermann Award Lecture: X-ray Evidence for Supermassive Black Holes at the Centers of Nearby, Non-Active Galaxies. *Reviews of Modern Astronomy* 15, 27–+, [arXiv:astro-ph/0209007](https://arxiv.org/abs/astro-ph/0209007). ► See p. 61, 64
- Kopeikin, S. M., Ozernoy, L. M., 1999. Post-Newtonian Theory for Precision Doppler Measurements of Binary Star Orbits. *ApJ* 523, 771–785. ► See p. 48
- Kormendy, J., Richstone, D., 1995. Inward Bound—The Search For Supermassive Black Holes In Galactic Nuclei. *ARA&A* 33, 581. ► See p. 3
- Kosack, K., et al., 2004. TeV Gamma-Ray Observations of the Galactic Center. *ApJ* 608, L97–L100. ► See p. 43
- Koyama, K., Maeda, Y., Sonobe, T., Takeshima, T., Tanaka, Y., Yamauchi, S., 1996. ASCA View of Our Galactic Center: Remains of Past Activities in X-Rays? *PASJ* 48, 249–255. ► See p. 65
- Krabbe, A., et al., 1995. The Nuclear Cluster of the Milky Way: Star Formation and Velocity Dispersion in the Central 0.5 Parsec. *ApJ* 447, L95–L98. ► See p. 10, 13, 31, 76, 77, 79
- Kumar, P., Quataert, E. J., 1998. On the Orbital Decay of the PSR J0045-7319 Binary. *ApJ* 493, 412–+. ► See p. 28
- Lacy, J. H., Townes, C. H., Geballe, T. R., Hollenbach, D. J., 1980. Observations of the motion and distribution of the ionized gas in the central parsec of the Galaxy. II. *ApJ* 241, 132–146. ► See p. 31
- Lacy, J. H., Townes, C. H., Hollenbach, D. J., 1982. The nature of the central parsec of the Galaxy. *ApJ*

- 262, 120–134. ► See p. [25](#), [61](#)
- Laguna, P., Miller, W. A., Zurek, W. H., Davies, M. B., 1993. Tidal disruptions by supermassive black holes - Hydrodynamic evolution of stars on a Schwarzschild background. *ApJ* 410, L83–L86. ► See p. [57](#), [61](#), [66](#), [68](#)
- Lai, D., Rasio, F. A., Shapiro, S. L., 1993. Collisions and close encounters between massive main-sequence stars. *ApJ* 412, 593–611. ► See p. [30](#)
- Landau, L. D., Lifshitz, E. M., 1969. *Mechanics*. Course of Theoretical Physics, Oxford: Pergamon Press, 1969, 2nd ed. ► See p. [43](#)
- Lauer, T. R., Faber, S. M., Ajhar, E. A., Grillmair, C. J., Scowen, P. A., 1998. M32 +/- 1. *AJ* 116, 2263–2286. ► See p. [6](#)
- Laun, F., Merritt, D., 2004. Brownian Motion of Black Holes in Dense Nuclei. *ApJ* Submitted, [arXiv:astro-ph/0408029](#). ► See p. [44](#)
- Lazio, T. J. W., Cordes, J. M., Lang, C. C., Gotthelf, E. V., Wang, Q. D., 2003. Radio Pulsars in the Galactic Center. *Astronomische Nachrichten Supplement* 324, 333–336. ► See p. [24](#)
- Lee, M. H., Goodman, J., 1989. Adiabatic growth of a black hole in a rotating stellar system. *ApJ* 343, 594–601. ► See p. [17](#)
- Leonard, P. J. T., Livio, M., 1995. The Rotational Rates of Blue Stragglers Produced by Physical Stellar Collisions. *ApJ* 447, L121+. ► See p. [77](#)
- Leonard, P. J. T., Merritt, D., 1989. The mass of the open star cluster M35 as derived from proper motions. *ApJ* 339, 195–208. ► See p. [34](#), [35](#), [39](#)
- Levin, Y., Beloborodov, A. M., 2003. Stellar Disk in the Galactic Center: A Remnant of a Dense Accretion Disk? *ApJ* 590, L33–L36. ► See p. [11](#), [12](#), [49](#), [79](#)
- Levin, Y., Wu, A. S. P., Thommes, E. W., 2005. Intermediate-mass Black Hole and stellar orbits in the Galactic Center. *ApJ* Submitted, [arXiv:astro-ph/0502143](#). ► See p. [80](#)
- Lightman, A. P., Shapiro, S. L., 1977. The distribution and consumption rate of stars around a massive, collapsed object. *ApJ* 211, 244–262. ► See p. [56](#), [59](#), [60](#)
- Liszt, H. S., 2003. The velocity field of ionized gas near Sgr A*. *A&A* 408, 1009–1014. ► See p. [77](#)
- Livne, E., Tuchman, Y., 1988. The dynamical consequences of a red giant-main-sequence star collision. *ApJ* 332, 271–281. ► See p. [25](#)
- Loeb, A., 2003. Apparent Deviations from Keplerian Acceleration for Stars Around the Supermassive Black Hole at the Galactic Center, [arXiv:astro-ph/0309716](#). ► See p. [47](#)
- Loeb, A., 2004. Direct feeding of the black hole at the Galactic Centre with radial gas streams from close-in stellar winds. *MNRAS* 350, 725–728. ► See p. [82](#)
- Loeb, A., Ulmer, A., 1997. Optical Appearance of the Debris of a Star Disrupted by a Massive Black Hole. *ApJ* 489, 573–+. ► See p. [61](#), [63](#)
- Lombardi, J. C., Rasio, F. A., Shapiro, S. L., 1995. On blue straggler formation by direct collisions of main sequence stars. *ApJ* 445, L117–L120. ► See p. [77](#)
- Lombardi, J. C., Rasio, F. A., Shapiro, S. L., 1996. Collisions of Main-Sequence Stars and the Formation of Blue Stragglers in Globular Clusters. *ApJ* 468, 797–+. ► See p. [77](#)
- Lucy, L. B., 1977. A numerical approach to the testing of the fission hypothesis. *AJ* 82, 1013–1024. ► See p. [65](#)
- Luminet, J.-P., Marck, J.-A., 1985. Tidal squeezing of stars by Schwarzschild black holes. *MNRAS* 212, 57–75. ► See p. [66](#)
- Maeda, Y., Baganoff, F. K., Feigelson, E. D., Morris, M., Bautz, M. W., Brandt, W. N., Burrows, D. N., Doty, J. P., Garmire, G. P., Pravdo, S. H., Ricker, G. R., Townsley, L. K., 2002. A Chandra Study of Sagittarius A East: A Supernova Remnant Regulating the Activity of Our Galactic Center? *ApJ* 570, 671–687. ► See p. [64](#)

- Maeder, A., Meynet, G., 2000. The Evolution of Rotating Stars. *ARA&A* 38, 143–190. ► See p. 27
- Magorrian, J., Tremaine, S., 1999. Rates of tidal disruption of stars by massive central black holes. *MNRAS* 309, 447–460. ► See p. 59, 60, 72
- Magorrian, J., et al., 1998. The Demography of Massive Dark Objects in Galaxy Centers. *AJ* 115, 2285–2305. ► See p. 3
- Maillard, J. P., Paumard, T., Stolovy, S. R., Rigaut, F., 2004. The nature of the Galactic Center source IRS 13 revealed by high spatial resolution in the infrared. *A&A* 423, 155–167. ► See p. 12, 44, 81
- Maoz, E., 1998. Dynamical Constraints on Alternatives to Supermassive Black Holes in Galactic Nuclei. *ApJ* 494, L181–L184. ► See p. 40, 41
- Marr, J. M., Wright, M. C. H., Backer, D. C., 1993. HCO(+), H(C-13)N, and H(C-12)N aperture synthesis observations of the circumnuclear ring in the Galactic center. *ApJ* 411, 667–673. ► See p. 77
- Marshall, J., Lasenby, A. N., Harris, A. I., 1995. HCN observations of the circumnuclear disc in the Galactic Centre. *MNRAS* 277, 594–608. ► See p. 77
- McGinn, M. T., Sellgren, K., Becklin, E. E., Hall, D. N. B., 1989. Stellar kinematics in the Galactic center. *ApJ* 338, 824–840. ► See p. 10, 31
- McMillan, S. L. W., McDermott, P. N., Taam, R. E., 1987. The formation and evolution of tidal binary systems. *ApJ* 318, 261–277. ► See p. 71
- Melia, F., 1992. An accreting black hole model for Sagittarius A. *ApJ* 387, L25–L28. ► See p. 82
- Melia, F., Falcke, H., 2001. The Supermassive Black Hole at the Galactic Center. *ARA&A* 39, 309–352. ► See p. 6
- Menou, K., Quataert, E., 2001. Activity From Tidal Disruptions in Galactic Nuclei. *ApJ* 562, L137–L140. ► See p. 61, 63, 64
- Menten, K. M., Reid, M. J., Eckart, A., Genzel, R., 1997. The Position of SGR A star: Accurate Alignment of the Radio and Infrared Reference Frames at the Galactic Center. *ApJ* 475, L111+. ► See p. 32, 37
- Merritt, D., 2004a. A Note on Gravitational Brownian Motion. [arXiv:astro-ph/0405351](https://arxiv.org/abs/astro-ph/0405351). ► See p. 44
- Merritt, D., 2004b. Evolution of the Dark Matter Distribution at the Galactic Center. *Physical Review Letters* 92 (20), 201304+. ► See p. 43
- Merritt, D., Milosavljevic, M., 2004. Massive Black Hole Binary Evolution, *Living Reviews in Relativity*, in press; [arXiv:astro-ph/0410364](https://arxiv.org/abs/astro-ph/0410364). ► See p. 6, 44
- Merritt, D., Poon, M. Y., 2004. Chaotic Loss Cones and Black Hole Fueling. *ApJ* 606, 788–798. ► See p. 60
- Merritt, D., Tremblay, B., 1994. Nonparametric estimation of density profiles. *AJ* 108, 514–537. ► See p. 20
- Meylan, G., Mayor, M., 1991. Studies of dynamical properties of globular clusters. VI - The high-concentration cluster NGC 6397. *A&A* 250, 113–126. ► See p. 10
- Mezger, P. G., Zylka, R., Philipp, S., Launhardt, R., 1999. The nuclear bulge of the Galaxy. II. The K band luminosity function of the central 30 PC. *A&A* 348, 457–465. ► See p. 7
- Mezger, P. G., Zylka, R., Salter, C. J., Wink, J. E., Chini, R., Kreysa, E., Tuffs, R., 1989. Continuum observations of SGR A at mm/submm wavelengths. *A&A* 209, 337–348. ► See p. 64
- Miller, C. M., Colbert, E. J. M., 2004. Intermediate-Mass Black Holes. *International Journal of Modern Physics D* 13, 1–64. ► See p. 6
- Miller, G. E., Scalo, J. M., 1979. The initial mass function and stellar birthrate in the solar neighborhood. *ApJS* 41, 513–547. ► See p. 10
- Milosavljević, M., Loeb, A., 2004. The Link between Warm Molecular Disks in Maser Nuclei and Star

- Formation near the Black Hole at the Galactic Center. *ApJ* 604, L45–L48. ► See p. 79
- Milosavljević, M., Merritt, D., Rest, A., van den Bosch, F. C., 2002. Galaxy cores as relics of black hole mergers. *MNRAS* 331, L51–L55. ► See p. 18, 44
- Miralda-Escudé, J., Gould, A., 2000. A Cluster of Black Holes at the Galactic Center. *ApJ* 545, 847–853. ► See p. 22, 23, 24, 56, 58, 70
- Monaghan, J. J., 1992. Smoothed particle hydrodynamics. *ARA&A* 30, 543–574. ► See p. 65
- Morris, M., 1993. Massive star formation near the Galactic center and the fate of the stellar remnants. *ApJ* 408, 496–506. ► See p. 22, 23, 28, 30, 78
- Morris, M., Ghez, A. M., Becklin, E. E., 1999. The galactic center black hole: clues for the evolution of black holes in galactic nuclei. *Advances in Space Research* 23, 959–968. ► See p. 78
- Morris, M., Serabyn, E., 1996. The Galactic Center Environment. *ARA&A* 34, 645–702. ► See p. 6
- Mouawad, N., Eckart, A., Pfalzner, S., Schödel, R., Moutaka, J., Spurzem, R., 2005. Weighing the cusp at the Galactic Centre. *Astronomische Nachrichten* 326, 83–95. ► See p. 24, 43
- Muno, M. P., Pfahl, E., Baganoff, F. K., Brandt, W. N., Ghez, A., Lu, J., Morris, M. R., 2005. An Overabundance of Transient X-Ray Binaries within 1 Parsec of the Galactic Center. *ApJ* 622, L113–L116. ► See p. 24, 85
- Munyanza, F., Tsiklauri, D., Viollier, R. D., 1998. Sagittarius A*: A Supermassive Black Hole or a Spatially Extended Object? *ApJ* 509, L105–L108. ► See p. 42
- Munyanza, F., Viollier, R. D., 2002. The Motion of Stars near the Galactic Center: A Comparison of the Black Hole and Fermion Ball Scenarios. *ApJ* 564, 274–283. ► See p. 42
- Murakami, H., Koyama, K., Sakano, M., Tsujimoto, M., Maeda, Y., 2000. ASCA Observations of the Sagittarius B2 Cloud: An X-Ray Reflection Nebula. *ApJ* 534, 283–290. ► See p. 65
- Murakami, H., Koyama, K., Tsujimoto, M., Maeda, Y., Sakano, M., 2001. ASCA Discovery of Diffuse 6.4 KEV Emission near the Sagittarius C Complex: A New X-Ray Reflection Nebula. *ApJ* 550, 297–300. ► See p. 65
- Murphy, B. W., Cohn, H. N., Durisen, R. H., 1991. Dynamical and luminosity evolution of active galactic nuclei - Models with a mass spectrum. *ApJ* 370, 60–77. ► See p. 17, 72, 75
- Najarro, F., Krabbe, A., Genzel, R., Lutz, D., Kudritzki, R. P., Hillier, D. J., 1997. Quantitative spectroscopy of the HeI cluster in the Galactic center. *A&A* 325, 700–708. ► See p. 11
- Narayan, R., 2002. Why Do AGN Lighthouses Switch Off? In: *Lighthouses of the Universe: The Most Luminous Celestial Objects and Their Use for Cosmology Proceedings of the MPA/ESO*, p. 405. pp. 405–+. ► See p. 3
- Narayan, R., Igumenshchev, I. V., Abramowicz, M. A., 2000. Self-similar Accretion Flows with Convection. *ApJ* 539, 798–808. ► See p. 62
- Narayan, R., Yi, I., 1994. Advection-dominated accretion: A self-similar solution. *ApJ* 428, L13–L16. ► See p. 62
- Narayan, R., Yi, I., 1995. Advection-dominated Accretion: Underfed Black Holes and Neutron Stars. *ApJ* 452, 710–+. ► See p. 62
- Narayan, R., Yi, I., Mahadevan, R., 1995. Explaining the Spectrum of SAGITTARIUS-A* with a Model of an Accreting Black-Hole. *Nature* 374, 623–+. ► See p. 62
- Navarro, J. F., Frenk, C. S., White, S. D. M., 1996. The Structure of Cold Dark Matter Halos. *ApJ* 462, 563–+. ► See p. 43
- Nayakshin, S., Cuadra, J., 2005. A self-gravitating accretion disk in Sgr A* a few million years ago: Is Sgr A* a failed quasar? *A&A* 437, 437–445. ► See p. 79
- Nayakshin, S., Cuadra, J., Sunyaev, R., 2004. X-ray flares from Sgr A*: Star-disk interactions? *A&A* 413, 173–188. ► See p. 75

- Nayakshin, S., Sunyaev, R., 2003. Close stars and an inactive accretion disc in Sgr A*: eclipses and flares. *MNRAS* 343, L15–L19. ► See p. 75
- Nolthenius, R. A., Katz, J. I., 1982. The passage of a star by a massive black hole. *ApJ* 263, 377–385. ► See p. 61
- Novikov, I. D., Pethick, C. J., Polnarev, A. G., 1992. Tidal capture of stars by a massive black hole. *MNRAS* 255, 276–284. ► See p. 72
- Nusser, A., Broadhurst, T., 2004. Monitoring lensed starlight emitted close to the Galactic centre. *MNRAS* 355, L6–L8. ► See p. 55
- Olling, R. P., Merrifield, M. R., 2001. Luminous and dark matter in the Milky Way. *MNRAS* 326, 164–180. ► See p. 39
- Oppenheimer, J. R., Volkoff, G. M., 1939. On Massive Neutron Cores. *Physical Review* 55, 374–381. ► See p. 42
- Ostriker, J. P., 1983. Viscous drag on an accretion disk due to an embedded stellar system. *ApJ* 273, 99–104. ► See p. 75
- Ott, T., Eckart, A., Genzel, R., 1999. Variable and Embedded Stars in the Galactic Center. *ApJ* 523, 248–264. ► See p. 77
- Ott, T., et al., 2003. Inward bound: studying the Galactic Centre with NAOS/CONICA. *The Messenger* 111, 1–8. ► See p. 34
- Ouellette, J. A., Pritchett, C. J., 1998. The Evolution of Blue Stragglers Formed via Stellar Collisions. *AJ* 115, 2539–2550. ► See p. 77
- Paczynski, B., 1978. A model of selfgravitating accretion disk. *Acta Astronomica* 28, 91–109. ► See p. 79
- Page, K. L., Schartel, N., Turner, M. J. L., O’Brien, P. T., 2004. XMM-Newton observations of seven soft X-ray excess quasi-stellar objects. *MNRAS* 352, 523–534. ► See p. 46
- Paresce, F., Delplancke, F., Derie, F., Glindemann, A., Richichi, A., Tarenghi, M., 2003. Scientific objectives of ESO’s PRIMA facility. In: *Interferometry for Optical Astronomy II*. Edited by Wesley A. Traub. *Proceedings of the SPIE*, Volume 4838, pp. 486–495 (2003). pp. 486–495. ► See p. 9
- Paumard, T., 2004. Census of the Galactic Centre early-type stars using spectro-imagery. In: Chalabaev, A., Fukui, T., Montmerle, T., J., T. (Eds.), *Proc XXXIXth Moriond meeting: Young Local Universe*. Editions Frontieres, Paris, in press, [arXiv:astro-ph/0407189](https://arxiv.org/abs/astro-ph/0407189). ► See p. 10, 76, 77
- Paumard, T., Maillard, J.-P., Morris, M., 2004. Kinematic and structural analysis of the <ASTROBJ>Minispiral</ASTROBJ> in the Galactic Center from BEAR spectro-imagery. *A&A* 426, 81–96. ► See p. 77
- Paumard, T., Maillard, J. P., Morris, M., Rigaut, F., 2001. New results on the helium stars in the galactic center using BEAR spectro-imagery. *A&A* 366, 466–480. ► See p. 76
- Pessah, M., Melia, F., 2003. Diffuse X-Rays from a Distributed Component of Dark Matter Surrounding Sagittarius A*. *ApJ* 585, L29–L32. ► See p. 24
- Peters, P. C., 1964. Gravitational Radiation and the Motion of Two Point Masses. *Physical Review* 136, 1224–1232. ► See p. 45, 69
- Petters, A. O., 2003. On relativistic corrections to microlensing effects: applications to the Galactic black hole. *MNRAS* 338, 457–464. ► See p. 55
- Pfahl, E., Loeb, A., 2004. Probing the Spacetime around Sagittarius A* with Radio Pulsars. *ApJ* 615, 253–258. ► See p. 48
- Philipp, S., Zylka, R., Mezger, P. G., Duschl, W. J., Herbst, T., Tuffs, R. J., 1999. The nuclear bulge. I. K band observations of the central 30 PC. *A&A* 348, 768–782. ► See p. 7
- Phinney, E. S., 1989. Manifestations of a Massive Black Hole in the Galactic Center. In: *IAU Symp. 136: The Center of the Galaxy*. pp. 543–+. ► See p. 25, 61

- Pichon, B., 1985. Helium detonation in pancake stars. *A&A* 145, 387–390. ► See p. 67
- Podsiadlowski, P., 1996. The response of tidally heated stars. *MNRAS* 279, 1104. ► See p. 71
- Podsiadlowski, P., Rappaport, S., Pfahl, E. D., 2002. Evolutionary Sequences for Low- and Intermediate-Mass X-Ray Binaries. *ApJ* 565, 1107–1133. ► See p. 25
- Poon, M. Y., Merritt, D., 2002. Triaxial Black Hole Nuclei. *ApJ* 568, L89–L92. ► See p. 60
- Portegies Zwart, S. F., Baumgardt, H., Hut, P., Makino, J., McMillan, S. L. W., 2004. Formation of massive black holes through runaway collisions in dense young star clusters. *Nature* 428, 724–726. ► See p. 6, 80
- Portegies Zwart, S. F., McMillan, S. L. W., Gerhard, O., 2003. The Origin of IRS 16: Dynamically Driven In-Spiral of a Dense Star Cluster to the Galactic Center? *ApJ* 593, 352–357. ► See p. 80
- Predehl, P., Costantini, E., Hasinger, G., Tanaka, Y., 2003. XMM-Newton observation of the galactic centre - evidence against the X-ray reflection nebulae model? *Astronomische Nachrichten* 324, 73–76. ► See p. 65
- Press, W. H., Teukolsky, S. A., 1977. On formation of close binaries by two-body tidal capture. *ApJ* 213, 183–192. ► See p. 27
- Preto, M., Merritt, D., Spurzem, R., 2004. N-Body Growth of a Bahcall-Wolf Cusp around a Black Hole. *ApJ* 613, L109–L112. ► See p. 85
- Quataert, E., 2003. Radiatively Inefficient Accretion Flow Models of Sgr A*. *Astronomische Nachrichten Supplement* 324, 435–443. ► See p. 82
- Quataert, E., Gruzinov, A., 2000. Convection-dominated Accretion Flows. *ApJ* 539, 809–814. ► See p. 62
- Quinlan, G. D., Hernquist, L., Sigurdsson, S., 1995. Models of Galaxies with Central Black Holes: Adiabatic Growth in Spherical Galaxies. *ApJ* 440, 554–+. ► See p. 17, 19
- Rasio, F. A., Shapiro, S. L., 1990. Encounters between compact stars and red giants in dense stellar systems. *ApJ* 354, 201–210. ► See p. 25
- Rasio, F. A., Shapiro, S. L., 1991. Collisions of giant stars with compact objects - Hydrodynamical calculations. *ApJ* 377, 559–580. ► See p. 25
- Rauch, K. P., Ingalls, B., 1998. Resonant tidal disruption in galactic nuclei. *MNRAS* 299, 1231–1241. ► See p. 60
- Rauch, K. P., Tremaine, S., 1996. Resonant relaxation in stellar systems. *New Astronomy* 1, 149–170. ► See p. 14, 60
- Rees, M. J., 1988. Tidal disruption of stars by black holes of 10 to the 6th–10 to the 8th solar masses in nearby galaxies. *Nature* 333, 523–528. ► See p. 56, 58, 61, 62, 63
- Rees, M. J., Phinney, E. S., Begelman, M. C., Blandford, R. D., 1982. Ion-supported tori and the origin of radio jets. *Nature* 295, 17–21. ► See p. 62
- Reid, M. J., 1993. The distance to the center of the Galaxy. *ARA&A* 31, 345–372. ► See p. 9, 34, 39
- Reid, M. J., Brunthaler, A., 2004. The Proper Motion of Sagittarius A*. II. The Mass of Sagittarius A*. *ApJ* 616, 872–884. ► See p. 38, 41, 44, 45
- Reid, M. J., Menten, K. M., Genzel, R., Ott, T., Schödel, R., Brunthaler, A., 2003a. The Position, Motion, and Mass of Sgr A*. *Astronomische Nachrichten Supplement* 324, 505–511. ► See p. 40
- Reid, M. J., Menten, K. M., Genzel, R., Ott, T., Schödel, R., Eckart, A., 2003b. The Position of Sagittarius A*. II. Accurate Positions and Proper Motions of Stellar SiO Masers near the Galactic Center. *ApJ* 587, 208–220. ► See p. 32
- Reid, M. J., Readhead, A. C. S., Vermeulen, R. C., Treuhaft, R. N., 1999. The Proper Motion of Sagittarius A*. I. First VLBA Results. *ApJ* 524, 816–823. ► See p. 40
- Revnivtsev, M. G., Churazov, E. M., Sazonov, S. Y., Sunyaev, R. A., Lutovinov, A. A., Gilfanov, M. R.,

- Vikhlinin, A. A., Shtykovsky, P. E., Pavlinsky, M. N., 2004. Hard X-ray view of the past activity of Sgr A* in a natural Compton mirror. *A&A* 425, L49–L52. ► See p. 65
- Rieke, G. H., Rieke, M. J., 1988. Stellar velocities and the mass distribution in the Galactic center. *ApJ* 330, L33–L37. ► See p. 21
- Rieke, G. H., Rieke, M. J., Paul, A. E., 1989. Origin of the excitation of the galactic center. *ApJ* 336, 752–761. ► See p. 4, 9
- Rockefeller, G., Fryer, C. L., Melia, F., Warren, M. S., 2004. Diffuse X-Rays from the Inner 3 Parsecs of the Galaxy. *ApJ* 604, 662–670. ► See p. 82
- Rubilar, G. F., Eckart, A., 2001. Periastron shifts of stellar orbits near the Galactic Center. *A&A* 374, 95–104. ► See p. 47, 49
- Sakano, M., Warwick, R. S., Decourchelle, A., Predehl, P., 2004. XMM-Newton observations of Sagittarius A East. *MNRAS* 350, 129–139. ► See p. 64
- Salim, S., Gould, A., 1999. Sagittarius A* “Visual Binaries”: A Direct Measurement of the Galactocentric Distance. *ApJ* 523, 633–641. ► See p. 36, 38, 40
- Sanders, R. H., 1998. The circumnuclear material in the Galactic Centre - A clue to the accretion process. *MNRAS* 294, 35–+. ► See p. 79
- Sandquist, E. L., Bolte, M., Hernquist, L., 1997. Composition Mixing during Blue Straggler Formation and Evolution. *ApJ* 477, 335–+. ► See p. 77
- Schödel, R., Eckart, A., Iserlohe, C., Genzel, R., Ott, T., 2005. A Black Hole in the Galactic Center Complex IRS 13E? *ApJ* 625, L111–L114. ► See p. 12, 44, 81
- Schaller, G., Schaerer, D., Meynet, G., Maeder, A., 1992. New grids of stellar models from 0.8 to 120 solar masses at $Z = 0.020$ and $Z = 0.001$. *A&AS* 96, 269–331. ► See p. 9, 10, 13, 55
- Schneider, P., Ehlers, J., Falco, E. E., 1992. Gravitational Lenses. Gravitational Lenses, XIV, 560 pp. 112 figs.. Springer-Verlag Berlin Heidelberg New York. Also Astronomy and Astrophysics Library. ► See p. 50
- Schödel, R., Ott, T., Genzel, R., Eckart, A., Mouawad, N., Alexander, T. E., 2003. Stellar Dynamics in the Central Arcsecond of Our Galaxy. *ApJ* 596, 1015–1034. ► See p. 13, 14, 15, 18, 34, 36, 41, 44, 76
- Schödel, R., et al., 2002. A star in a 15.2-year orbit around the supermassive black hole at the centre of the Milky Way. *Nature* 419, 694–696. ► See p. 31, 39, 42, 49
- Scoville, N., Stolovy, S. R., Christopher, M., 2003. The ISM and stellar distributions near Sgr A*. *Astronomische Nachrichten Supplement* 324, 591–596. ► See p. 20
- Scoville, N. Z., 2004. Stellar Distributions Near SgrA* and the Host Galaxies of Bright QSOs. In: *Coevolution of Black Holes and Galaxies*. ► See p. 21
- Sellgren, K., McGinn, M. T., Becklin, E. E., Hall, D. N., 1990. Velocity dispersion and the stellar population in the central 1.2 parsecs of the Galaxy. *ApJ* 359, 112–120. ► See p. 20, 25, 31
- Serabyn, E., Morris, M., 1996. Sustained star formation in the central stellar cluster of the Milky Way. *Nature* 382, 602–604. ► See p. 7, 20
- Shakura, N. I., Sunyaev, R. A., 1973. Black holes in binary systems. Observational appearance. *A&A* 24, 337–355. ► See p. 82
- Shapiro, S. L., Teukolsky, S. A., 1983. Black holes, white dwarfs, and neutron stars: The physics of compact objects. Research supported by the National Science Foundation. New York, Wiley-Interscience, 1983, 663 p. ► See p. 45, 62, 70
- Shukla, H., Yun, M. S., Scoville, N. Z., 2004. Dense, Ionized, and Neutral Gas Surrounding Sagittarius A*. *ApJ* 616, 231–246. ► See p. 77
- Sigurdsson, S., 1997. Estimating the detectable rate of capture of stellar mass black holes by massive central black holes in normal galaxies. *Classical and Quantum Gravity* 14, 1425–1429. ► See p. 67

- Sigurdsson, S., 2003. The loss cone: past, present and future. *Classical and Quantum Gravity* 20, 45–. ► See p. 67, 70
- Sigurdsson, S., Rees, M. J., 1997. Capture of stellar mass compact objects by massive black holes in galactic cusps. *MNRAS* 284, 318–326. ► See p. 67, 70
- Sills, A., Lombardi, J. C., Baily, C. D., Demarque, P., Rasio, F. A., Shapiro, S. L., 1997. Evolution of Stellar Collision Products in Globular Clusters. I. Head-on Collisions. *ApJ* 487, 290–+. ► See p. 77
- Soltan, A., 1982. Masses of quasars. *MNRAS* 200, 115–122. ► See p. 3
- Sternberg, A., Hoffmann, T. L., Pauldrach, A. W. A., 2003. Ionizing Photon Emission Rates from O- and Early B-Type Stars and Clusters. *ApJ* 599, 1333–1343. ► See p. 10
- Sunyaev, R., Churazov, E., 1998. Equivalent width, shape and proper motion of the iron fluorescent line emission from molecular clouds as an indicator of the illuminating source X-ray flux history. *MNRAS* 297, 1279–1291. ► See p. 65
- Sunyaev, R. A., Markevitch, M., Pavlinsky, M., 1993. The center of the Galaxy in the recent past - A view from GRANAT. *ApJ* 407, 606–610. ► See p. 65
- Syer, D., Clarke, C. J., Rees, M. J., 1991. Star-disc interactions near a massive black hole. *MNRAS* 250, 505–512. ► See p. 75
- Syer, D., Ulmer, A., 1999. Tidal disruption rates of stars in observed galaxies. *MNRAS* 306, 35–42. ► See p. 59, 60
- Tamblyn, P., Rieke, G. H., Hanson, M. M., Close, L. M., McCarthy, D. W., Rieke, M. J., 1996. The Peculiar Population of Hot Stars at the Galactic Center. *ApJ* 456, 206–+. ► See p. 10
- Tanner, A., Ghez, A. M., Morris, M., Becklin, E. E., Cotera, A., Ressler, M., Werner, M., Wizinowich, P., 2002. Spatially Resolved Observations of the Galactic Center Source IRS 21. *ApJ* 575, 860–870. ► See p. 77
- Tanner, A., Ghez, A. M., Morris, M. R., Christou, J. C., 2005. Stellar Bow Shocks in the Northern Arm of the Galactic Center: More Members and Kinematics of the Massive Star Population. *ApJ* 624, 742–750. ► See p. 77
- Taylor, J. H., Weisberg, J. M., 1989. Further experimental tests of relativistic gravity using the binary pulsar PSR 1913 + 16. *ApJ* 345, 434–450. ► See p. 46
- Thirring, H., Lense, J., 1918. Über den Einfluss der Eigenrotation der Zentralkörper auf die Bewegung der Planeten und Monde nach der Einsteinschen Gravitationstheorie. *Physikalische Zeitschrift* 19, 156–163. ► See p. 49
- Thorne, K. S., Zytow, A. N., 1975. Red giants and supergiants with degenerate neutron cores. *ApJ* 199, L19–L24. ► See p. 14, 58
- Tiede, G. P., Frogel, J. A., Terndrup, D. M., 1995. Implications of New JHK Photometry and a Deep Infrared Luminosity Function for the Galactic Bulge. *AJ* 110, 2788–+. ► See p. 10
- Timmes, F. X., Woosley, S. E., Weaver, T. A., 1996. The Neutron Star and Black Hole Initial Mass Function. *ApJ* 457, 834–+. ► See p. 10
- Torres, D. F., Capozziello, S., Lambiase, G., 2000. Supermassive boson star at the galactic center? *Phys. Rev. D* 62, 104012. ► See p. 41, 42
- Tremaine, S., et al., 2002. The Slope of the Black Hole Mass versus Velocity Dispersion Correlation. *ApJ* 574, 740–753. ► See p. 4
- Tsiklauri, D., Viollier, R. D., 1998. Dark Matter Concentration in the Galactic Center. *ApJ* 500, 591. ► See p. 41, 42
- Ulmer, A., 1999. Flares from the Tidal Disruption of Stars by Massive Black Holes. *ApJ* 514, 180–187. ► See p. 61, 62, 63
- Ulmer, A., Paczynski, B., Goodman, J., 1998. Tidal disruption Eddington envelopes around massive black holes. *A&A* 333, 379–384. ► See p. 61

- Valluri, M., Ferrarese, L., Merritt, D., Joseph, C. L., 2005. The Low End of the Supermassive Black Hole Mass Function: Constraining the Mass of a Nuclear Black Hole in NGC 205 via Stellar Kinematics. *ApJ* In press, 20 July 2005, v628, [arXiv:astro-ph/0502493](#). ► See p. 4
- Vilkoviskij, E. Y., Czerny, B., 2002. The role of the central stellar cluster in active galactic nuclei. I. Semi-analytical model. *A&A* 387, 804–817. ► See p. 75
- Virbhadra, K. S., Ellis, G. F. R., 2000. Schwarzschild black hole lensing. *Phys. Rev. D* 62 (8), 084003–+. ► See p. 55
- Vollmer, B., Duschl, W. J., 2001. The stability of the Circumnuclear Disk clouds in the Galactic Centre. *A&A* 377, 1016–1022. ► See p. 78
- Wang, J., Merritt, D., 2004. Revised Rates of Stellar Disruption in Galactic Nuclei. *ApJ* 600, 149–161. ► See p. 59, 60
- Wardle, M., Yusef-Zadeh, F., 1992. Gravitational lensing by a massive black hole at the Galactic center. *ApJ* 387, L65–L68. ► See p. 50, 55
- Weinberg, N. N., Milosavljević, M., Ghez, A. M., 2005. Stellar Dynamics at the Galactic Center with an Extremely Large Telescope. *ApJ* 622, 878–891. ► See p. 24, 39, 43, 48, 49, 85
- Weinberg, S., 1972. *Gravitation and cosmology: Principles and applications of the general theory of relativity*. New York: Wiley. ► See p. 48
- Wilkinson, M. I., Evans, N. W., 1999. The present and future mass of the Milky Way halo. *MNRAS* 310, 645–662. ► See p. 45
- Wilson, J. R., Mathews, G. J., 2004. White Dwarfs near Black Holes: A New Paradigm for Type I Supernovae. *ApJ* 610, 368–377. ► See p. 67
- Wollman, E. R., Geballe, T. R., Lacy, J. H., Townes, C. H., Rank, D. M., 1976. Spectral and spatial resolution of the 12.8 micron NE II emission from the galactic center. *ApJ* 205, L5–L9. ► See p. 31
- Young, P., 1980. Numerical models of star clusters with a central black hole. I - Adiabatic models. *ApJ* 242, 1232–1237. ► See p. 17
- Yu, Q., Tremaine, S., 2002. Observational constraints on growth of massive black holes. *MNRAS* 335, 965–976. ► See p. 3
- Yu, Q., Tremaine, S., 2003. Ejection of Hypervelocity Stars by the (Binary) Black Hole in the Galactic Center. *ApJ* 599, 1129–1138. ► See p. 45
- Yusef-Zadeh, F., Melia, F., Wardle, M., 2000. The Galactic Center: An Interacting System of Unusual Sources. *Science* 287, 85–91. ► See p. 6
- Yusef-Zadeh, F., Morris, M., 1987. Structural details of the Sagittarius A complex - Evidence for a large-scale poloidal magnetic field in the Galactic center region. *ApJ* 320, 545–561. ► See p. 64
- Zahn, J.-P., 1989. Tidal evolution of close binary stars. I - Revisiting the theory of the equilibrium tide. *A&A* 220, 112–116. ► See p. 28
- Zhao, H., Haehnelt, M. G., Rees, M. J., 2002. Feeding black holes at galactic centres by capture from isothermal cusps. *New Astronomy* 7, 385–394. ► See p. 14, 60
- Zoccali, M., et al., 2003. Age and metallicity distribution of the Galactic bulge from extensive optical and near-IR stellar photometry. *A&A* 399, 931–956. ► See p. 10